# Compressive Sensing for Microwave and Millimeter-Wave Array Imaging

by

Qiao Cheng

A thesis submitted to the University of London in partial fulfilment of the requirements for the degree of

Doctor of Philosophy

School of Electronic Engineering and Computer Science
Queen Mary, University of London
United Kingdom

January 2018

**TO MY FAMILY**

# Abstract

Compressive Sensing (CS) is a recently proposed signal processing technique that has already found many applications in microwave and millimeter-wave imaging. CS theory guarantees that sparse or compressible signals can be recovered from far fewer measurements than those were traditionally thought necessary. This property coincides with the goal of personnel surveillance imaging whose priority is to reduce the scanning time as much as possible. Therefore, this thesis investigates the implementation of CS techniques in personnel surveillance imaging systems with different array configurations.

The first key contribution is the comparative study of CS methods in a switched array imaging system. Specific attention has been paid to situations where the array element spacing does not satisfy the Nyquist criterion due to physical limitations. CS methods are divided into the Fourier transform based CS (FT-CS) method that relies on conventional FT and the direct CS (D-CS) method that directly utilizes classic CS formulations. The performance of the two CS methods is compared with the conventional FT method in terms of resolution, computational complexity, robustness to noise and under-sampling. Particularly, the resolving power of the two CS methods is studied under various circumstances. Both numerical and experimental results demonstrate the superiority of CS methods. The FT-CS and D-CS methods are complementary techniques that can be used together for optimized efficiency and image reconstruction.

The second contribution is a novel 3-D compressive phased array imaging algorithm based on a more general forward model that takes antenna factors into consideration. Imaging results in both range and cross-range dimensions show better performance than the conventional FT method. Furthermore, suggestions on how to design the sensing configurations for better CS reconstruction results are provided based on coherence analysis. This work further considers the near-field imaging with a near-field focusing technique

integrated into the CS framework. Simulation results show better robustness against noise and interfering targets from the background.

The third contribution presents the effects of array configurations on the performance of the D-CS method. Compressive MIMO array imaging is first derived and demonstrated with a cross-shaped MIMO array. The switched array, MIMO array and phased array are then investigated together under the compressive imaging framework. All three methods have similar resolution due to the same effective aperture. As an alternative scheme for the switched array, the MIMO array is able to achieve comparable performance with far fewer antenna elements. While all three array configurations are capable of imaging with sub-Nyquist element spacing, the phased array is more sensitive to this element spacing factor. Nevertheless, the phased array configuration achieves the best robustness against noise at the cost of higher computational complexity.

The final contribution is the design of a novel low-cost beam-steering imaging system using a flat Luneburg lens. The idea is to use a switched array at the focal plane of the Luneburg lens to control the beam-steering. By sequentially exciting each element, the lens forms directive beams to scan the region of interest. The adoption of CS for image reconstruction enables high resolution and also data under-sampling. Numerical simulations based on mechanically scanned data are conducted to verify the proposed imaging system.

# Acknowledgments

Four years Ph.D. life is short compared to one's lifetime, but it is the most important and valuable four years for me. During the past four years, I have met many difficulties and managed to overcome them. I could not have gone this far without support and encouragement from many people. Therefore, I would like to express my sincere gratitude to those who have given their support through the journey of my Ph.D..

Firstly I would like to thank the China Scholarship Council for their financial support during my Ph.D. study. Thanks are also due to the Engineering and Physical Sciences Research Council (EPSRC) in the UK. Part of my work were accomplished by their funding (EP/I034548/1).

I would like to thank my supervisor Prof. Yang Hao for allowing me to conduct this research on microwave and Millimeter-wave imaging under his supervision. He offered me many valuable ideas, suggestions and comments with his profound knowledge and rich research experience. He has always taught me that doing research is different from being an engineer, one should not confine his or her view in one particular area but needs to be open-minded to other disciplines. His scientific intuition, expertise and technical insight had a crucial impact on my research career, and will definitely be with me for years to come.

I would also like to express my gratitude to my joint supervisor Dr. Akram Alomainy. I am very grateful for his supervision, advice, and proofreading of my papers, reports, presentation slides. He was easily available and accessible and willing to discuss whenever I needed his guidance and support. He is also a warm and encouraging friend. Without his constant support, it is impossible for me to finish my research. It was my great pleasure to be his student.

I sincerely thank Dr. Max Munoz Torrico, Dr. Massimo Candotti and Mr. Tony Stone for their fruitful discussion and kind help in setting up the active Millimeter-wave imaging system in the antenna lab, without which many of the investigations in this thesis could not have been performed.

I am deeply grateful to my fellow labmates: Biyi Wu, Darryl Smith, Dr. Jiefu Zhang, Dr. Jiandong Lang, Dr. Ke Yang, Liang Yang, Dr. Lei Li, Majid Naeem, Min Zhou, Nishtha Chopra and Qianyun Zhang, for the research discussions, for the sleepless nights we were working together before deadlines, and for all the fun we have had in the past four years. I would also like to extend my gratitude to many other colleagues from the antenna research group. It was a pleasure to work with them.

Finally, last but by no means least, I would like to thank my parents, who have provided me through moral and emotional support in my life. It was their unconditional love and support that gave me courage and confidence to finish my research work.

# Table of Contents

**Abstract** i

**Acknowledgments** iii

**Table of Contents** v

**List of Figures** ix

**List of Tables** xv

**List of Abbreviations** xvi

**1 Introduction** 1

1.1 Background . . . . . 1

1.2 Motivation and Research Objectives . . . . . 3

1.3 Outline of the Thesis . . . . . 4

References . . . . . 6

**2 Microwave and Millimeter-wave Array Imaging** 9

2.1 Introduction . . . . . 9

2.2 Array Configurations . . . . . 11

2.2.1 Switched Array . . . . . 11

2.2.2 MIMO Array . . . . . 13

2.2.3 Phased Array . . . . . 16

2.3 Conventional Image Reconstruction . . . . . 17
2.3.1 Imaging Algorithm . . . . . 17
2.3.2 Spatial and Frequency Sampling . . . . . 20
2.3.3 Range and Cross-Range Resolution . . . . . 21
2.4 Summary . . . . . 22
References . . . . . 22

**3 Compressive Sensing and its Application to Imaging 26**
3.1 Introduction . . . . . 26
3.2 Sparsity and Compressibility . . . . . 27
3.3 The Basic Framework of Compressive Sensing . . . . . 28
3.4 Properties of Sensing Matrix . . . . . 31
3.4.1 Spark . . . . . 31
3.4.2 Mutual Coherence . . . . . 32
3.4.3 Restricted Isometry Property . . . . . 32
3.5 Recovery Algorithms . . . . . 33
3.5.1 Convex Optimization . . . . . 34
3.5.2 Greedy Algorithms . . . . . 35
3.5.3 Probabilistic Methods . . . . . 36
3.6 Compressive Sensing for Imaging Applications . . . . . 37
3.6.1 Compressive Sensing Implementation in Array Imaging . . . . . 37
3.6.2 Compressive Sensing for Radar Imaging . . . . . 39
3.7 Summary . . . . . 41
References . . . . . 41

**4 Compressive Sensing for Switched Array Imaging 48**
4.1 Introduction . . . . . 48
4.2 Switched Array 2-D Forward Imaging Model . . . . . 49
4.3 Compressive Sensing Implementation to Switched Array . . . . . 50
4.3.1 D-CS Model . . . . . 50

4.3.2 FT-CS Model . . . . . 53
4.3.3 Reconstruction Algorithms . . . . . 54
4.4 Numerical Analysis . . . . . 56
4.4.1 Simulation Configuration . . . . . 56
4.4.2 Sparsity Constraint . . . . . 57
4.4.3 Sampling Pattern And Sampling Interval . . . . . 61
4.4.4 Computational Complexity . . . . . 68
4.4.5 Resolution . . . . . 71
4.5 Experimental Results . . . . . 77
4.6 Summary . . . . . 79
References . . . . . 80

**5 Compressive Sensing for Phased Array Imaging 83**
5.1 Introduction . . . . . 83
5.2 Phased Array Forward Imaging Model . . . . . 84
5.3 Compressive Sensing Implementation to Phased Array . . . . . 88
5.3.1 CS Forward Imaging Model . . . . . 88
5.3.2 Reconstruction Algorithms . . . . . 89
5.3.3 Numerical Investigations and Analysis . . . . . 91
5.4 Compressive Phased Array Imaging with Near-field Focusing . . . . . 101
5.4.1 Comparison of Far-field Focusing and Near-field Focusing . . . . . 103
5.4.2 Compressive Sensing Implementation based on Near-field Focusing Technique . . . . . 107
5.4.3 Numerical Results and Analysis . . . . . 108
5.5 Summary . . . . . 113
References . . . . . 114

**6 Comparative Study of Compressive Sensing Methods in Different Array Configurations 117**
6.1 Introduction . . . . . 117

6.2 Compressive MIMO Array Imaging . . . . . 118
6.2.1 MIMO Array Design . . . . . 118
6.2.2 CS Implementation . . . . . 122
6.3 Numerical Analysis . . . . . 124
6.3.1 Resolution . . . . . 125
6.3.2 Impact of Element Spacing . . . . . 128
6.3.3 Robustness against Noise . . . . . 130
6.3.4 Computational Complexity . . . . . 133
6.4 Summary . . . . . 136
References . . . . . 137

**7 Compressive Luneburg Lens Imaging 138**
7.1 Introduction . . . . . 138
7.2 Luneburg Lens Design . . . . . 139
7.3 Compressive Luneburg Lens Imaging Formulation . . . . . 142
7.4 Numerical Analysis . . . . . 146
7.5 Summary . . . . . 153
References . . . . . 154

**8 Conclusions and Future Work 157**
8.1 Summary . . . . . 157
8.2 Key Contributions . . . . . 159
8.3 Future work . . . . . 160

**Appendix A Author's publications 163**

**Appendix B Code for Antenna Radiation Pattern Generation in CST 165**
B.1 Matlab Code to Control CST . . . . . 165
B.2 VBA Code to Configure CST . . . . . 167
B.3 Matlab Code to Extract Data . . . . . 167

# List of Figures


2.1 Block diagram of a SAR imaging system. . . . . 10

2.2 Array geometry for (a) switched array (b) MIMO array and (c) phased array. . . . . 12

2.3 L-3 ProVision full body scanner in an airport [14]. . . . . 13

2.4 Fully electronic imaging prototype with 736 Tx and 736 Rx antennas operating from 72 to 80 GHz [7]. . . . . 14

2.5 Rohde & Schwarz quick personnel security scanner deployed at the London City Airport [19]. . . . . 15

2.6 SAR imaging configuration. . . . . 17

3.1 Example of a spares signal with only 6 non-zeros. . . . . 27

3.2 Example of a compressible signal. . . . . 28

3.3 Signal recovery using $\ell_p$-norm with (a) $p = 1$ and (b) $p = 2$. . . . . 30

3.4 Single-pixel camera and data under-sampling. . . . . 37

3.5 From imaging model to CS model. . . . . 38

4.1 Switched array imaging system. . . . . 51

4.2 Simulation model in FEKO. All dimensions are in mm. . . . . 57

4.3 The (a) amplitude, (b) phase, (c) real and (d) imaginary parts of the reconstructed signal by the BP method. . . . . 58

4.4 MSE of reconstructed images of different sparsity constraints. (a) FT-CS and (b) D-CS. . . . . 59

4.5 Four random under-sampling masks under (a) $\lambda/4$ element spacing, (b) $\lambda/2$ element spacing and (c) $3\lambda/4$ element spacing. From left to right, sampling rates of four masks are 80%, 60%, 40% and 20%, respectively. . 62
4.6 Simulation results showing the reconstruction quality of three methods based on (a) $\lambda/4$ element spacing, (b) $\lambda/2$ element spacing and (c) $3\lambda/4$ element spacing. In each subfigure, from left to right, D-CS methods with grid size of $\lambda/8$, $\lambda/4$ and $\lambda/3$, FT-CS method and BP method. . . . . 65
4.7 MSE trend of three methods with element spacing of $\lambda/2$ and $\lambda/4$. . . . . 66
4.8 MSE of the target area for the BP, FT-CS and three D-CS methods. . . . 66
4.9 Averaged running time of different methods versus random under-sampling. 69
4.10 Reconstruction results of two point scatterers at $(\pm 0.9, 0)$ by (a) BP with 100% data, (b) BP with 50% data, (c) FT-CS with 100% data and (d) FT-CS with 50% data. . . . . 70
4.11 One-dimensional cut of BP and FT-CS methods for point scatterers at $(\pm 0.9, 0)$. . . . . 71
4.12 Reconstruction results of two point scatterers at $(\pm 0.9, 0)$ by (a) D-CS with 50% data and (b) D-CS with 10% data. . . . . 72
4.13 Reconstruction results of two point scatterers at $(\pm 0.5, 0)$ with (a) $L_{ROI} = 20$, (b) $L_{ROI} = 12$ and (c) $L_{ROI} = 4$. (d) One-dimensional reconstruction at $y = 0$. . . . . 74
4.14 Reconstruction results of two point scatterers at $(\pm 0.5, 0)$ with (a) $L_{ROI} = 20$, (b) $L_{ROI} = 12$ and (c) $L_{ROI} = 4$. (d) One-dimensional reconstruction at $y = 0$. . . . . 75
4.15 System setup: (a) measuring equipments, (b) two identical targets with metallic stripes, (c) NSI scanner and (d) measuring equipments with an attenuator. . . . . 76
4.16 Experimental results showing the reconstruction quality of three methods based on element spacing of (a) $2.25\lambda$, (b) $3\lambda$ and (c) $3.75\lambda$. . . . . 78

4.17 Experimental results showing the effect of transmitting power of three methods with different sampling rates. (a) 100% sampling rate (full sampling). (b) 60% sampling rate. . . . . 79

5.1 Three-dimensional imaging using 2-D phased array and wideband signals. By assigning appropriate weights to each element, the main beam of the array is focused in the direction of $(\theta, \phi)$ while the sidelobes are suppressed in the undesired directions. . . . . 85

5.2 Three-dimensional reconstruction of 6 point scatterers. (a) Ground truth of the target scene. (b) Reconstruction by the proposed method. . . . . 92

5.3 Reconstruction results of point scatterers by (a) FT method with 40% data, (b) FT method with 100% data and (c) CS method with 40% data. (d) Averaged MSE of the CS method as a function of sampling rate. . . . 94

5.4 Two-dimensional reconstruction of double-point scatterers at $(0, 0, 50 \pm 0.175)$ and $(0, \pm 1, 0)$. (a and c) CS method with 10% data. (b and d) FT method with 100% data. . . . . 95

5.5 One-dimensional slice reconstruction of double-point scatterers at (a) $(0, 0, 50 \pm 0.17)$, (b) $(0, 0, 50 \pm 0.65)$, (c) $(0, \pm 0.4, 0)$ and (d) $(0, \pm 2.3, 0)$. . . . . 97

5.6 CS reconstructions of different array configurations using the same number of measurements. (a) Switched array and (b) phased array with 20 dB SNR. (c) Switched array and (d) phased array with -50 dB SNR. . . . . 98

5.7 Averaged MSE comparison of switched array and phased array schemes as a function of SNR. . . . . 99

5.8 The $t_{\%}$-average mutual coherence as a function of (a) array distance, (b) array length (c) number of angles and (d) number of frequency points. . . 100

5.9 Phased array imaging system. Antenna main beam is steered toward various directions to probe the target region. . . . . 103

5.10 Simulated electric field distribution in the near-field region at a distance of 15 cm from a 6 cm × 6 cm aperture in 60 GHz. (a) Far-field focusing. (b) Near-field focusing. . . . . 105
5.11 Comparison of two sampling methods in 2-D cross-range imaging case. Both methods have the same number of measurements. (a) Intersection points of the angle steered beams and the target plane. (b) Sampling points of the proposed near-field method on the target plane. . . . . 106
5.12 Image reconstruction of 64 squares by the (a) far-field focusing and (b) near-field focusing methods. The squares have 0.6 cm length and 0.3 cm spacing. Ground truth targets are also marked in green dotted lines for reference. . . . . 109
5.13 Two-dimensional reconstruction of targets at a distance of 15 cm from the aperture under -50 dB SNR. 5×5 point scatterers reconstruction of (a) far-field method and (b) near-field method. T-shaped target reconstruction of (c) far-field method and (d) near-field method. . . . . 110
5.14 Averaged MSE comparison of the far-field and near-field schemes as a function of SNR. . . . . 111
5.15 Normalized power density along the $z$-axis as a function of the distance from the aperture. . . . . 112
5.16 Composite target visualization. (a)Cross range view. (b) 3-D view. Two-dimensional images are reconstructed using 50% data under 60 dB SNR. (c) Far-field method. (d) Near-field method. . . . . 113

6.1 Cross MIMO array and its equivalent virtual array. . . . . 121
6.2 Cross MIMO array imaging system. . . . . 122
6.3 Image reconstruction of two point scatterers with a spacing of 0.8 cm by the (a) switched array, (b) MIMO array and (c) phased array. . . . . 125
6.4 One-dimensional cut of the 2-D reconstruction at $y = 0$ by the (a) switched array, (b) MIMO array and (c) phased array. . . . . 125

6.5 Three sets of target scenes with different level of sparsity. (a) 4 squares, (b) 16 squares and (c) 36 squares with length of 1 cm and spacing of 0.6 cm. . . . . 126
6.6 Image reconstruction of 4 squares by (a) switched array (b) MIMO array and (c) phased array. Image reconstruction of the 16 squares by (d) switched array (e) MIMO array and (f) phased array. Image reconstruction of 36 squares by (g) switched array (h) MIMO array and (i) phased array. . . . . 127
6.7 Image reconstruction of 36 squares with 1.2 cm spacing by (a) switched array (b) MIMO array and (c) phased array. . . . . 128
6.8 Array topology of the MIMO array with (a) one wavelength spacing in virtual aperture and (b) one and a half wavelength spacing in virtual aperture. . . . . 128
6.9 Image reconstruction of 36 squares by (a) switched array (b) MIMO array and (c) phased array with one wavelength element spacing. Image reconstruction of 36 squares by (d) switched array (e) MIMO array and (f) phased array with one and a half wavelength element spacing. . . . . 129
6.10 Image reconstruction of 9 point scatterers by (a) switched array (b) MIMO array and (c) phased array with one and a half wavelength element spacing. 130
6.11 Two sets of target scenes with different level of sparsity. (a) 4 squares and (b) 49 point scatterers. . . . . 131
6.12 Image reconstruction of 4 squares by (a) switched array (b) MIMO array and (c) phased array. Image reconstruction of 49 point scatterers by (d) switched array (e) MIMO array and (f) phased array. . . . . 132

7.1 Ray tracing for (a) original and (b) transformed Luneburg lens [12]. . . . 139
7.2 Cross-section of the discretized flat Luneburg lens and spherical Luneburg lens after considering 6 shells of dielectric material with the optimised dimensions as in Table I. . . . . 140

7.3 Compressive sensing based Luneburg lens imaging system. . . . . 142
7.4 Luneburg lens imaging system using a mechanically scanned horn antenna. 147
7.5 (a) Dimensions of the pyramid horn antenna and (b) its radiation pattern. 147
7.6 S-parameter of the pyramid horn antenna. . . . . 148
7.7 Three-dimensional far-field directivity patterns at 10 GHz for different positions of the horn, (a) at 0, (b) 10, (c) 20 and (d) 30 mm along the $x$ axis. . . . . 149
7.8 Image reconstruction of four stripe targets using 50% random samples. (a) The ground truth and (b) reconstruction by the proposed imaging method. . . . . 150
7.9 Ground truth of the (a) rectangular stripe target and (b) T-shaped target. 150
7.10 Stripe target reconstruction with (a) 30 × 30, (b) 20 × 20 and (c) 12 × 12 feeding locations. T-shaped target reconstruction with (a) 30 × 30, (b) 20 × 20 and (c) 12 × 12 feeding locations. . . . . 151
7.11 Ground truth of the 9 square target with (a) 2 cm spacing and (b) 1 cm spacing. . . . . 152
7.12 Reconstruction of 2 cm spaced square targets using (a) 30 × 30, (b) 20 × 20 and (c) 12 × 12 feeding locations. Reconstruction of 1 cm spaced square targets using (a) 30 × 30, (b) 20 × 20 and (c) 12 × 12 feeding locations. . . . . 152

# List of Tables

3-A $\ell_1$ minimization problems and solvers . . . . . 35

4-A Complexity Comparison of D-CS Methods . . . . . 68

6-A Complexity Comparison of the Unoptimized Code and the Optimized Code 135

6-B Computing Time of the **H** matrix . . . . . 136

7-A Flat Luneburg Lens Transformed from a Spherical Lunebrug Lens . . . . 142

# List of Abbreviations

| | |
|---|---|
| 1-D | One-Dimensional |
| 2-D | Two-Dimensional |
| 3-D | Three-Dimensional |
| ADC | Analog to Digital Converters |
| ADMM | Alternating Direction Method of Multipliers |
| BA | Born Approximation |
| BPDN | Basis Pursuit Denoising |
| BPIC | Basis Pursuit with Inequality Constraints |
| CoSaMP | Compressive Sampling Matching Pursuits |
| COM | Component Object Model |
| CS | Compressive Sensing |
| DBF | Digital Beam-forming |
| DCT | Discrete Cosine Transform |
| DDC | Digital Down-Converters |
| EM | Electromagnetic |
| F-K | Frequency-wavenumber |
| FT | Fourier Transform |
| GO | Geometrical Optics |

| | |
|---|---|
| GPR | Ground-penetrating Radar |
| IHT | Iterative Shrinkage-threshold |
| IF | Intermediate Frequency |
| IFT | Inverse Fourier Transform |
| i.i.d. | Independent and Identically Distributed |
| ILA | Integrated Lens Antenna |
| LO | Local Oscillator |
| MIMO | Multiple Input Multiple Output |
| MMV | Multiple Measurement Vectors |
| MMW | Millimeter-Wave |
| MRI | Magnetic Resonance Imaging |
| MSE | Mean Squared Errors |
| MSP | Method of the Stationary Phase |
| NDT&E | Nondestructive Testing and Evaluation |
| OMP | Orthogonal Matching Pursuit |
| PO | Physical Optics |
| PSF | Point Spread Function |
| QMUL | Queen Mary University of London |
| RFID | Radio Frequency Identification |
| RIP | Restricted Isometry Property |
| RMA | Range Migrations Algorithm |
| ROI | Region of Interest |
| SAFT | Synthetic Aperture Focusing Technique |
| SALSA | Split Augmented Lagrangian Shrinkage Algorithm |
| SAR | Synthetic Aperture Radar |
| SISO | Single Input Single Output |

| | |
|---|---|
| SNR | Signal-to-noise ratio |
| TE-SAT | Terrorism Situation and Trend Report |
| TO | Transformation Optics |
| TV | Total Variation |
| TwIST | Two Step Iterative Shrinkage Threshold |
| TWI | Through-the-wall Imaging |
| UWB | Ultra-wide-band |
| VBA | Visual Basic for Applications |
| VNA | Vector Network Analyzer |

# Chapter 1

# Introduction

## 1.1 Background

While terrorism is not new to the international community, the number of terror attacks has dramatically increased over the past few years. According to the European Union Terrorism Situation and Trend Report (TE-SAT) 2016 [1], a total of 1077 terror suspects were detained in 2015 across the EU, significantly higher than that of 2014 when 774 were arrested. The UK had the highest number of failed, foiled or completed terror attacks in 2015, racking up 103 attempted incidents, followed by France with 72 and Spain with 25.

In response to the increasing threat of terrorism, personnel surveillance at public places, such as airports, train stations, government buildings and shopping malls, is becoming increasingly important. The priority is to have an efficient security system that can detect concealed weapons and hidden explosives. Conventional X-ray imaging systems have been very successful for luggage checking and are potentially effective for personnel imaging. However, X-ray is ionizing radiation, and thus can pose health hazard to human body. Electromagnetic signals at microwave and millimeter wave frequencies are capable of inspecting dielectric materials and composite structures, thus are well

suited for penetrating clothing materials to image items concealed by common clothing. Also, the radiation power of the electromagnetic imaging system could be 1000 times lower than the EU standard (the UK policy is to comply with the EU standard) for the maximum allowed radiation power density on an individual, which is 50 $W/m^2$ [2], relieving the concerns about adverse effect on the human body. These characteristics make the microwave and Millimeter-wave (MMW) imaging techniques a good candidate for personnel surveillance applications.

Existing microwave and MMW imaging systems fall into two categories: active approach and passive approach. A typical passive imaging approach employs a focusing lens and a receiving array near the focal region. Its operating principle is analogous to an optical camera, in which the image is formed point by point, with each pixel directly representing the naturally-emitted radiation from a point in the target scene. The main advantage of the passive approach is that the system does not emit radio waves and thus poses no radiation hazard to individuals. However, this feature also hinders its use in the indoor environment, i.e. the natural illumination would be very weak and the emissivity contrast between the target and its background could be very difficult to differentiate. The fundamental difference between the passive approach and the active approach lies in the fact that there is artificial illumination in the active approach, and because of this, active imaging has more flexibilities in designing imaging algorithms with a variety of transmitting waveforms to choose. The active approach usually includes a transmitter for electromagnetic wave generation and a receiver for receiving backscattered data from the target. The mechanism of active imaging relies on the reflectivity contrast from different materials in the target scene. In comparison, the active approach usually exhibits much higher dynamic range than the passive approach.

## 1.2 Motivation and Research Objectives

A coherent active imaging system operates by sampling the amplitude and phase of backscattered field from a given scene. The sampled data is then used for image reconstruction with Fourier Transform (FT) based algorithms [3]. However, due to the well-known Nyquist sampling theorem, generating high-resolution images using FT techniques requires data acquisition over a uniformly and densely sampled set of points, which will introduce prohibitively long detection time for single transceiver systems. For example, it took us approximately 2 hours to scan an area of 400 $mm \times 400$ $mm$ with 2 $mm$ step using an NSI 2000 x-y-z mechanical scanner. This issue can be alleviated by adopting more complicated antenna array systems which enable fast electronic scanning. However, it is still challenging to achieve high frame-rate like real-time video cameras, especially when ultra-wide-band (UWB) signals are used to form three-dimensional (3-D) images. To overcome this issue, one would consider more sparsely sampled data collection strategies where the transceiver only samples a small fraction of required positions. For instance, undersampling with certain trajectory is often adopted in magnetic resonance imaging (MRI) to save scan duration [4]. However, when inverse Fourier transform (IFT) is applied to sparsely sampled data with zero-filling, reconstruction quality can be poor, e.g. aliasing artifacts, low spatial resolution, reduced signal-to-noise ratio (SNR).

The emerging field of Compressive Sensing (CS) [5, 6] has offered great insights into how to solve this issue. CS theory guarantees signal reconstruction from highly under-sampled data provided that the signal is sparse or compressible and proper sensing matrix is adopted. As the 3-D scene to be reconstructed is a map of the spatial distribution of the reflectivity function of stationary targets, the reconstruction can be sparse or compressible in some representations. By utilizing this sparse nature, we can speed up the data acquisition process by under-samping in the spatial and frequency domains while satisfactory reconstruction can still be achieved with CS recovery algorithms. During the last decade, CS techniques have been successfully applied to many imaging applications including (but not limited to) MMW holography [7–9], synthetic aperture radar (SAR)

imaging [10–13] and inverse scattering [14, 15]. Efficient sampling, increased resolution and robustness to noise can be achieved.

The main research question of this thesis is how to utilize CS techniques in personnel surveillance imaging systems. A practical imaging system for personnel surveillance will undoubtedly adopt an antenna array over a single antenna in order to remarkably reduce scanning time. There are already many array based imaging systems in the open literature and in some cases commercially deployed, such as the switched array [16], multiple-input multiple-output (MIMO) array [17, 18] and phased array [19, 20]. The primary focus lies on the implementation of CS imaging algorithms for these array systems. In order to obtain comprehensive understanding of CS imaging algorithms, a comparative study between CS methods and conventional FT methods will be carried out based on different imaging systems. It is well known that the resolution of conventional Fourier imaging system is subject to fundamental limitations [21]. Whether or not CS methods can break this limitation in aforementioned imaging systems is the first priority to study. Many other fundamental aspects considered in traditional methods will also be investigated, such as the robustness to noise and interference, data acquisition time and computational complexity, etc. Both qualitative and quantitative comparisons are considered in the simulation. Experiments are also conducted in the antenna lab to verify numerical results.

## 1.3 Outline of the Thesis

This thesis is organized as follows.

**Chapter 2** - *Microwave and millimeter-wave array imaging.* This chapter first introduces fundamentals of a typical SAR imaging system and then presents the state of the art of imaging systems for personnel surveillance in terms of different array configurations. Conventional three-dimensional image reconstruction algorithm based on the switched array is illustrated in detail, together with achievable resolution in x-y-z

dimensions and the corresponding required sampling intervals in spatial and frequency domains.

**Chapter 3** *Compressive sensing background and its application to imaging.* This chapter presents the mathematical foundation of the CS theory. Two mainstream CS recovery algorithms that based on convex optimization and greedy pursuit are briefly explained, with a summary of the state of the art optimization solvers. Then, the basic framework of CS imaging is explained. Finally, a brief literature review of the CS implementation to radar imaging applications is provided.

**Chapter 4** *Compressive switched array imaging.* This chapter investigates CS implementations in a two-dimensional (2-D) switched array imaging system. Specific attention is paid to situations where the array element spacing does not satisfy the Nyquist criterion due to physical limitations. CS methods are divided into the FT-CS method that relies on conventional FT and the D-CS method that directly utilizes classic CS formulations. The performance of two CS methods is compared with the conventional backpropagation method in terms of resolution, computational complexity, robustness to noise and under-sampling. Particularly, the resolving power of two CS methods is studied under various circumstances. Both numerical and experimental data are applied to yield more conclusive results.

**Chapter 5** *Compressive phased array imaging.* This chapter aims to study the CS implementation in a 2-D phased array imaging system. A general forward model is derived for array based imaging systems by taking into consideration of particular antenna parameters. This model can be easily applied to other array configurations with slight modifications. Thereafter, we introduce a 3-D compressive imaging method based on conventional phased array configurations. Imaging performance comparison is conducted in range and cross-range dimensions in a similar fashion to Chapter 4. Furthermore, suggestions on how to design sensing configurations for better CS reconstruction results are provided based on a coherence analysis. This work is further extended for near-field applications by integrating a near-field focusing technique into the CS frame-

work. A new scanning method has also been provided to focus array beams at different spots with various depths such that they can fully cover the whole target region.

**Chapter 6** *Comparative study of compressive sensing methods in different array configurations.* This chapter gives a comparative study on the performance of CS methods with different array configurations. The aim is to find the best array configuration that fits the compressive sensing framework. A switched array with fixed beams, a MIMO array with fewer antenna elements and a phased array with sharpened and steerable beams are considered for various CS implementations.

**Chapter 7** *Compressive Luneburg lens imaging.* This chapter presents a novel beam-steering imaging system using CS techniques. The proposed system consists of a flat Luneburg lens fed by an antenna array. By exciting antenna elements at different feeding locations, the lens antenna forms directive beams to scan the region of interest. The CS technique is integrated into the imaging algorithm for image reconstruction. Full-wave simulated radiation patterns are used for the calculation of the system response matrix. A fully automated approach for the generation of radiation patterns is given with Matlab and Visual Basic for Applications (VBA) codes. Numerical simulations are provided to demonstrate the effectiveness of the proposed imaging system.

**Chapter 8** *Conclusions and future work.* This chapter concludes the main results of the thesis and provides recommendations for future research.

## References

[1] EUROPOL, "European union terrorism situation and trend report (te-sat) 2016," European Union's law enforcement agency, Tech. Rep., 2016.

[2] I. C. on Non-Ionizing Radiation Protection, "Guidelines for limiting exposure to time-varying electric, magnetic, and electromagnetic fields (up to 300 ghz)," https://www.ncbi.nlm.nih.gov/pubmed/9525427, Apr 1998.

[3] A. Boyer, P. Hirsch, J. Jordan Jr, L. Lesem, and D. Van Rooy, "Reconstruction of ultrasonic images by backward propagation," in *Acoustical Holography.* Springer, 1971, pp. 333–348.

[4] C.-M. Tsai and D. G. Nishimura, "Reduced aliasing artifacts using variable-density k-space sampling trajectories," *Magnetic Resonance in Medicine*, vol. 43, no. 3, pp. 452–458, 2000.

[5] D. Donoho, "Compressed sensing," *IEEE Transactions on Information Theory*, vol. 52, no. 4, pp. 1289–1306, April 2006.

[6] E. Candes, J. Romberg, and T. Tao, "Robust uncertainty principles: exact signal reconstruction from highly incomplete frequency information," *IEEE Transactions on Information Theory*, vol. 52, no. 2, pp. 489–509, Feb 2006.

[7] C. F. Cull, D. A. Wikner, J. N. Mait, M. Mattheiss, and D. J. Brady, "Millimeter-wave compressive holography," *Appl. Opt.*, vol. 49, no. 19, pp. E67–E82, Jul 2010.

[8] L. Qiao, Y. Wang, Z. Shen, Z. Zhao, and Z. Chen, "Compressive sensing for direct millimeter-wave holographic imaging," *Appl. Opt.*, vol. 54, no. 11, pp. 3280–3289, Apr 2015.

[9] Q. Cheng, A. Alomainy, and Y. Hao, "On the performance of compressed sensing-based methods for millimeter-wave holographic imaging," *Appl. Opt.*, vol. 55, no. 4, pp. 728–738, Feb 2016.

[10] V. Patel, G. Easley, J. Healy, D.M., and R. Chellappa, "Compressed synthetic aperture radar," *IEEE Journal of Selected Topics in Signal Processing*, vol. 4, no. 2, pp. 244–254, April 2010.

[11] J. Yang, J. Thompson, X. Huang, T. Jin, and Z. Zhou, "Random-frequency sar imaging based on compressed sensing," *IEEE Transactions on Geoscience and Remote Sensing*, vol. 51, no. 2, pp. 983–994, 2013.

[12] W. Qiu, J. Zhou, H. Zhao, and Q. Fu, "Three-dimensional sparse turntable microwave imaging based on compressive sensing," *IEEE Geoscience and Remote Sensing Letters*, vol. 12, no. 4, pp. 826–830, April 2015.

[13] H. Kajbaf, J. T. Case, Z. Yang, and Y. R. Zheng, "Compressed sensing for

sar-based wideband three-dimensional microwave imaging system using non-uniform fast fourier transform," *IET Radar, Sonar & Navigation*, vol. 7, no. 6, pp. 658–670, 2013.

[14] L. Carin, D. Liu, W. Lin, and B. Guo, "Compressive sensing for multi-static scattering analysis," *Journal of Computational Physics*, vol. 228, no. 9, pp. 3464–3477, 2009.

[15] A. Massa, P. Rocca, and G. Oliveri, "Compressive sensing in electromagnetics - a review," *IEEE Antennas and Propagation Magazine*, vol. 57, no. 1, pp. 224–238, Feb 2015.

[16] D. Sheen, D. McMakin, and T. Hall, "Three-dimensional millimeter-wave imaging for concealed weapon detection," *IEEE Transactions on Microwave Theory and Techniques*, vol. 49, no. 9, pp. 1581–1592, Sep 2001.

[17] X. Zhuge and A. G. Yarovoy, "Three-dimensional near-field MIMO array imaging using range migration techniques," *IEEE Transactions on Image Processing*, vol. 21, no. 6, pp. 3026–3033, June 2012.

[18] S. Ahmed, A. Schiessl, and L. Schmidt, "A novel fully electronic active real-time imager based on a planar multistatic sparse array," *IEEE Transactions on Microwave Theory and Techniques*, vol. 59, no. 12, pp. 3567–3576, Dec 2011.

[19] F. Gumbmann and L. P. Schmidt, "Millimeter-wave imaging with optimized sparse periodic array for short-range applications," *IEEE Transactions on Geoscience and Remote Sensing*, vol. 49, no. 10, pp. 3629–3638, Oct 2011.

[20] S. Patole and M. Torlak, "Two dimensional array imaging with beam steered data," *IEEE Transactions on Image Processing*, vol. 22, no. 12, pp. 5181–5189, Dec 2013.

[21] C. Fischer, W. Wiesbeck, and J. Fortuny, "Fundamental limitations for the resolution of sar sensors," in *EUSAR 2000*, 2000, pp. 467–470.

# Chapter 2

# Microwave and Millimeter-wave Array Imaging

## 2.1 Introduction

Microwave and Millimeter-Wave (MMW) imaging have been widely used in many applications such as SAR, nondestructive testing and evaluation (NDT&E), concealed weapon detection, ground-penetrating radar (GPR) and through-the-wall imaging (TWI) [1–5]. The first formation of SAR images can be traced back to the early 1960s at the Willow Run Laboratories [6]. Ever since then, SAR imaging has become a field of intensive research. Many subsequent applications like security imaging are more or less developed from the SAR imaging. An SAR system is usually implemented by mounting a transmitter-and-receiver pair on a moving platform such as airplane or satellite, from which a target scene is repeatedly illuminated with radio waves. The backscattered waves received successively at different antenna positions are coherently detected, stored and then post-processed together to reconstruct the target scene.

Figure 2.1 shows the block diagram of a typical SAR imaging system. The input signal is mixed with the local oscillator (LO) signal to produce the required working

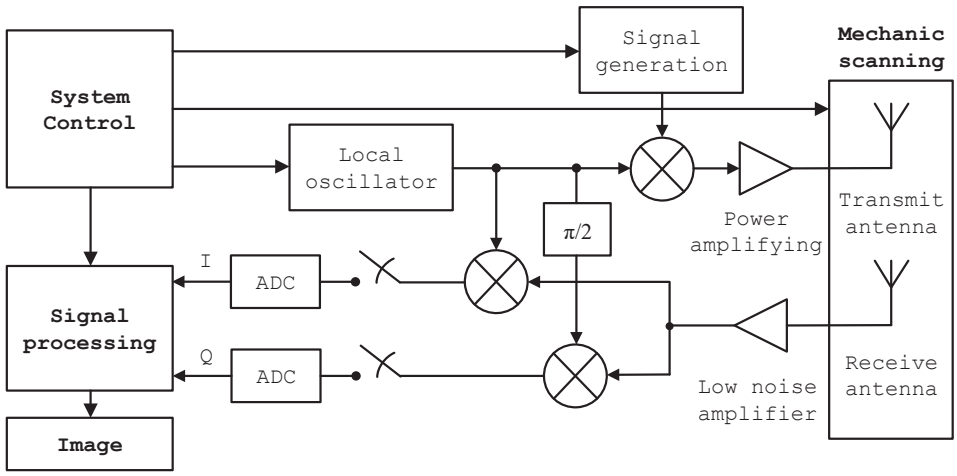


Figure 2.1: Block diagram of a SAR imaging system.

frequency for imaging. The signal is then amplified and transmitted by the transmit antenna. The backscattered signal that contains the target information is received and amplified by the low noise amplifier. This signal is then split into two parts and mixed with LO signal again, but with one of them shifted by $\pi/2$, to convert to baseband frequency. The two baseband signals are then digitized into the real and imaginary parts (also known as in-phase and quadrature components) of the complex radar signal using Analog to Digital Converters (ADCs). The controlling system repeat this process by translating the transmitter/receiver pair to scan the region of interest (ROI). After the data acquisition, the signal processing unit can then reconstruct images with certain algorithms.

In the area of security imaging, MMW frequency region from 30 to 300 GHz has received considerable attention owing to its capability of penetrating dielectric materials such as plastic and cloth while being strongly reflected by metallic materials. Relatively small wavelengths and wide bandwidths associated with these signals enable high resolution in both the range and cross-range dimensions. However, due to its relative short wavelength, MMW circuits and array antennas are costly to implement in the early years. Most imaging systems adopted a linear array configuration with mechanic scanning as a tradeoff between system cost and scanning speed. For example, the authors in [2]

designed a horizontal linear array with vertical mechanic scanning for concealed weapon detection.

Thanks to the enormous advances made in semiconductor technology over the last few years, highly integrated circuits with moderate costs are achievable at MMW frequencies [7, 8]. Antenna array systems are thus becoming affordable in many imaging applications for high resolution and fast electronic scanning. An increased number of antennas requires additional control components such as high speed switches, phase shifters and power dividers, depending on different array configurations. To date, there are already many array configurations which have been proposed in the open literature and in some cases commercially deployed. As will be introduced in the following section, they can be categorized into three groups: the switched array [2, 9], the MIMO array [7, 10, 11] and the phased array [12, 13].

This chapter is organized as follows. Section 2.2 summarizes the details of three different array configurations for security imaging applications. Then, based on the switched array configuration, FT based imaging algorithm, sampling criteria and the corresponding resolution are presented in Section 2.3. Section 2.4 concludes the chapter.

## 2.2 Array Configurations

### 2.2.1 Switched Array

The switched array is the most direct array approach that simply consists of an array of transceiver antennas. During data acquisition, all elements are sequentially switched on and off to transmit and receive radio waves. Figure 2.2(a) illustrates the array geometry of a switched array scheme. The array elements are connected to a high speed switching matrix that is controlled by a central unit. In an ideal situation, all antenna elements share the same radiation pattern and the element spacing can follow the Nyquist sampling theorem to ensure correct image reconstruction. The aperture size of the switched array

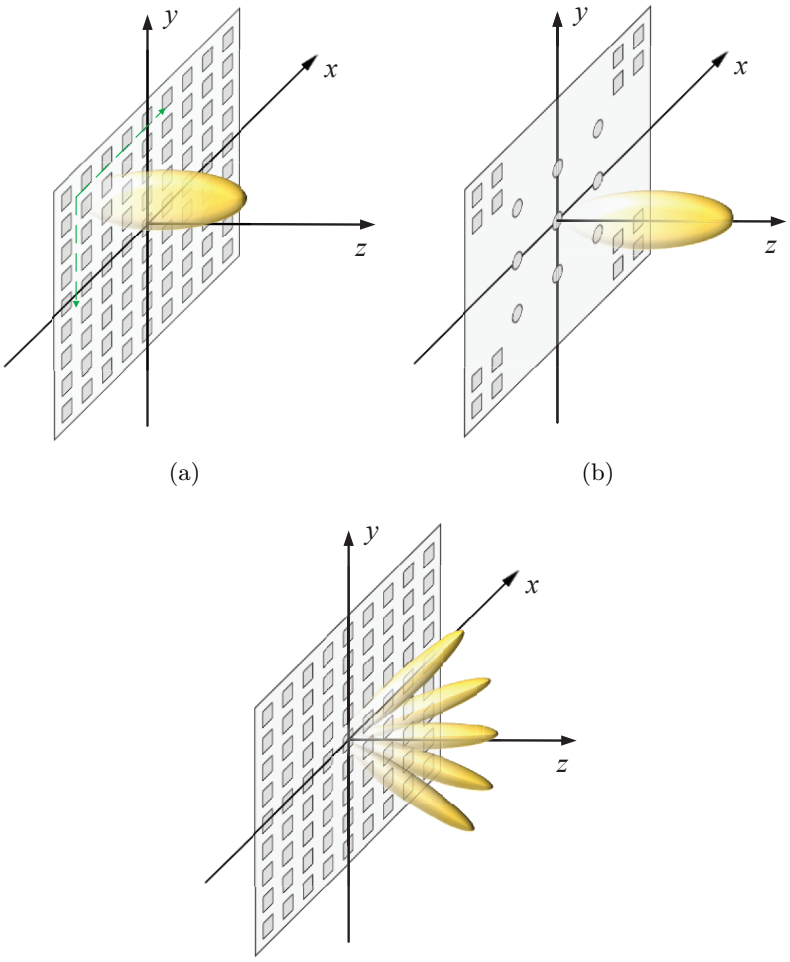


Figure 2.2: Array geometry for (a) switched array (b) MIMO array and (c) phased array.

should be roughly equal to the area being scanned.

In a practical design, there are many circumstances need to be considered and many aspects might be compromised. For example, the design of monostatic transceivers is usually replaced by a quasi-monostatic configuration which transmit and receive antennas are separated, but in approximately the same location and they are assumed to be coincident at the midpoint between the two antennas. The main advantage of separate transmit and receive antennas is that the isolation in excess of 50 dB are easily achievable. Another example is the array aperture size design. The required area for a full body scan

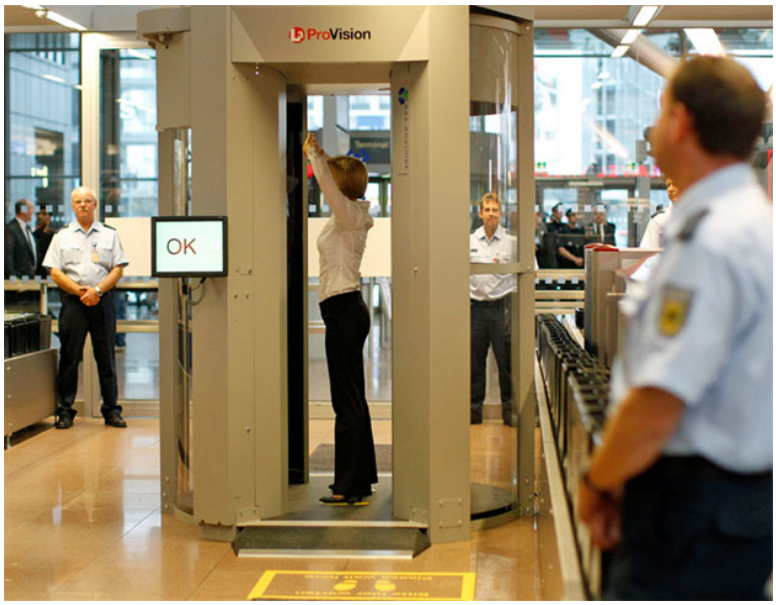


Figure 2.3: L-3 ProVision full body scanner in an airport [14].

in an airport security check can be as large as 2 m × 1 m. To make a full switched array at such size is still too expensive at the moment. Therefore, most commercially realized products combined linear switched array with SAR concept. The most widely deployed full body scanner L-3 ProVision is a good example that utilizes cylindrical scanning [14]. This security body scanner operates at frequencies between 24 and 30 GHz, requiring only a single stationary position during a 1.5-second scan. Figure 2.3 shows the photo of an L-3 ProVision doing full body scanning. The L-3 ProVision products have been deployed in more than 250 airports across the world for counterterrorist detection.

### 2.2.2 MIMO Array

The main disadvantage of the switched array approach is its low efficiency. As each time after a signal is transmitted, only one antenna is switched on for signal reception. The switched array works as a single-input single-output (SISO) system. This is a waste of other antennas who can also be used for reception. To improve the efficiency, the idea of using the MIMO array for security imaging has attracted significant attention in recent years [10, 15]. A MIMO array normally adopts sperate transmit and receive

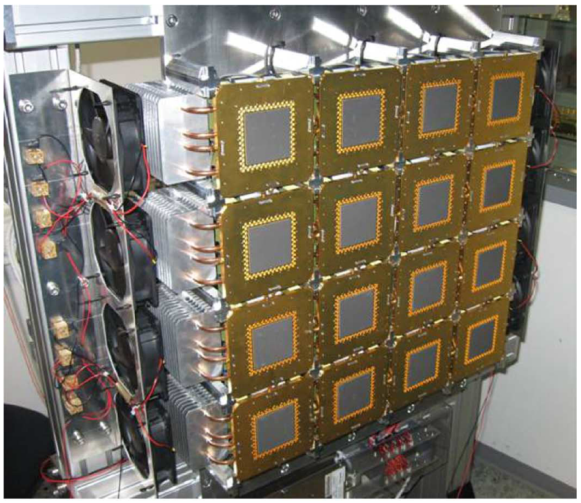

Figure 2.4: Fully electronic imaging prototype with 736 Tx and 736 Rx antennas operating from 72 to 80 GHz [7].

subarrays to form a virtue aperture similar to a switched array. The big advantage of the MIMO configuration is the increased spatial diversity enables a sparse array design while preserving similar imaging performance as a switched array. In some cases, the switched array and the MIMO array are also called monostatic array and multistatic array systems, respectively.

There are already many MIMO array designs for security applications in existing literature [10, 16, 17]. Conventional uniformly distributed MIMO arrays like rectangular arrays and Mills Cross arrays suffer from element shadowing effect along certain directions. According to [18], array configurations that follow curvilinear geometries have less shadowing effect and also decreased grating/sidelobe level in the near-field. Figure 2.2(b) gives an example of a MIMO array geometry, where circles represent transmitting antennas and squares stand for receiving antennas. When each time a signal is transmitted from the transmitter array, all the receive antennas will be switched on for reception in parallel. By properly arranging the element placements, the effective aperture of a MIMO array can be comparable to that of a switched array with far fewer elements. This capability makes it possible to design a fully electronic MIMO array for real-time imaging at an affordable cost.

Figure 2.5: Rohde & Schwarz quick personnel security scanner deployed at the London City Airport [19].

In [7], a new MMW multistatic array architecture was presented for concealed weapon detection with real-time operation capability. This imager was designed and verified from 72 to 80 GHz and demonstrated a lateral resolution of 2 mm. To achieve an array aperture of around 50 cm $\times$ 50 cm, 25600 antennas are required using the switched array configuration. The prototype in [7] managed to achieve the same aperture, at the same base antenna spacing and array aperture size, using a total number of 736 Tx antennas and 736 Rx antennas, which is only 5.75% of its switched array counterpart. Figure 2.4 shows the prototype of the imager that consists of 16 clusters of transmit and receive subarrays. This prototype was later extended to a 2 m $\times$ 2 m aperture using 32 clusters for personnel screening applications [8]. Recently, this millimetre-wave full-body scanner is commercialized by Rohde & Schwarz and has been successfully deployed at London City Airport to increase the speed of security screening and detection. Figure 2.5 shows the Rohde & Schwarz QPS200 personnel screening system deployed at the London City Airport [19] where the two imagers from left to right are responsible for the back and front of a personnel under detection, respectively.

### 2.2.3 Phased Array

From the transmit antenna point of view, the switched array and the MIMO array are similar as antennas operate in a separate/sequential way. Each antenna in transmitting mode is independent and interference free from other transmit antennas. Therefore, the scanning process is actually a fixed (stationary) beam translating within the aperture. On the other hand, a phased array is totally different in the essence that the antennas are controlled by variable phase (very short time-delay) and variable amplitude to provide constructive/destructive interference in different directions. Specifically, the array pattern is sharpened by constructive interference in the main direction while suppressed by destructive interference in undesired directions. Compared to the switched and MIMO arrays, the main advantage of the phased array is its dynamic beam scanning capability. The resulting high gain beam greatly maximizes the SNR [20] and makes the imaging system more robust to noise.

The phased array scheme can be further discussed in two scenarios: an analog phased array that can do beamforming in both transmitting and receiving array; a digital beamforming (DBF) array that normally only do beamforming in the receiving array. DBF receiver consists of the spatial filtering of a signal where the phase shifting and amplitude scaling are implemented digitally. ADCs and Digital Down-Converters (DDCs) are required for each antenna to make the necessary transformations of the signal between the Intermediate Frequency (IF) analog domain and the digital domain. In comparison, a DBF receiver array has lower gain due to beamforming only in receiving mode, but is easier to implement and can dramatically reduce the system cost. In fact, the MMW MIMO array imaging system proposed in [7, 8] also adopted DBF techniques for image reconstruction. However, without loss of generality and to avoid confusion, we consider the phased array as a SISO system where the acquired data is the summation of signals from all antenna elements, which is also to say the imaging algorithms do not have access to the signals of individual antennas.

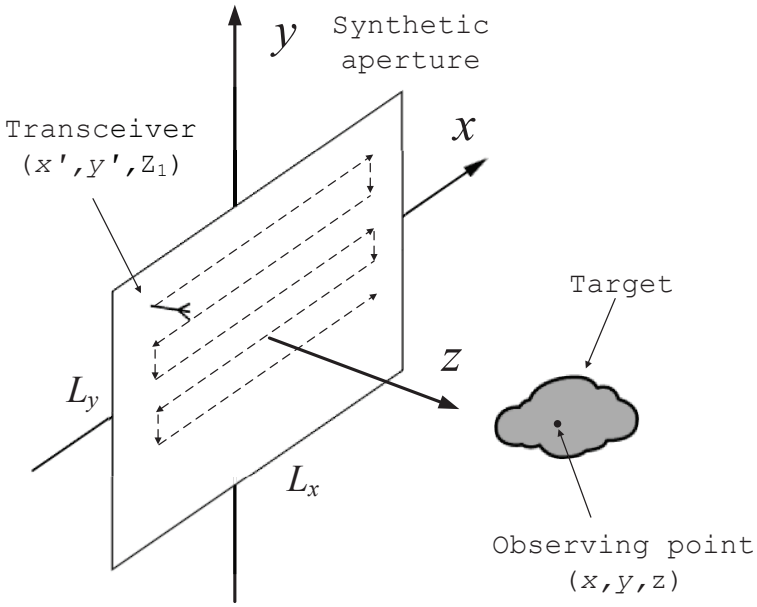


Figure 2.6: SAR imaging configuration.

Figure 2.2(c) gives an example of a typical analog phased array. Although the array geometry is the same as a switched array, there are more complex controlling components like phase shifters and power dividers behind the array aperture. By carefully adjusting the phase shift of each radiating antenna, the main beam of the array can be electronically steered towards different directions. However, this cannot be extended unlimitedly. The scanning angle of a phased array is normally within 120°, e.g., 60° up and 60° down in the $y$ dimension.

## 2.3 Conventional Image Reconstruction

### 2.3.1 Imaging Algorithm

The fundamentals of an array imaging system are not much different from a typical SAR imaging system. Therefore, we start with the 3D-SAR imaging configuration to introduce the basic imaging algorithms. The example SAR imaging system is shown in Figure 2.6. During the imaging process, a transceiver is scanned over a 2-D planar

aperture with size $L_x$ and $L_y$. It is assumed that the transceiver is at position $(x', y', Z_1)$ and a general point $(x, y, z)$ is at the target plane. The target region is characterized by its reflectivity function $g(x, y, z)$. Under Born approximation (BA), the scattering field at the transceiver can be approximately represented by a linear superposition of reflected waves from each point in the target region or

$$s(x', y', k) = \iiint_V g(x, y, z) \exp(-j2k\sqrt{(x - x')^2 + (y - y')^2 + (z - Z_1)^2})\, dx\, dy\, dz, \tag{2.1}$$

where $k = 2\pi f/c$ is the wavenumber, $f$ is the frequency and $c$ is the speed of light. The BA is a necessary assumption to simplify the original complicated inverse scattering problem into (2.1). However, if the BA is not well satisfied, for example, strong multiple scattering exists, the reconstruction based on (2.1) will no longer be accurate. Note that the amplitude attenuation with range is not considered since it will have little impact on image reconstruction. According the dispersion relation, the wavenumber $k$ here can also be expressed as $k_x^2 + k_y^2 + k_z^2 = (2k)^2$, where $k_x$, $k_y$ and $k_z$ are wavenumbers in $x$, $y$ and $z$ dimension, respectively. The exponential term in (2.1) represents a spherical wave, which can be decomposed into an infinite superposition of plane waves [2]

$$\exp(-j2k\sqrt{(x - x')^2 + (y - y')^2 + (z - Z_1)^2}) = \iint \exp(-jk_{x'}(x - x') - jk_{y'}(y - y') - jk_z(z - Z1))\, dk_{x'}\, dk_{y'}, \tag{2.2}$$

where $k_{x'}$ and $k_{y'}$ are the Fourier-transform variables corresponding to $x'$ and $y'$, respectively. The spatial wavenumbers will range from $-2k$ to $2k$ for propagating waves.

Substituting (2.2) into (2.1) and rearranging yields

$$\begin{aligned} s(x', y', k) &= \iint \left[ \iiint g(x, y, z) \exp(-j(k_{x'}x + k_{y'}y + k_z z))\, dx\, dy\, dz \right] \\ &\quad \times \exp(jk_z Z_1) \exp(jk_{x'}x') \exp(jk_{y'}y')\, dk_{x'}\, dk_{y'} \\ &= \iint G(k_{x'}, k_{y'}, k_z) \exp(jk_z Z_1) \exp(j(k_{x'}x' + k_{y'}y'))\, dk_{x'}\, dk_{y'} \\ &= \mathrm{FT}_{2D}^{-1}\{G(k_{x'}, k_{y'}, k_z) \exp(jk_z Z_1)\}. \end{aligned} \tag{2.3}$$

where $\mathrm{FT}_{2D}\{\cdot\}$ and $\mathrm{FT}_{2D}^{-1}\{\cdot\}$ represent 2-D FT operator and its inverse, respectively. The triple integral in the first line of (2.3) represents a 3-D Fourier transform of the reflectivity function and are expressed as $G(k_{x'}, k_{y'}, k_z)$ in the third line. Taking the 2-D Fourier transform of both sides and dropping the distinction between the primed and unprimed coordinate systems yields

$$\mathrm{FT}_{2D}\{s(x, y, k)\} = S(k_x, k_y, k) = G(k_x, k_y, k_z) \exp(jk_z Z_1). \tag{2.4}$$

Moving the exponential term in (2.4) to the left and taking the 3-D inverse Fourier transform of both sides we have the reflectivity function as

$$g(x, y, z) = \mathrm{FT}_{3D}^{-1} \left\{ \mathrm{FT}_{2D}\{s(x, y, k)\} \exp(-j\sqrt{4k^2 - k_x^2 - k_y^2} Z_1) \right\}. \tag{2.5}$$

The final image of the target can be acquired by computing the amplitude of the complex-valued reflectivity function $g(x, y, z)$. In order to perform the inverse 3-D FFT in (2.5), the data need to be uniformly sampled in $k_x$, $k_y$ and $k_z$. This can be easily satisfied in the $k_x$ and $k_y$ domains by uniformly sampling in the $x$, $y$ dimensions. However, due to the dispersion relation, the data in the $k_z$ domain becomes non-uniformly spaced when its uniformly sampled in the frequency dimension. Therefore, before we can take inverse 3-D FFT, we need to use interpolation techniques to resample the data to have uniform intervals in $k_z$. The most well known interpolation technique is the Stolt interpolation that originates from computer based processing of seismic data [21].

The Stolt interpolation compensates the curvature of the wavefront by mapping the data from $\omega$ domain to $k_z$ domain for each frequency component of the measured data. Consequently, this technique is also known as the frequency-wavenumber (F-K) migration algorithm or the range-migrations algorithm (RMA). The original RMA [21] is a 2-D algorithm that was first designed for seismic engineering and then extended to 2-D SAR for space-borne applications [22]. Its 3-D modification was proposed in 2000 by Juan M. Lopez-Sanchez based on the method of the stationary phase (MSP) [23]. The 3-D RMA shows some similarities with the synthetic aperture focusing technique (SAFT) [24, 25]. The SAFT is also a 3-D SAR imaging algorithm which was originally developed from acoustic holography based on angular spectrum decomposition [26]. Its 2-D version (single frequency imaging in the cross-range domain) of is also known as the Backward propagation (BP) algorithm [27]. According to [23], both RMA and SAFT techniques are supposed to have the same order of computational complexity since they both make an extensive use of FFTs. From the electromagnetism point of view, these algorithms are actually a simplification of the complicated inverse scattering problem derived from the Maxwell's equations. Interested readers are referred to [28] for a detailed discussion of these algorithms in the inverse scattering point of view.

### 2.3.2 Spatial and Frequency Sampling

Data acquisition for image reconstruction without aliasing requires the sampling interval to satisfy the Nyquist criterion. Specifically, the Nyquist criterion states that the phase shift from one sample point to the next is less than $\pi$ rad. As illustrated above, the data for 3-D imaging is acquired from $x$, $y$ and frequency dimensions. This Nyqusit sampling in the aperture and the frequency domains need to be discussed separately.

The sampling interval along the aperture is determined by a number of factors including the wavelength, size of the aperture, size of the target, and distance to the target. The most restrictive case is that the target is very close to the aperture and the sample point is near the edge of the aperture. In such case, the maximum phase shift will be

$2k\Delta x$ when the sampling interval is $\Delta x$. Therefore, the required sampling interval in the $x$ and $y$ domains should be

$$\Delta x, \Delta y < \frac{\lambda}{4}, \tag{2.6}$$

where $\lambda = 2\pi/k$. However, for a practical imaging system that usually has a moderate aperture-to-target distance, $\lambda/2$ sampling interval is sufficient [2].

The sampling interval in the frequency domain can be determined in a similar way. The maximum phase shift from a change in wavenumber $\Delta k$ will be $2\Delta k D_{max}$, where $D_{max}$ is the maximum target range. Therefore, by substituting the $\Delta k$ with $2\pi\Delta f/c$, the required sampling interval in the frequency domain should be

$$\Delta f < \frac{c}{4D_{max}}. \tag{2.7}$$

### 2.3.3 Range and Cross-Range Resolution

The above imaging algorithm based on Fourier transform is a diffraction-limited technique which is imposed by the wavelength, transmit and receive antenna beamwidths, size of aperture, and distance to the target. More specifically, the resolution is determined by the extent or width of the coverage in the wavenumber domain. As similar to many other radar imaging systems, the range resolution in the $z$ dimension is dependant on the frequency bandwidth

$$\delta_z = \frac{2\pi}{2(k_2 - k_1)} = \frac{c}{2B}, \tag{2.8}$$

where $k_2$ and $k_1$ are the wavenumbers at highest and lowest frequencies, respectively. The cross-range resolution is usually approximated by [13]

$$\delta_{x,y} = \frac{2\pi}{\text{Range}(k_{x,y})} \approx \frac{\lambda D}{2L_{x,y}}, \tag{2.9}$$

where $D$ is the target range.

## 2.4 Summary

This chapter first presents the background of microwave and millimeter-wave imaging by describing the SAR imaging system. Its application in the security imaging is then discussed and summarized in terms of the switched array, the MIMO array and the phased array. A three-dimensional image reconstruction algorithm based on FT is explained in detail using the switched array example. Resolution of this imaging algorithm is diffraction-limited which depends on wavelength, bandwidth, distance and aperture size. The required sampling step in spatial and frequency dimensions which is determined by the Nyquist theorem is also presented.

## References

[1] S. Kharkovsky and R. Zoughi, "Microwave and millimeter wave nondestructive testing and evaluation - overview and recent advances," *IEEE Instrumentation Measurement Magazine*, vol. 10, no. 2, pp. 26–38, April 2007.

[2] D. Sheen, D. McMakin, and T. Hall, "Three-dimensional millimeter-wave imaging for concealed weapon detection," *IEEE Transactions on Microwave Theory and Techniques*, vol. 49, no. 9, pp. 1581–1592, Sep 2001.

[3] E. C. Fear, X. Li, S. C. Hagness, and M. A. Stuchly, "Confocal microwave imaging for breast cancer detection: localization of tumors in three dimensions," *IEEE Transactions on Biomedical Engineering*, vol. 49, no. 8, pp. 812–822, Aug 2002.

[4] A. Gonzalez-Ruiz and Y. Mostofi, "Cooperative robotic structure mapping using wireless measurements-a comparison of random and coordinated sampling patterns," *IEEE Sensors Journal*, vol. 13, no. 7, pp. 2571–2580, 2013.

[5] L. Zhang, Y. Hao, and C. Parini, "Millimetre wave imaging system parameters at 95 ghz," *IET Microwaves, Antennas Propagation*, vol. 5, no. 5, pp. 528–534, April 2011.

[6] W. M. Brown, "Synthetic aperture radar," *IEEE Transactions on Aerospace and*

*Electronic Systems*, vol. AES-3, no. 2, pp. 217–229, March 1967.

[7] S. Ahmed, A. Schiessl, and L. Schmidt, "A novel fully electronic active real-time imager based on a planar multistatic sparse array," *IEEE Transactions on Microwave Theory and Techniques*, vol. 59, no. 12, pp. 3567–3576, Dec 2011.

[8] S. Ahmed, A. Genghammer, A. Schiessl, and L.-P. Schmidt, "Fully electronic $e$-band personnel imager of 2 $m^2$ aperture based on a multistatic architecture," *IEEE Transactions on Microwave Theory and Techniques*, vol. 61, no. 1, pp. 651–657, Jan 2013.

[9] L. Qiao, Y. Wang, Z. Shen, Z. Zhao, and Z. Chen, "Compressive sensing for direct millimeter-wave holographic imaging," *Appl. Opt.*, vol. 54, no. 11, pp. 3280–3289, Apr 2015.

[10] X. Zhuge and A. G. Yarovoy, "Three-dimensional near-field MIMO array imaging using range migration techniques," *IEEE Transactions on Image Processing*, vol. 21, no. 6, pp. 3026–3033, June 2012.

[11] ——, "Study on two-dimensional sparse mimo uwb arrays for high resolution near-field imaging," *IEEE Transactions on Antennas and Propagation*, vol. 60, no. 9, pp. 4173–4182, Sept 2012.

[12] F. Gumbmann and L. P. Schmidt, "Millimeter-wave imaging with optimized sparse periodic array for short-range applications," *IEEE Transactions on Geoscience and Remote Sensing*, vol. 49, no. 10, pp. 3629–3638, Oct 2011.

[13] S. Patole and M. Torlak, "Two dimensional array imaging with beam steered data," *IEEE Transactions on Image Processing*, vol. 22, no. 12, pp. 5181–5189, Dec 2013.

[14] "L-3 provision 2," http://www.sds.l-3com.com/advancedimaging/provision-2.htm, 2016.

[15] J. Li, P. Stoica, and X. Zheng, "Signal synthesis and receiver design for mimo radar imaging," *IEEE Transactions on Signal Processing*, vol. 56, no. 8, pp. 3959–3968, Aug 2008.

[16] X. Zhuge and A. G. Yarovoy, "A sparse aperture mimo-sar-based uwb imaging system for concealed weapon detection," *IEEE Transactions on Geoscience and*

*Remote Sensing*, vol. 49, no. 1, pp. 509–518, 2011.

[17] C. Hu, J. Wang, W. Tian, T. Zeng, and R. Wang, "Design and imaging of ground-based multiple-input multiple-output synthetic aperture radar (mimo sar) with non-collinear arrays," *Sensors*, vol. 17, no. 3, 2017.

[18] X. Zhuge and A. G. Yarovoy, "Study on two-dimensional sparse mimo uwb arrays for high resolution near-field imaging," *IEEE Transactions on Antennas and Propagation*, vol. 60, no. 9, pp. 4173–4182, 2012.

[19] "London airport installs mm-wave security scanners from rohde & schwarz," https://www.everythingrf.com/News/details/3103-London-Airport-Installs-mm-Wave-Security-Scanners-from-Rohde-Schwarz, 2016.

[20] J. Li and P. Stoica, "The phased array is the maximum snr active array," *IEEE Signal Processing Magazine*, vol. 27, no. 2, pp. 143–144, 2010.

[21] R. Stolt, "Migration by fourier transform," *Geophysics*, vol. 43, no. 1, pp. 23–48, 1978.

[22] C. Cafforio, C. Prati, and F. Rocca, "Sar data focusing using seismic migration techniques," *IEEE transactions on aerospace and electronic systems*, vol. 27, no. 2, pp. 194–207, 1991.

[23] J. M. Lopez-Sanchez and J. Fortuny-Guasch, "3-d radar imaging using range migration techniques," *IEEE Transactions on Antennas and Propagation*, vol. 48, no. 5, pp. 728–737, May 2000.

[24] K. Mayer, R. Marklein, K. Langenberg, and T. Kreutter, "Three-dimensional imaging system based on fourier transform synthetic aperture focusing technique," *Ultrasonics*, vol. 28, no. 4, pp. 241–255, 1990.

[25] K. Langenberg, M. Brandfass, K. Mayer, T. Kreutter, A. Brüll, P. Felinger, and D. Huo, "Principles of microwave imaging and inverse scattering," *EARSeL Advances in Remote Sensing*, vol. 2, no. 1-I, pp. 163–186, 1993.

[26] J. W. Goodman, Ed., *Introduction to Fourier optics*. Roberts and Company Publishers, 2005.

[27] A. Boyer, P. Hirsch, J. Jordan Jr, L. Lesem, and D. Van Rooy, "Reconstruction of

ultrasonic images by backward propagation," in *Acoustical Holography.* Springer, 1971, pp. 333–348.

[28] L. Li, W. Zhang, and F. Li, "Derivation and discussion of the sar migration algorithm within inverse scattering problem: Theoretical analysis," *IEEE Transactions on Geoscience and Remote Sensing*, vol. 48, no. 1, pp. 415–422, Jan 2010.

# Chapter 3

# Compressive Sensing and its Application to Imaging

## 3.1 Introduction

Over the past few years, compressive sensing (CS) [1, 2], also known as compressed sensing or compressive sampling, has attracted considerable attention in the research areas of applied mathematics, computer science, and electronic engineering. This rapidly developing field of sparse signal recovery is already changing the way engineers think about data acquisition and reconstruction. The purpose of this chapter is to provide a general background on the CS theory and its application to radar imaging. Section 3.2 to Section 3.5 introduce the mathematical fundamentals of the CS in terms of signal sparsity, basic CS framework, properties of sensing matrix and CS recovery algorithms. Section 3.6 first introduces the framework of CS imaging and then presents a brief literature review of CS applied to radar imaging. Section 3.7 summarizes this chapter.

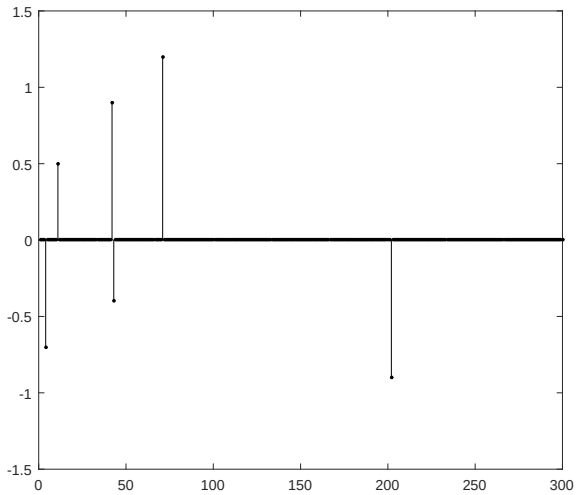


Figure 3.1: Example of a spares signal with only 6 non-zeros.

## 3.2 Sparsity and Compressibility

Sparse signals that having only a few nonzero entries, as shown in Figure 3.1, are of great importance in signal processing for the purpose of compression. Mathematically, a discrete signal $\mathbf{x} \in \mathbb{R}^n$ is said to be $k$-sparse, where $k \leq n$ and $k$ is an integer, if the support of $\mathbf{x}$, defined by $\text{supp}(\mathbf{x}) = \{i : x_i \neq 0\}$ contains at most $k$ indices. We define a set of $k$-sparse signals as:

$$\sum\nolimits_k = \{\mathbf{x} \in \mathbb{R}^n : |\text{supp}\,(\mathbf{x})| \leq k\}. \tag{3.1}$$

Sparsity can also be found in a canonical basis or transformed basis or a combination of bases. In such cases, the transform coefficients vector of the original signal is sparse. For example, a signal $\mathbf{x} \in \mathbb{R}^n$ which is sparse in a dictionary represented by an $m \times n$ matrix $\mathbf{\Psi}$ can be written as

$$\mathbf{x} = \sum\nolimits_{i=1}^{n} s_i \mathbf{\Psi}_i = \mathbf{\Psi}\mathbf{s}, \tag{3.2}$$

where $\mathbf{\Psi}_i$ are the column vectors of $\mathbf{\Psi}$, $\mathbf{s}$ is the sparse representation.

Typically, real-world signals are not exactly sparse in any orthogonal basis. Instead,

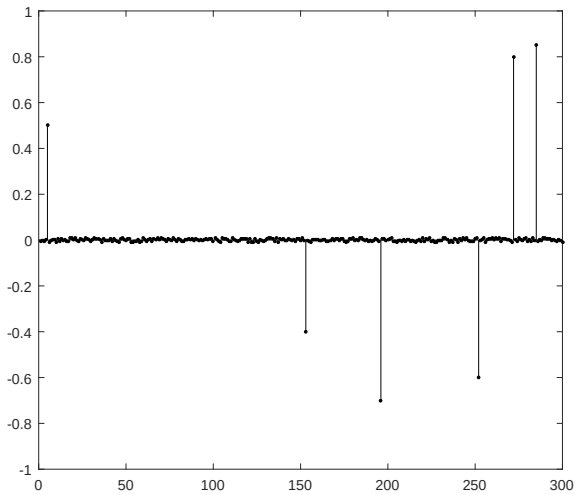


Figure 3.2: Example of a compressible signal.

most entries of these signals or their transform coefficients are approximately zero, as shown in Figure 3.2. Such signals are called compressible. For example, natural images are compressible through wavelet transformation. Specifically, a signal $\mathbf{x} \in \mathbb{R}^n$ is said to be compressible if the magnitudes of coefficient vector $\mathbf{s}$ sorted in decreasing order follow the power law $|s_i| \leq C_1 i^{-q}, i = 1, 2, \cdots, n$. The larger $q$ is, the faster the magnitudes decay, and the more compressible a signal is.

## 3.3 The Basic Framework of Compressive Sensing

In a traditional signal acquisition method, one measures the full length of a signal but only keeps the nonzero coefficients, thereby wasting many of the measurements. CS overcomes this issue by combining compression and sensing (measuring) at the same time. Moreover, it guarantees us to recover the signal from the under-sampled measurements. Suppose we have a signal $\mathbf{x} \in \mathbb{R}^n$, that is $k$-sparse in a basis (or a Dictionary) $\mathbf{\Psi}$, such that $\mathbf{x} = \mathbf{\Psi}\mathbf{s}$, with $\mathbf{s} \in \mathbb{R}^n$ being a $k$-sparse vector. In the case when $\mathbf{x}$ is compressible in $\mathbf{\Psi}$, it can be well approximated by the best $k$-term representation. Consider a random $m \times n$ sensing matrix $\mathbf{\Phi}$ with $m \ll n$, We observe a set of measurements $\mathbf{y} \in \mathbb{R}^m$ through

the following system:

$$\mathbf{y} = \mathbf{\Phi}\mathbf{x}. \tag{3.3}$$

Then we want to recover signal $\mathbf{x}$ from the measurements $\mathbf{y}$. By substituting $\mathbf{x} = \mathbf{\Psi}\mathbf{s}$ into (3.3) we have:

$$\mathbf{y} = \mathbf{\Phi}\mathbf{\Psi}\mathbf{s}. \tag{3.4}$$

We define $\mathbf{\Theta} = \mathbf{\Phi}\mathbf{\Psi}$ as the new sensing matrix and rewrite (3.4) as:

$$\mathbf{y} = \mathbf{\Theta}\mathbf{s}. \tag{3.5}$$

As $m < n$, the underdetermined system (3.5) admits infinitely many solutions. Ideally, we want to solve this underdetermined system of equations and find $\mathbf{s}$ that has the fewest number of non-zeros. The search of sparsest vector $\mathbf{s}$ then amounts to solving the following optimization problem

$$\min_{\mathbf{s}} \|\mathbf{s}\|_0 \;\; s.t. \;\; \mathbf{y} = \mathbf{\Theta}\mathbf{s}, \tag{3.6}$$

where $\|\cdot\|_0$ is the best measure of sparsity. That is, among infinitely many $\mathbf{s}$'s that satisfy $\mathbf{y} = \mathbf{\Theta}\mathbf{s}$, we choose the one that has the fewest nonzero components. However, $\|\cdot\|_0$ is not convex and it has been shown that the search for such an $\mathbf{s}$ is an NP hard problem that requires an exhaustive combination of all $\binom{n}{k}$ possible locations of the non-zero components of $\mathbf{s}$ [3]. Alternatively, we look for another measure for sparsity which is convex but still induces sparsity of $\mathbf{s}$ as close as possible to $\|\mathbf{s}\|_0$. The following optimization problem, known as Basis Pursuit (BP) [4], does exactly that.

$$\min_{\mathbf{s}} \|\mathbf{s}\|_1 \;\; s.t. \;\; \mathbf{y} = \mathbf{\Theta}\mathbf{s}, \tag{3.7}$$

where $\|\mathbf{s}\|_1 = \sum_{i=1}^{n} |s_i|$. The reason why the $\ell_1$ norm can promote sparsity is illustrated in Figure 3.3. Assuming an underdetermined system $\mathbf{y} = \mathbf{A}\mathbf{x}$, where the sparse signal $\mathbf{x} \in \mathbb{R}^2$. The solid lines represent the linear constraint and the dotted lines are the $\ell_p$-

ball with $p = 1$ and $p = 2$. Then the solution $\hat{\mathbf{x}}$ takes place at the intersection between the $\ell_p$-ball and $\mathbf{y} = \mathbf{A}\mathbf{x}$. It can be observed that the solution based on $\ell_1$-norm tends to be sparse as it's on the axis, whereas for the case with $\ell_2$-norm, the solution will have nonzero values for both elements in $\hat{\mathbf{x}}$. Although $\ell_p$-norm with $0 < p < 1$ can also introduce sparsity, they are not convex anymore. Therefore, the $\ell_1$ norm is the closest norm that makes the problem convex and still preserves the sparsity of the solution among others.

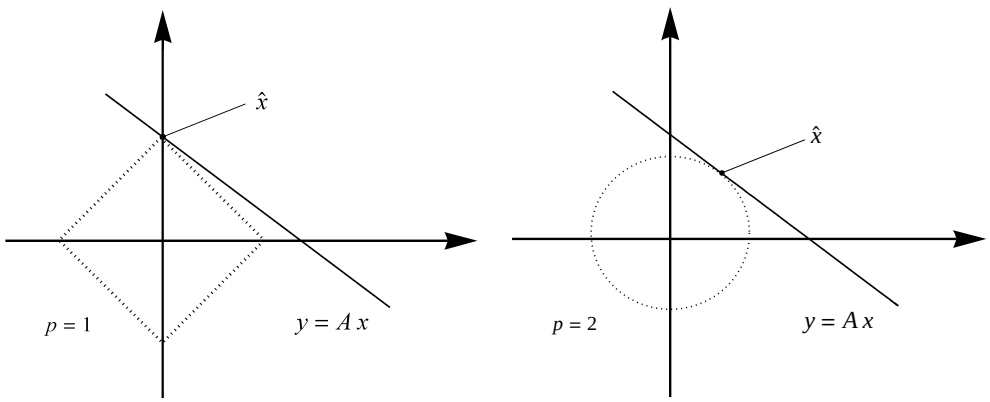


(a) (b)

Figure 3.3: Signal recovery using $\ell_p$-norm with (a) $p = 1$ and (b) $p = 2$.

The BP method in (3.7) is considered without noise, which is too ideal to be used in real scenarios. Considering the noise corrupted model: $\mathbf{y} = \mathbf{\Theta}\mathbf{s} + \eta$, where $\eta$ is the noise vector with bounded energy $\|\eta\|_2 \leq \epsilon$. The modified version of (3.7) is then given as:

$$\min_{\mathbf{s}} \|\mathbf{s}\|_1 \;\; s.t. \;\; \|\mathbf{\Theta}\mathbf{s} - \mathbf{y}\|_2 \leq \epsilon. \tag{3.8}$$

This modified optimization is known as basis pursuit with inequality constraints (BPIC). The Lagrangian relaxation of this quadratic program is written as

$$\min_{\mathbf{s}} \frac{1}{2}\|\mathbf{\Theta}\mathbf{s} - \mathbf{y}\|_2^2 + \lambda \|\mathbf{s}\|_1 , \tag{3.9}$$

and is known as basis pursuit denoising (BPDN). There exists many solvers to find

solutions for (3.6), (3.7), (3.8) and (3.9). They will be introduced later in this Chapter.

## 3.4 Properties of Sensing Matrix

Section 3.3 has provided several approaches for sparse signal recovery. However, whether or not the signal can be uniquely identified from its measurements $\mathbf{y} = \mathbf{\Theta}\mathbf{s}$ also depends on the property of the sensing matrix $\mathbf{\Theta}$. In other words, one has to carefully design the sensing matrix accordingly such that the reconstruction can be successful. This section describes how to evaluate the property of a sensing matrix in terms of the well-known spark, mutual coherence, and Restricted Isometry Property (RIP).

### 3.4.1 Spark

The definition of spark is described as follows.

**Definition 3.4.1.** *Let a matrix $\mathbf{\Theta} \in \mathbb{R}^{m\times n}$. The spark of the matrix $\mathbf{\Theta}$, denoted by spark($\mathbf{\Theta}$), is the smallest number of columns of that are linearly dependent [5].*

For instance, if a matrix $\mathbf{\Theta}$ has $r$ linearly independent columns, but there exists a subset of $r+1$ columns that are linearly dependent then $\text{spark}(\mathbf{\Theta}) = r+1$. Generally, the following relation holds for the spark and the rank of a matrix $\mathbf{\Theta} \in \mathbb{R}^{m\times n}$, with $m \geq 2$.

$$2 \leq \text{spark}(\mathbf{\Theta}) \leq \text{rank}(\mathbf{\Theta}) + 1. \tag{3.10}$$

This definition allows us to pose the following straightforward theorem that guarantees uniqueness of representation for $k$-sparse signals.

**Theorem 3.4.1.** *If $\text{spark}(\mathbf{\Theta}) > 2k$, then for each measurement vector there exists at most one signal $\mathbf{s}$ ($k$-sparse) such that $\mathbf{y} = \mathbf{\Theta}\mathbf{s}$.*

It is easy to see that for the $m \times n$ matrix $\mathbf{\Theta}$, $\text{spark}(\mathbf{\Theta}) \in [2, m+1]$. So, to make the solution unique, the number of measurements taken must satisfy $m \geq 2k$.

### 3.4.2 Mutual Coherence

While Theorem 3.4.1 guarantees uniqueness of the reconstruction, it is computational expensive to compute the spark of a general matrix, since one must verify that all sets of columns are linearly independent. On the contrary, the coherence property of the matrix $\mathbf{\Theta}$ provides an easily computable recovery guarantee [6].

**Definition 3.4.2.** *The mutual coherence of a matrix $\mathbf{\Theta}$, denoted as $\mu(\mathbf{\Theta})$, is the largest absolute normalized inner product between different columns of the matrix:*

$$\mu(\mathbf{\Theta}) = \max_{1 \leq i \neq j \leq n} \frac{\left|\theta_i^T \theta_j\right|}{\|\theta_i\|_2 \cdot \|\theta_j\|_2}, \tag{3.11}$$

*where $\theta_i$ is the $i$-th column of $\mathbf{\Theta}$.*

It can be shown that $\mu(\mathbf{\Theta}) \in \left[\sqrt{\frac{n-m}{m(n-1)}}, 1\right]$; the lower bound is known as Welch bound [7]. By applying the Gersgorin disk theorem [8] to the Gram matrix $\mathbf{G} = \mathbf{\Theta}_\Omega^T \mathbf{\Theta}_\Omega$, it is straightforward to obtain

$$\text{spark}(\mathbf{\Theta}) > 1 + \frac{1}{\mu(\mathbf{\Theta})}. \tag{3.12}$$

Therefore, we have the following condition on $\mathbf{\Theta}$ for the unique recovery.

**Theorem 3.4.2** ([9, 10])**.** *If*

$$k < \frac{1}{2}\left(1 + \frac{1}{\mu(\mathbf{\Theta})}\right), \tag{3.13}$$

*then for each measurement vector $\mathbf{y} \in \mathbb{R}^m$ there exists at most one signal $s \in \sum_k$ such that $\mathbf{y} = \mathbf{\Theta}\mathbf{s}$.*

### 3.4.3 Restricted Isometry Property

The previous two sensing matrix properties provide guarantees of uniqueness when the measurement vector is obtained without error. In practice, the measurement process is always accompanied with noise and system errors. In such scenarios, it is desirable to

have a property that allows us to guarantee that, for small enough noise, two sparse vectors that are far apart from each other cannot lead to the same (noisy) measurement vector [11]. The RIP is such a property that has been widely used for analysing the performance of a CS system [12].

**Definition 3.4.3.** *(Restricted Isometry Property (RIP)): A matrix* $\mathbf{\Theta} \in \mathbb{R}^{m \times n}$ *satisfies the RIP of order* $k$ *if there exists a constant* $\delta_k \in (0, 1)$ *such that*

$$(1 - \delta_k) \|\mathbf{s}\|_2^2 \leq \|\mathbf{\Theta}\mathbf{s}\|_2^2 \leq (1 + \delta_k) \|\mathbf{s}\|_2^2 , \tag{3.14}$$

*for any* $\mathbf{s} \in \sum_k$.

One implication of RIP is that if $\delta_{2k}$ is sufficiently small, then the sensing matrix $\mathbf{\Theta}$ preserves the distance between any pair of $k$-sparse signals. Therefore, we can bound the error of signal recovery when noise is present. In fact, if $\delta_{2k} < \sqrt{2} - 1$, then for some constants $c_1$ and $c_2$ the solution $\hat{\mathbf{s}}$ to the BPIC problem (3.8) satisfies [12, 13]

$$\|\hat{\mathbf{s}} - \mathbf{s}\|_2 \leq c_1 \frac{\|\mathbf{s} - \mathbf{s}_k\|_1}{\sqrt{k}} + c_2 \epsilon, \tag{3.15}$$

where $\mathbf{s}_k$ is the vector $\mathbf{s}$ with all but the largest $k$ elements set to zero. It should be noted that, although RIP provides strong guarantees for the recovery of $k$-sparse vectors, it is commonly impractical to check whether a sensing matrix satisfies the RIP due to the high computational complexity.

## 3.5 Recovery Algorithms

Recall that the CS framework is a sample and recover system, we now focus on solving the recovery problem. After acquiring the signal through the sensing matrix $\mathbf{\Phi}$, we get the measurement vector $\mathbf{y}$. Given signal $\mathbf{x}$ is sparse in transform basis $\mathbf{\Psi}$, we want to find a signal within the class of interest such that $\mathbf{y} = \mathbf{\Phi}\mathbf{x}$ exactly or approximately. There are two major algorithmic approaches to solve this underdetermined system: Greedy

pursuit [6] and Convex optimization [2]. In comparison, convex optimization algorithms require fewer measurements at the cost of higher computational complexity, especially when the signal dimension is large.

### 3.5.1 Convex Optimization

As stated in subsection 3.3, solving the $\ell_0$ minimization (3.6) directly is NP-hard. Alternatively, convex optimization algorithms relax (3.6) to a $\ell_1$ minimization (3.7). The convexity of $\ell_1$ norm makes it possible to reformulate the original problem as a linear programming problem, which is computational acceptable. There exists many algorithms that can solve $\ell_1$ minimization problems including (3.7), (3.8) and (3.9). These algorithms are based on different techniques such as linear programming methods [2], projected gradient methods [14], iterative shrinkage-threshold (IST) algorithm [15], alternating direction method of multipliers (ADMM) algorithms[16], etc. Table 3-A summarizes some well-known solvers that are capable of solving above three $\ell_1$ minimization problems. Most of these solvers offer online Matlab toolboxes. Particulary, two-step IST (TwIST) [17] and split augmented Lagrangian shrinkage algorithm (SALSA) [18] have been extensively used in this thesis as the imaging reconstruction algorithms. TwIST is a variant of the IST. The term two-step comes from the fact that the update equation depends on the two previous estimates rather than only on the previous one like conventional methods. This algorithm exhibits much faster convergence rate than IST for ill-conditioned problems [19]. SALSA is based on a variable splitting to obtain an equivalent constrained optimization formulation, which is then addressed using the ADMM method. According to [20], SALSA is consistently and considerably faster than the previous state of the art methods FISTA, TwIST, and SpaRSA.

Table 3-A: $\ell_1$ minimization problems and solvers

| Minimization problems | Solvers |
|---|---|
| $\min_{\mathbf{s}} \|\mathbf{s}\|_1 \;\; s.t. \;\; \mathbf{y} = \mathbf{\Theta s}$ | $\ell_1$-magic [21] |
| $\min_{\mathbf{s}} \|\mathbf{s}\|_1 \;\; s.t. \;\; \|\mathbf{\Theta s} - \mathbf{y}\|_2 \leq \epsilon$ | NESTA [22]<br>SPGL1 [23] |
| $\min_{\mathbf{s}} \frac{1}{2}\|\mathbf{\Theta s} - \mathbf{y}\|_2^2 + \lambda \|\mathbf{s}\|_1$ | FISTA [24]<br>FPC [25]<br>Bregman [26]<br>GPSR [14]<br>SpaRSA [27]<br>TwIST [19]<br>SALSA [20] |

### 3.5.2 Greedy Algorithms

While the convex optimization relies on the linear programming of the $\ell_1$ minimization (3.7), greedy algorithms aim to solve the $\ell_0$ minimization by iteratively refining the approximate solution of (3.6). The most common greedy algorithm for CS is the Orthogonal Matching Pursuit (OMP) [6]. Algorithm 1 gives a mathematical description of it. In each iteration, the column of $\mathbf{\Theta}$ that is most strongly correlated with the residual will be selected. The index of this column is recorded in the index set $\Omega$ which gives the indices of nonzero coefficients of the estimated sparse vector $\mathbf{s}$. Then the best coefficients for approximating $\mathbf{s}$ are computed by minimizing $\|\mathbf{\Theta}_\Omega \mathbf{s} - \mathbf{y}\|_2^2$ with respect to $\mathbf{s}$. Finally, the residual is updated by subtracting the contribution of the selected columns so far. Commonly, we set the stopping criterion as a fixed number usually the sparsity of the signal. We can also set a threshold when the residual has small magnitude: $\|\mathbf{r}_i\| \leq \epsilon$.

As we can see from the algorithm, OMP method greatly relies on the identification of the correct columns. In some cases, wrong columns are chosen in the first few iterations, and therefore the remaining iterations are spent on correcting the first few mistakes. This concept is also the basis of some other developed greedy algorithms such as Regularized OMP [28], Stagewise OMP [29], Compressive Sampling Matching Pursuit (CoSaMP) [30] and Subspace Pursuit [31].

**Algorithm 1** Orthogonal Matching Pursuit

**Input**: Measurement vector y, sensing matrix $\mathbf{\Theta} = \mathbf{\Phi}\mathbf{\Psi} \in \mathbb{R}^{m \times n}$

**1) Initialize**: Set the index set $\Omega_0 = \emptyset$, the residual $\mathbf{r}_0 = \mathbf{y}$, count number $i = 1$, $\mathbf{s}_0 = \mathbf{0}$.

**2) Identify**: Find a column $j$ of $\mathbf{\Theta}$ that is most strongly correlated with the residual:

$$j = \arg \max_{j=1,\cdots,n} |\langle \mathbf{r}_{i-1}, \theta_j \rangle| \text{ and update the index set: } \Omega_i = \Omega_{i-1} \cup \{j\}$$

**3) Estimate**: Find the best coefficients for approximating with the columns chosen so far subject to $\text{supp}\,(\mathbf{v}) = \Omega_i$

$$\mathbf{s}_i = \arg \min_{\mathbf{v}} \|\mathbf{y} - \mathbf{\Theta}_{\Omega_i}\mathbf{v}\|_2^2$$

**4) Iterate**: Update the residual and count number:

$$\mathbf{r}_i = \mathbf{y} - \mathbf{\Theta}_{\Omega_i}\mathbf{s}_i$$
$$i = i + 1$$

Repeat (2)-(4) until stopping criterion holds.

**Output**: Return the estimation $\mathbf{s}$ with components $\mathbf{s}(k) = \mathbf{s}_i(k)$ for $k \in \Omega_i$ and $\mathbf{s}(k) = 0$ otherwise.

### 3.5.3 Probabilistic Methods

Convex optimization and greedy algorithms are computationally practical and give provably correct solutions under well-defined conditions. However, it is important to note that the validity of widely adopted RIP assumptions in these approaches, cannot be always granted in many engineering problems, whose properties are often constrained by the underlying physics [32]. Under such circumstances, the use of these approaches may not be an optimal choice.

Recently, a probabilistic CS method that does not rely on the RIP of the sensing matrix to yield accurate and stable results has been proposed [33]. This method introduces the sparse Bayesian learning to CS signal reconstruction and outperforms traditional deterministic reconstruction approaches. Apart from the advantage of dealing with RIP violated sensing matrix, Bayesian CS (BCS) methods can also provide an estimation on the confidence level of the estimated solution. Moreover, the multi-task version of the BCS can be utilized to solve complex-valued CS applications in the

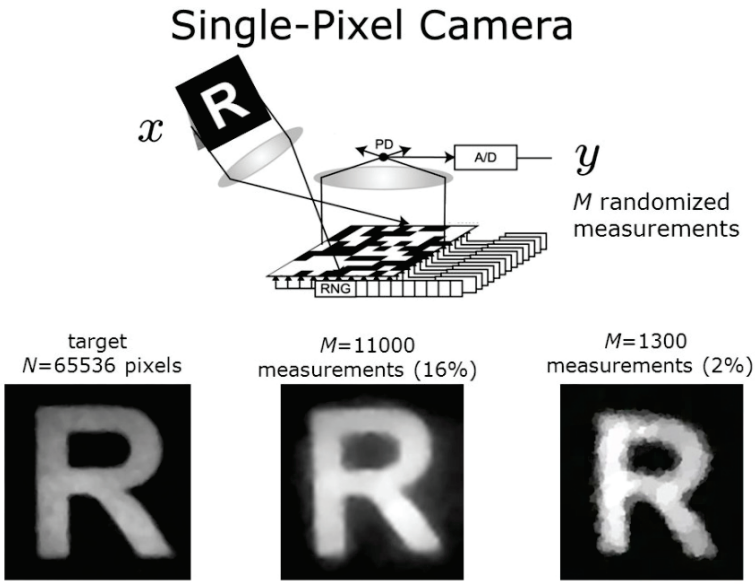


Figure 3.4: Single-pixel camera and data under-sampling.

multiple measurement vectors (MMV) framework [34], which can be more efficient than solving the real and imaginary parts separately. Although BCS methods do not currently offer theoretical guarantees, they have been successfully applied and verified in many EM problems where RIP cannot be satisfied, for instance, sparse array synthesis [35, 36], array diagnosis [37] and inverse scattering [38–41].

## 3.6 Compressive Sensing for Imaging Applications

### 3.6.1 Compressive Sensing Implementation in Array Imaging

Natural images are compressible by sparse representations such as those from a wavelet transform and discrete cosine transform (DCT). The ability to recover under-sampled sparse signals makes CS a perfect tool for designing novel imaging systems. One of the most well known CS imaging system is the single-pixel CS camera developed in Rice University [42]. As shown in Figure 3.4, this new imaging architecture combines sampling and compression into a single non-adaptive linear measurement process. Rather than using an array of imaging sensors to measure the scene, the CS camera uses a single sensor

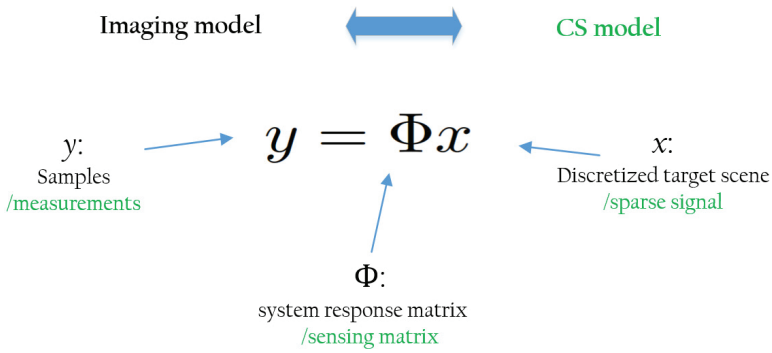


Figure 3.5: From imaging model to CS model.

to measure inner products between the scene and a set of test functions. By randomly choosing these test functions, the CS theory enables stable reconstruction from fewer measurements than the number of reconstructed pixels. In this manner, sub-Nyquist data acquisition has been achieved in the imaging system.

The single-pixel camera is just one example of many CS imaging applications. Due to the distinct theories and physical limitations behind different imaging systems, their ways of incorporating CS can vary a lot. Recall that the CS framework can be simplified as $y = \Phi x$, where $y$ is the measurements, $\Phi$ is the sensing matrix and $x$ is the sparse signal. For any imaging system, if its forward imaging model can be reformulated in a similar way like the CS model, then we can solve for the unknown $x$ using CS algorithms. Figure 3.5 illustrates such a transformation from traditional imaging to CS imaging. Clearly, apart from vectorizing and discretizing the measured samples and target scene, the most crucial part of CS imaging is to reformulate the system responses into a matrix form that serves as the sensing matrix.

The primary goal of this thesis is to investigate the CS implementation in array imaging systems for security applications. In essence, we are trying to reformulate the original imaging models of different array systems into a CS-like model. Unlike the single-pixel CS camera that utilizes a spatial light modulator to build a totally different imaging device, we focus our research on the CS implementation in existing array systems without altering the hardware. In this regard, the main difference in applying CS to the

three array configurations introduced in Chapter 2 lies in the construction of the system response matrix. Specifically, the difference comes from the different array geometries and antenna patterns. For instance, in the switched array system, the response matrix is mainly determined by the location arrangement of the transceiver antennas. Similarly, in the MIMO array, the response matrix is determined by the design of transmit sub-array and receive sub-array. However, in the phased array, the response matrix is determined by not only the array geometry but also the used array patterns in the beamforming process. According to the CS theory, the well condition of these response matrices will play an important role in the latter image reconstruction process.

### 3.6.2 Compressive Sensing for Radar Imaging

During the past few years, CS theory has been successfully applied to a wide range of radar imaging applications including; terahertz imaging [43–45], MMW imaging [46–49], SAR imaging [50–58], through-wall imaging [59, 60], medical imaging [61, 62] and even inverse scattering [40, 41, 63].

Among these CS methods, there are basically two ways to implement the CS framework. The first is to utilize the conventional FT reconstruction algorithms. Specifically, in [48], CS was adopted in single frequency MMW indirect holographic imaging to reduce spatial sampling data. FT based forward and backward operators were used instead of matrix multiplication in each CS iteration. Three-dimensional imaging from 2-D scanning data was realized by applying total variation (TV) regularization. The same strategy was then extended to 2-D direct MMW holography where both the amplitude and phase are acquired for image reconstruction [49]. As opposed to the indirect holography, the processed data for direct holography and typical radar imaging is complex-valued and thus needs special care to explore image sparsity. In the mean time, this FT and CS combination concept has also been used in wide-band 3-D SAR imaging systems [56–58]. The main difference is the single frequency 2-D FT forward and backward operators have been replaced by their multi-frequency 3-D versions. As these methods share the same

principal on combining existing FT imaging models with CS theory, they are referred to as the Fourier transform based CS (FT-CS) method in this thesis. The FT-CS method inherits the computational efficiency from FFT and thus is capable of real-time image reconstruction.

While the FT-CS method greatly relies on FT reconstruction algorithms, a more direct way is to integrate the forward imaging model into the classic CS framework. This is simply done by reformulating the forward imaging model into a matrix form. In [51], CS was introduced to stepped frequency GPSs for compressed data acquisition both in frequency dimension and spatial dimension. The same idea was later applied to 2-D SAR imaging in [52] and [53]. We refer to this kind of CS methods as the direct CS (D-CS) method in our thesis. Since the D-CS imaging model is a straightforward expansion of the scattering model, it can be easily implemented for different scanning apertures, e.g., planar aperture, circular aperture and cylindrical aperture. However, the main drawback is the high computational complexity since 2-D data or 3-D data has to be vectorized during the algorithm implementation. In [54], a low complexity 3-D imaging method was presented. The complexity reduction is based on small bandwidth and narrow-angle measurement assumption which makes the multi-dimensional scattered data becomes separable and thus can be processed with Kronecker CS [55]. Another attempt to reduce complexity was made in [64] for multiple frequency 2-D imaging. A near-field approximation of the distance from antenna to each scattering center was proposed to make the angularly sampled data separable for 2-D FFT operation. However, as these two methods rely on single transceiver to scan with very small angle interval and frequency interval, they become invalid in other scanning apertures like planar aperture in personnel imaging.

Both FT-CS and D-CS methods have their pros and cons. The detailed performance the two methods will be discussed in the next chapter in the context of switched array imaging.

## 3.7 Summary

This chapter first presents the mathematical foundation of the CS theory, including sparsity, CS framework and sensing matrix. Then the state of the art recovery algorithms are briefly explained and summarized. Finally, CS imaging applications are discussed and summarized.

## References

[1] D. Donoho, "Compressed sensing," *IEEE Transactions on Information Theory*, vol. 52, no. 4, pp. 1289–1306, April 2006.

[2] E. Candes, J. Romberg, and T. Tao, "Robust uncertainty principles: exact signal reconstruction from highly incomplete frequency information," *IEEE Transactions on Information Theory*, vol. 52, no. 2, pp. 489–509, Feb 2006.

[3] B. K. Natarajan, "Sparse approximate solutions to linear systems," *SIAM Journal on Computing*, vol. 24, no. 2, pp. 227–234, 1995.

[4] S. S. Chen, D. L. Donoho, and M. A. Saunders, "Atomic decomposition by basis pursuit," *SIAM journal on scientific computing*, vol. 20, no. 1, pp. 33–61, 1998.

[5] D. L. Donoho and M. Elad, "Optimally sparse representation in general (nonorthogonal) dictionaries via $\ell_1$ minimization," *Proceedings of the National Academy of Sciences*, vol. 100, no. 5, pp. 2197–2202, 2003.

[6] J. Tropp and A. Gilbert, "Signal recovery from random measurements via orthogonal matching pursuit," *IEEE Transactions on Information Theory*, vol. 53, no. 12, pp. 4655–4666, Dec 2007.

[7] L. Welch, "Lower bounds on the maximum cross correlation of signals (Corresp.)," *IEEE Transactions on Information Theory*, vol. 20, pp. 397–399, 1974.

[8] S. Gershgorin, "Ueber die Abgrenzung der Eigenwerte einer Matrix," *Izv. Akad. Nauk. SSSR Ser. Mat.*, vol. 1, pp. 749–754, 1931.

[9] J. a. Tropp, "Greed is good: Algorithmic results for sparse approximation," *IEEE*

*Transactions on Information Theory*, vol. 50, no. 10, pp. 2231–2242, 2004.

[10] R. Gribonval and M. Nielsen, "Sparse representations in unions of bases," *IEEE Transactions on Information Theory*, vol. 49, no. 12, pp. 3320–3325, 2003.

[11] M. F. Duarte and Y. C. Eldar, "Structured compressed sensing: From theory to applications," *IEEE Transactions on Signal Processing*, vol. 59, no. 9, pp. 4053–4085, 2011.

[12] E. J. Candès, "The restricted isometry property and its implications for compressed sensing," *Comptes Rendus Mathematique*, vol. 346, no. 910, pp. 589 – 592, 2008.

[13] H. Huang, S. Misra, W. Tang, H. Barani, and H. Al-Azzawi, "Applications of compressed sensing in communications networks," *arXiv preprint arXiv:1305.3002*, 2013.

[14] M. A. T. Figueiredo, R. D. Nowak, and S. J. Wright, "Gradient projection for sparse reconstruction: Application to compressed sensing and other inverse problems," *IEEE Journal on Selected Topics in Signal Processing*, vol. 1, no. 4, pp. 586–597, 2007.

[15] I. Daubechies, M. Defrise, and C. De Mol, "An iterative thresholding algorithm for linear inverse problems with a sparsity constraint," *Communications on Pure and Applied Mathematics*, vol. 57, no. 11, pp. 1413–1457, 2004.

[16] J. Eckstein and D. P. Bertsekas, "On the douglasrachford splitting method and the proximal point algorithm for maximal monotone operators," *Mathematical Programming*, vol. 55, no. 1, pp. 293–318, 1992.

[17] J. M. Bioucas-Dias and M. A. Figueiredo, "Two-step iterative shrinkage/thresholding algorithm for linear inverse problems," http://www.lx.it.pt/~bioucas/TwIST/TwIST.htm, 2007.

[18] M. V. Afonso, J. M. Bioucas-Dias, and M. A. Figueiredo, "Split augmented lagrangian shrinkage algorithm," http://cascais.lx.it.pt/~mafonso/salsa.html, 2010.

[19] J. M. Bioucas-Dias and M. A. Figueiredo, "A new twist: two-step iterative shrinkage/thresholding algorithms for image restoration," *IEEE Transactions on*

*Image Processing*, vol. 16, no. 12, pp. 2992–3004, 2007.

[20] M. V. Afonso, J. M. Bioucas-Dias, and M. A. Figueiredo, "Fast image recovery using variable splitting and constrained optimization," *IEEE Transactions on Image Processing*, vol. 19, no. 9, pp. 2345–2356, 2010.

[21] E. Cand'es and J. Romberg, "$\ell_1$ magic: Matlab software," http://users.ece.gatech.edu/justin/l1magic/, Mar. 2005.

[22] S. Becker, J. Bobin, and E. J. Candès, "Nesta: A fast and accurate first-order method for sparse recovery," *SIAM Journal on Imaging Sciences*, vol. 4, no. 1, pp. 1–39, 2011.

[23] E. Van Den Berg and M. P. Friedlander, "Probing the pareto frontier for basis pursuit solutions," *SIAM Journal on Scientific Computing*, vol. 31, no. 2, pp. 890–912, 2008.

[24] A. Beck and M. Teboulle, "A fast iterative shrinkage-thresholding algorithm for linear inverse problems," *SIAM journal on imaging sciences*, vol. 2, no. 1, pp. 183–202, 2009.

[25] E. T. Hale, W. Yin, and Y. Zhang, "Fixed-point continuation for $\ell_1$-minimization: Methodology and convergence," *SIAM Journal on Optimization*, vol. 19, no. 3, pp. 1107–1130, 2008.

[26] W. Yin, S. Osher, D. Goldfarb, and J. Darbon, "Bregman iterative algorithms for $\ell_1$-minimization with applications to compressed sensing," *SIAM Journal on Imaging sciences*, vol. 1, no. 1, pp. 143–168, 2008.

[27] S. J. Wright, R. D. Nowak, and M. A. Figueiredo, "Sparse reconstruction by separable approximation," *IEEE Transactions on Signal Processing*, vol. 57, no. 7, pp. 2479–2493, 2009.

[28] D. Needell and R. Vershynin, "Uniform uncertainty principle and signal recovery via regularized orthogonal matching pursuit," *Foundations of Computational Mathematics*, vol. 9, no. 3, pp. 317–334, 2009.

[29] D. L. Donoho, Y. Tsaig, I. Drori, and J. L. Starck, "Sparse solution of underdetermined systems of linear equations by stagewise orthogonal matching pursuit," *IEEE Transactions on Information Theory*, vol. 58, no. 2, pp.

1094–1121, 2012.

[30] D. Needell and J. a. Tropp, "CoSaMP: Iterative signal recovery from incomplete and inaccurate samples," *Applied and Computational Harmonic Analysis*, vol. 26, no. 3, pp. 301–321, 2009.

[31] W. Dai and O. Milenkovic, "Subspace pursuit for compressive sensing signal reconstruction," *IEEE Transactions on Information Theory*, vol. 55, no. 5, pp. 2230–2249, 2009.

[32] A. Massa, P. Rocca, and G. Oliveri, "Compressive sensing in electromagnetics - a review," *IEEE Antennas and Propagation Magazine*, vol. 57, no. 1, pp. 224–238, Feb 2015.

[33] S. Ji, Y. Xue, and L. Carin, "Bayesian compressive sensing," *IEEE Transactions on Signal Processing*, vol. 56, no. 6, pp. 2346–2356, 2008.

[34] S. Ji, D. Dunson, and L. Carin, "Multitask compressive sensing," *IEEE Transactions on Signal Processing*, vol. 57, no. 1, pp. 92–106, 2009.

[35] G. Oliveri and A. Massa, "Bayesian compressive sampling for pattern synthesis with maximally sparse non-uniform linear arrays," *IEEE Transactions on Antennas and Propagation*, vol. 59, no. 2, pp. 467–481, 2011.

[36] G. Oliveri, M. Carlin, and A. Massa, "Complex-weight sparse linear array synthesis by bayesian compressive sampling," *IEEE Transactions on Antennas and Propagation*, vol. 60, no. 5, pp. 2309–2326, 2012.

[37] G. Oliveri, P. Rocca, and A. Massa, "Reliable diagnosis of large linear arraysa bayesian compressive sensing approach," *IEEE Transactions on Antennas and Propagation*, vol. 60, no. 10, pp. 4627–4636, 2012.

[38] L. Poli, G. Oliveri, and A. Massa, "Microwave imaging within the first-order born approximation by means of the contrast-field bayesian compressive sensing," *IEEE Transactions on Antennas and Propagation*, vol. 60, no. 6, pp. 2865–2879, 2012.

[39] G. Oliveri, L. Poli, P. Rocca, and A. Massa, "Bayesian compressive optical imaging within the rytov approximation," *Optics Letters*, vol. 37, no. 10, pp. 1760–1762, 2012.

[40] L. Poli, G. Oliveri, P. Rocca, and A. Massa, "Bayesian compressive sensing

approaches for the reconstruction of two-dimensional sparse scatterers under te illuminations," *IEEE Transactions on Geoscience and Remote Sensing*, vol. 51, no. 5, pp. 2920–2936, May 2013.

[41] G. Oliveri, N. Anselmi, and A. Massa, "Compressive sensing imaging of non-sparse 2d scatterers by a total-variation approach within the born approximation," *IEEE Transactions on Antennas and Propagation*, vol. 62, no. 10, pp. 5157–5170, Oct 2014.

[42] M. F. Duarte, M. A. Davenport, D. Takhar, J. N. Laska, T. Sun, K. F. Kelly, and R. G. Baraniuk, "Single-pixel imaging via compressive sampling," *IEEE Signal Processing Magazine*, vol. 25, no. 2, pp. 83–91, March 2008.

[43] W. L. Chan, K. Charan, D. Takhar, K. F. Kelly, R. G. Baraniuk, and D. M. Mittleman, "A single-pixel terahertz imaging system based on compressed sensing," *Applied Physics Letters*, vol. 93, no. 12, p. 121105, 2008.

[44] W. L. Chan, M. L. Moravec, R. G. Baraniuk, and D. M. Mittleman, "Terahertz imaging with compressed sensing and phase retrieval," *Optics letters*, vol. 33, no. 9, pp. 974–976, 2008.

[45] W. L. Chan, H.-T. Chen, A. J. Taylor, I. Brener, M. J. Cich, and D. M. Mittleman, "A spatial light modulator for terahertz beams," *Applied Physics Letters*, vol. 94, no. 21, p. 213511, 2009.

[46] L. Spinoulas, J. Qi, A. K. Katsaggelos, T. W. Elmer, N. Gopalsami, and A. C. Raptis, "Optimized compressive sampling for passive millimeter-wave imaging," *Appl. Opt.*, vol. 51, no. 26, pp. 6335–6342, Sep 2012.

[47] V. M. Patel and J. N. Mait, "Compressive passive millimeter wave imaging with extended depth of field," *Optical Engineering*, vol. 51, no. 9, pp. 091 610–1–091 610–7, 2012.

[48] C. F. Cull, D. A. Wikner, J. N. Mait, M. Mattheiss, and D. J. Brady, "Millimeter-wave compressive holography," *Appl. Opt.*, vol. 49, no. 19, pp. E67–E82, Jul 2010.

[49] L. Qiao, Y. Wang, Z. Shen, Z. Zhao, and Z. Chen, "Compressive sensing for direct millimeter-wave holographic imaging," *Appl. Opt.*, vol. 54, no. 11, pp. 3280–3289,

Apr 2015.

[50] R. Baraniuk and P. Steeghs, "Compressive radar imaging," in *2007 IEEE Radar Conference*, April 2007, pp. 128–133.

[51] A. Gurbuz, J. McClellan, and W. Scott, "A compressive sensing data acquisition and imaging method for stepped frequency gprs," *IEEE Transactions on Signal Processing*, vol. 57, no. 7, pp. 2640–2650, July 2009.

[52] V. Patel, G. Easley, J. Healy, D.M., and R. Chellappa, "Compressed synthetic aperture radar," *IEEE Journal of Selected Topics in Signal Processing*, vol. 4, no. 2, pp. 244–254, April 2010.

[53] J. Yang, J. Thompson, X. Huang, T. Jin, and Z. Zhou, "Random-frequency sar imaging based on compressed sensing," *IEEE Transactions on Geoscience and Remote Sensing*, vol. 51, no. 2, pp. 983–994, 2013.

[54] W. Qiu, J. Zhou, H. Zhao, and Q. Fu, "Three-dimensional sparse turntable microwave imaging based on compressive sensing," *IEEE Geoscience and Remote Sensing Letters*, vol. 12, no. 4, pp. 826–830, April 2015.

[55] M. Duarte and R. Baraniuk, "Kronecker compressive sensing," *IEEE Transactions on Image Processing*, vol. 21, no. 2, pp. 494–504, Feb 2012.

[56] Z. Yang and Y. Zheng, "Near-field 3-d synthetic aperture radar imaging via compressed sensing," in *2012 IEEE International Conference on Acoustics, Speech and Signal Processing (ICASSP)*, March 2012, pp. 2513–2516.

[57] H. Kajbaf, J. T. Case, Z. Yang, and Y. R. Zheng, "Compressed sensing for sar-based wideband three-dimensional microwave imaging system using non-uniform fast fourier transform," *IET Radar, Sonar & Navigation*, vol. 7, no. 6, pp. 658–670, 2013.

[58] D. Liu and P. Boufounos, "Compressive sensing based 3d sar imaging with multi-prf baselines," in *2014 IEEE International Geoscience and Remote Sensing Symposium (IGARSS)*, July 2014, pp. 1301–1304.

[59] Q. Huang, L. Qu, B. Wu, and G. Fang, "UWB through-wall imaging based on compressive sensing," *IEEE Transactions on Geoscience and Remote Sensing*, vol. 48, no. 3 PART2, pp. 1408–1415, 2010.

[60] A. Gonzalez-Ruiz and Y. Mostofi, "Cooperative robotic structure mapping using wireless measurements-a comparison of random and coordinated sampling patterns," *IEEE Sensors Journal*, vol. 13, no. 7, pp. 2571–2580, 2013.

[61] M. Lustig, D. Donoho, and J. M. Pauly, "Sparse mri: The application of compressed sensing for rapid mr imaging," *Magnetic resonance in medicine*, vol. 58, no. 6, pp. 1182–1195, 2007.

[62] J. Haldar, D. Hernando, and Z.-P. Liang, "Compressed-sensing mri with random encoding," *IEEE Transactions on Medical Imaging*, vol. 30, no. 4, pp. 893–903, April 2011.

[63] L. Carin, D. Liu, W. Lin, and B. Guo, "Compressive sensing for multi-static scattering analysis," *Journal of Computational Physics*, vol. 228, no. 9, pp. 3464–3477, 2009.

[64] S. Li, G. Zhao, H. Li, B. Ren, W. Hu, Y. Liu, W. Yu, and H. Sun, "Near-field radar imaging via compressive sensing," *IEEE Transactions on Antennas and Propagation*, vol. 63, no. 2, pp. 828–833, Feb 2015.

# Chapter 4

# Compressive Sensing for Switched Array Imaging

## 4.1 Introduction

A practical imaging system for security scanning will undoubtedly adopt antenna array over single transceiver for the remarkably reduced scanning time. Applying CS techniques to array imaging systems is very different from applying them to single transceiver systems like SAR imaging. Firstly, to realize an antenna array such that the under-sampling pattern can be completely arbitrary is not practical. Because the array elements are fixed on a platform, the under-sampling pattern should be designed according to the feeding locations of the array elements. Secondly, CS methods enables sub-Nyquist sampling by randomly under-sampling the locations on a full grid that satisfy the Nyquist criterion. However, due to many physical limitations, the engineering realization of such an antenna array is quite challenging. Commonly, a tradeoff is to increase the array element spacing, which is to say the full sampled data already violates the Nyquist criterion.

To the authors' knowledge, existing D-CS methods that have been extensively studied

for wideband 2-D imaging and 3-D imaging is rarely mentioned in a near-field switched array for security imaging. These CS-SAR literature claims D-CS methods have much better efficiency than traditional Fourier based methods due to their random under-sampling feature. Considering the aforementioned practical conditions, this may not be the case for antenna array imaging systems when Fourier based methods are combined with the CS theory. More importantly, many papers only give sparse targets comparison between CS methods and Fourier methods with oversimplified qualitative results. Therefore, the objective of this chapter is to evaluate the FT-CS method and the D-CS method in near-field switched array imaging systems and find an efficient way that aims at less imaging time and better image quality.

This chapter first gives the single frequency 2-D forward imaging model for switched array in Section 4.2. The CS implementation to this model is then discussed in Section 4.3. Section 4.4 demonstrates the numerical analysis of the two CS methods and the conventional FT method. Experimental verification is presented in Section 4.5 while conclusions are drawn in Section 4.6.

## 4.2 Switched Array 2-D Forward Imaging Model

As we are more interested in the image reconstruction in the two cross-range dimensions, we simplify our question by considering 2-D cross-range imaging with single frequency data. Similar to the algorithm introduced in Chapter 2, we assume the transceiver is at position $(x', y', 0)$ and a general point $(x, y, z_0)$ is at the target plane. The reflectivity function of the target plane is characterized by $g(x, y, z_0)$. Under the BA and ignoring the amplitude attenuation, the scattering field at the transceiver can be approximately represented by

$$s(x', y') = \iint g(x, y) \exp(-j2kR)\, dx\, dy, \tag{4.1}$$

where $R = [(x - x')^2 + (y - y')^2 + (z_0 - 0)^2]^{1/2}$, $k_0 = 2\pi f_0/c$ is the wavenumber, $f_0$ is the adopted frequency and $c$ is the speed of light.

To avoid aliasing in image reconstruction, the sampling interval has to satisfy the Nyquist theorem during the data acquisition process. This sampling interval is determined by a number of factors including the wavelength $\lambda$, antenna beamwidth $\theta_a$, aperture size $L$, target size and aperture-to-target distance $D$. Although there is no good criterion so far with strict mathematical formulation considering these physical parameters for near field imaging systems, Joseph *et al.* [1] has suggested that the optimal sampling interval should be smaller than the theoretical resolution in order to achieve it. The theoretical cross-range resolution of the switched array imaging system can also can be expressed as

$$\delta \approx \frac{\lambda}{4\sin(\theta/2)}|\theta = \min(\theta_a, \theta_b), \tag{4.2}$$

where $\theta_b = 2\arctan(L/2D)$ is the angle subtended by the scanning aperture.

## 4.3 Compressive Sensing Implementation to Switched Array

CS based approaches enable image reconstruction from far fewer measurements by just randomly measuring a small fraction of positions on the scanning aperture. The D-CS and FT-CS methods for switched array will be introduced in this section.

### 4.3.1 D-CS Model

The D-CS model can be directly derived from the signal model in (4.1) by discretizing the target plane into a grid of point scatterers and then reshape the switched array signal matrix and reflectivity function matrix into long 1-D column vectors. Therefore, the 2-D imaging problem can be solved using standard 1-D CS reconstruction algorithms. Suppose the target plane reflectivity function $\mathbf{g}$ is discretized as a $P \times Q$ matrix $\mathbf{G}$ and the array signal matrix $\mathbf{S}$ has $M \times N$ sampling positions, as shown in Figure 4.1.

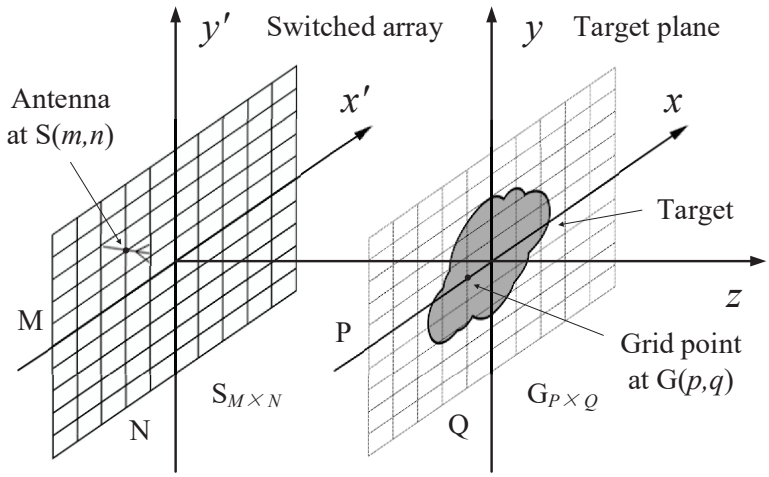


Figure 4.1: Switched array imaging system.

According to (4.1), a discrete version of $s(x, y)$ can be represented as

$$\mathbf{S}(m, n) = \sum_{p=1}^{P} \sum_{q=1}^{Q} \mathbf{G}(p, q) \exp(-j2kR(m, n, p, q)), \tag{4.3}$$

where $\mathbf{S}(m, n)$ is the received signal of the antenna at the $m$-th row and $n$-th column of $\mathbf{S}$ and $\mathbf{G}(p, q)$ is the reflectivity of the grid point at the $p$-th row and $q$-th column of $\mathbf{G}$. $R(m, n, p, q)$ is the distance between the antenna at $\mathbf{S}(m, n)$ and the grid point at $\mathbf{G}(p, q)$. By vectorizing $\mathbf{S}$ and $\mathbf{G}$, e.g., concatenating the columns of a matrix into a single column, (4.3) can be reformulated as

$$\mathbf{s} = \mathbf{H}\mathbf{g}$$

$$\begin{bmatrix} s(1,1) \\ \vdots \\ s(M,1) \\ \vdots \\ s(1,N) \\ \vdots \\ s(M,N) \end{bmatrix} = \begin{bmatrix} \mathbf{H}(1,1)^T \\ \vdots \\ \mathbf{H}(M,1)^T \\ \vdots \\ \mathbf{H}(1,N)^T \\ \vdots \\ \mathbf{H}(M,N)^T \end{bmatrix} \begin{bmatrix} g(1,1) \\ \vdots \\ g(P,1) \\ \vdots \\ g(1,Q) \\ \vdots \\ g(P,Q) \end{bmatrix}, \tag{4.4}$$

where

$$\mathbf{H}(m,n) = [\exp(-j2kR(m,n,1,1)),\ldots,\exp(-j2kR(m,n,P,1)),\ldots,$$
$$\exp(-j2kR(m,n,1,Q)),\ldots,\exp(-j2kR(m,n,P,Q))]^T,$$

and $\mathbf{H}$ is the system response matrix.

Suppose we are using a single transceiver system, the total number of measurements can be reduced by programming the transceiver to randomly sampling a fraction of all the positions on the grid. Mathematically, this amounts to introducing a binary mask as

$$\mathbf{Y} = \mathbf{B} \circ \mathbf{S}, \tag{4.5}$$

where $\circ$ represents the Hadamard product (element-wise multiplication), $\mathbf{Y}$ is the under-sampled data and $\mathbf{S}$ is the fully sampled data. Binary mask $\mathbf{B}$ is an $M \times N$ sampling matrix which only contains 1 (sample) and 0 (ignore). Suppose the number of sampled points is $K$, then the sampling rate can be computed as the ratio of $K$ to $MN$. Before applying reconstruction, $\mathbf{B}$ needs to be transformed to fit the vectorized $\mathbf{S}$. We denote by $\mathbf{A}$ the transformed version of $\mathbf{B}$. Then the vectorized under-sampling process can be summarized as

$$\mathbf{y} = \mathbf{A}\mathbf{s} = \mathbf{A}\mathbf{H}\mathbf{g}, \tag{4.6}$$

where $\mathbf{y}$ is the $K \times 1$ vector representation of $\mathbf{Y}$ and $\mathbf{A}$ is a $K \times MN$ matrix.

The resolution of the reconstructed image is directly related to the discretization of the target plane. Intuitively, finer grid size will provide higher resolution. However, this operation leads to significantly increased size of $\mathbf{H}$ and thus introduce higher computational complexity. This problem gets more serious when dealing with 3-D ($x-$dimension, $y-$dimension and frequency dimension) data. Complexity reduction methods based on small angular scanning aperture with different approximations of the scattered data [2, 3] become invalid here since in the case of planar scanning aperture, the square root phase

term cannot be easily separated. In addition to the increased complexity, finer grids will also weaken the performance of CS reconstruction. Firstly, as can be seen from (4.4), the only difference among the entries in $\mathbf{H}$ is the distance $R$, which means the closer the adjacent points on the grid, the more similarities among the columns in $\mathbf{H}$. In the CS framework, more similar columns means higher mutual coherence [4], which should always be avoided. Secondly, finer grids will increase the number of unknowns and thus require more measurements for stable CS reconstruction. This analysis will also be discussed later with simulation results.

### 4.3.2 FT-CS Model

The FT-CS model is based on the conventional BP algorithm that takes advantage of the FFT. Similar to the D-CS model, all data for the FT-CS model must be vectorized before applying recovery algorithms. Such vectorization process introduce unnecessary complexity and memory requirement in algorithm deployment. Alternatively, we can directly use the matrix formulation in computation if the forward operator and backward operator can be utilized.

The forward process in (4.1) can also be written as

$$s(x, y) = \mathrm{FT}_{2D}^{-1}[\mathrm{FT}_{2D}[g(x, y)] \exp(jk_z z_0)]. \tag{4.7}$$

To better describe the FT-CS method, we denote the forward process in (4.7) as

$$\mathbf{S} = \mathbf{O}[\mathbf{G}], \tag{4.8}$$

where $\mathbf{O} = \mathrm{FT}_{2D}^{-1}[\mathrm{FT}_{2D}[\cdot] \exp(jk_z z_0)]$ is an operator. Similarly, the adjoint system model of (4.8) (backward process) is

$$\mathbf{G} = \mathbf{O}^{\dagger}[\mathbf{S}], \tag{4.9}$$

where $\mathbf{O}^{\dagger} = \mathrm{FT}_{2D}^{-1}[\mathrm{FT}_{2D}[\cdot] \exp(-jk_z z_0)]$. Therefore, by adding the under-sampling mask,

the FT-CS model can be written as

$$\mathbf{Y} = \mathbf{B} \circ \mathbf{S} = \mathbf{B} \circ \mathbf{O}[\mathbf{G}], \tag{4.10}$$

The matrix formulation of the FT-CS model avoids the vectorization process and thus reduces its complexity. Moreover, due to the adoption of the Fourier transform in the forward and backward operators, each iteration of the algorithm runs much faster than that of the D-CS method. It is worth mentioning that the massive space requirement of the $\mathbf{H}$ matrix has also been eliminated here in the FT-CS method.

### 4.3.3 Reconstruction Algorithms

There are many choices in choosing a CS algorithm to solve the underdetermined system in (4.6) and (4.10). Greedy pursuit [5] and $\ell_1$ optimization [6], as introduced in Chapter 2 are the two mainstreams. In comparison, greedy algorithms are generally much faster but require more measurements. Although it is possible to solve the FT-CS model with certain greedy algorithms that only requires matrix vector product, this process needs to transform the 2-D FFT and 2-D IFFT operator into matrix forms, which introduces extra computation complexity and makes the problem more complicated. Here, we adopt the TwIST algorithm [7] for its significantly faster convergence rate than traditional $\ell_1$ algorithms. More importantly, the forward and backward operators can be applied directly without any modification.

One of the key requirements for successful CS reconstruction is the image sparsity or compressibility. In our case of study, target recognition is the first priority. There are many sparsity representations for imaging applications like wavelet transform, curvelet transform, total variation (TV) [8] and discrete cosine transform. Here we choose the TV in the regularization since it can preserve the sharp edges of an image while imposing smoothness on the solution. TV refers to the integral of the absolute gradient of the

signal. The discrete version for a 2-D image $\mathbf{G}$ can be defined as

$$\mathrm{TV}(\mathbf{G}) = \sum_{i,j} \sqrt{|\mathbf{G}_{i+1,j} - \mathbf{G}_{i,j}|^2 + |\mathbf{G}_{i,j+1} - \mathbf{G}_{i,j}|^2}, \tag{4.11}$$

where $i$ and $j$ denote the discrete indices of $\mathbf{G}$. We denote by $\|\mathbf{g}\|_{TV}$ the vector version of $\mathrm{TV}(\mathbf{G})$. Then the corresponding optimization problem for (4.6) and (4.10) with TV regularization can be written as

$$\hat{\mathbf{g}} = \underset{\mathbf{g}}{\operatorname{argmin}} \frac{1}{2} \|\mathbf{AHg} - \mathbf{y}\|_2^2 + \lambda \|\mathbf{g}\|_{TV}, \tag{4.12}$$

and

$$\hat{\mathbf{G}} = \underset{\mathbf{G}}{\operatorname{argmin}} \frac{1}{2} \|\mathbf{B} \circ \mathbf{O}[\mathbf{G}] - \mathbf{Y}\|_2^2 + \lambda \mathrm{TV}(\mathbf{G}), \tag{4.13}$$

respectively. It is important to note that other transforms can also be added to the above equations which can potentially improve the reconstruction performance. An important step of solving (4.12) and (4.13) is the selection of the regularization parameter $\lambda$, which controls the tradeoff between the sparsity of the solution and the closeness of the solution to the image. For example, if $\lambda$ is too small, then the solution is close to the conventional least squares solution, while if $\lambda$ is too large then the bias of the estimation will be very high. According to our simulation results, the optimal value of $\lambda$ is inconsistent across different data sets, and may change slightly for the same data set with different sampling rates. Another key requirement in CS framework is the RIP that measures the quality of the reconstruction [9]. The ultimate goal in a CS system is to adopt a measurement matrix and a basis matrix such that the sensing matrix has the RIP of high order. However, the RIP is often replaced by checking the mutual coherence as computing RIP is computationally intensive.

## 4.4 Numerical Analysis

This section presents the performance analysis and comparison of two CS based methods using full-wave EM solver simulated data.

### 4.4.1 Simulation Configuration

The simulated data can be acquired using either simplified signal model in (4.1) (synthetic data) or full-wave electromagnetic (EM) solver that follows rigorous Maxwell's equations. In many CS-SAR imaging literature, point scatterers are assumed and synthetic data is used for simplicity. However, in practice, the target area might be very complicated and thus full-wave simulation should be adopted to better approximate the real environment. The full-wave simulation setup consists of antennas and complicated targets, all with appropriate mesh sizes. As the whole volume is electrically large compared to the operating wavelength, the EM simulation can be very time consuming. Among many EM solvers, we tested ANSYS HFSS, CST MICROWAVE STUDIO and FEKO while only FEKO can give acceptable simulation time. Considering that a full switched array for simulation would require too much computing power, we use a single antenna as a transceiver to translate in the scanning aperture. Consequently, this means we ignore the mutual coherence among adjacent antennas in our analysis. To further reduce the simulation time, we use a dipole antenna instead of a directional antenna.

The simulation setup is illustrated in Figure 4.2. An $x$-polarized dipole antenna working at 100 GHz is used to scan an area of 60 $mm \times 60$ $mm$. The target plane is parallel to the scanning aperture with a height of 30 $mm$. Two identical targets which both consist of three metallic rectangular cuboids are placed perpendicularly to each other. The background medium is free space. During the simulation, the reflection scattering parameter ($S11$) of the antenna is acquired at each sampling position and is calibrated by subtracting the background $S11$ as described in [10].

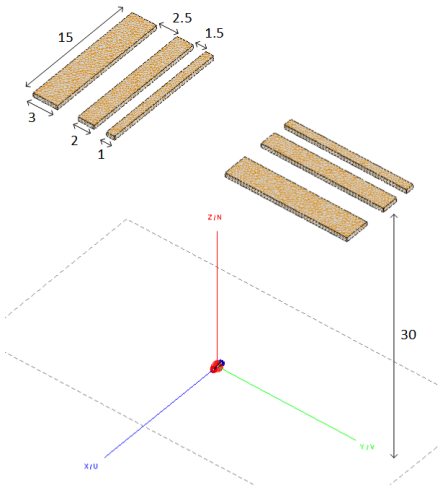


Figure 4.2: Simulation model in FEKO. All dimensions are in mm.

In the following numerical analysis, for the sake of fairness, we ensure that firstly all methods in comparison use the same sampling pattern; secondly, the regularization parameter for both CS methods are adjusted appropriately so that the reconstructed images for all methods are optimized; and thirdly both CS methods share the same stopping criterion, that is the optimizations cease when the relative change in the objective function falls below $1 \times 10^{-4}$ or the number of iterations reached 10000. All the evaluations were implemented using Matlab 2014b (x64) on a Windows 7 operating system, with an Intel i7-4770m processor and 16 GB of memory.

### 4.4.2 Sparsity Constraint

As mentioned previously, the data in our switched array imaging system is complex-valued. Figure 4.3 gives an example of the amplitude, phase, real and imaginary parts of a gun-shaped target recovered by the BP algorithm from experimental data. It is important to note that many sparsifying transforms for real-valued images become invalid or less effective for complex-valued data since only the amplitude of the image can be treated as sparse. Most existing literature has ignored this fact by directly applying the sparsity constraint to the complex-valued signals or only use sparse point-like targets for simplicity. Nevertheless, there has been some attempts to solve this problem. In

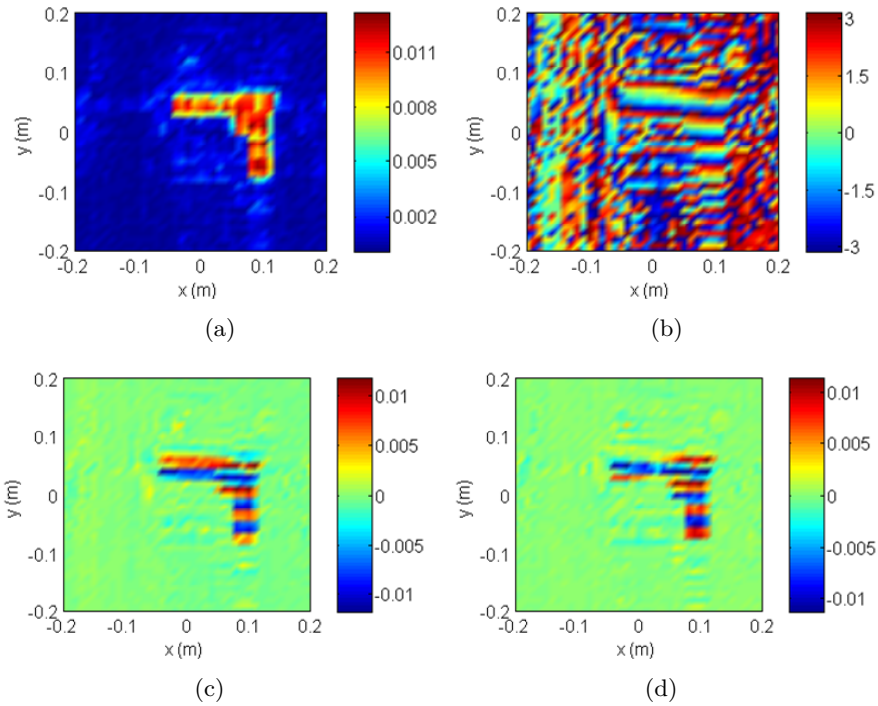


Figure 4.3: The (a) amplitude, (b) phase, (c) real and (d) imaginary parts of the reconstructed signal by the BP method.

[11], the TV regularization is applied to the amplitude only, but the phase is ignored, since in SAR images the phase is usually assumed to be random. On the contrary, the phase information for MRI and terahertz imaging is considered to be smooth and not varying rapidly. In [12], a phase smoothness constraint is introduced by controlling the similarities of the phase intensities among the image pixels. In [13], it was suggested that sparsity can be enforced separately in the real and imaginary parts. Both methods have shown to be effective in dealing with complex-valued images. In the proposed switched array application, the targets are placed in a short range of the array. As can be seen from Figure 4.3, the phase information of the acquired data is actually between random and smooth varying. Therefore, it is worth doing a comparison on these sparsity constraints. Of course, how to find an optimal sparsity constraint shall be an object of further research.

Figure 4.4 compares different sparsity constraints by calculating their mean squared

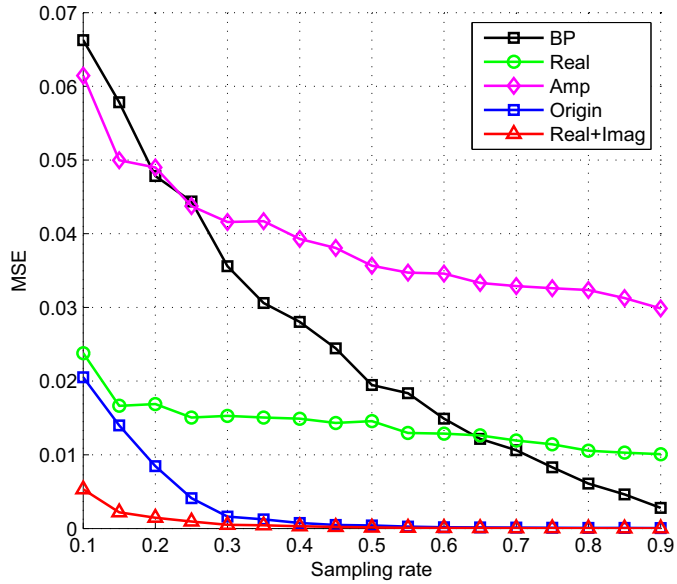


(a)

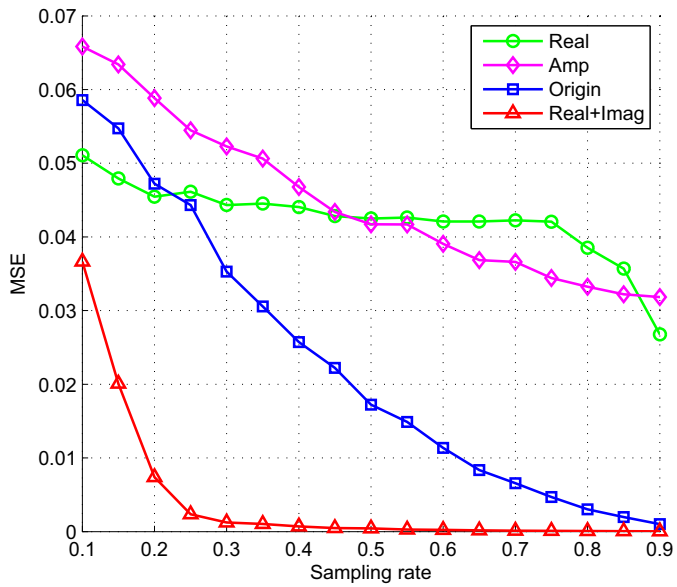


(b)

Figure 4.4: MSE of reconstructed images of different sparsity constraints. (a) FT-CS and (b) D-CS.

errors (MSEs) for the same experiment data as shown in Figure 4.3. The MSEs are averaged over the results of 20 independent trials for each sampling rate. In each trial, the samples are chosen in a random way such that they are independent from that of other trials. The regularizations to the imaginary part only, phase part only and both

amplitude and phase parts do not always converge thus are not shown here. As can be seen from Figure 4.4, TV regularization to the amplitude only scheme (pink curves) actually does not perform well in our case. The separate real and imaginary sparsity scheme (red curves) always achieves lower MSE than regularization applied directly to the original data scheme (blue curves) in both the FT-CS and D-CS methods. Therefore, in the following analysis, we adopt the scheme where sparsity is enforced separately in the real and imaginary parts.

Finally, the optimization model with TV regularization to both real and imaginary parts for (4.12) and (4.13) can be written as

$$\hat{\mathbf{g}} = \underset{\mathbf{g}}{\operatorname{argmin}} \frac{1}{2} \|\mathbf{AHg} - \mathbf{y}\|_2^2 + \lambda(\|\mathbf{g}_{Re}\|_{TV} + i\|\mathbf{g}_{Im}\|_{TV}), \tag{4.14}$$

and

$$\hat{\mathbf{G}} = \underset{\mathbf{G}}{\operatorname{argmin}} \frac{1}{2} \|\mathbf{B} \circ \mathbf{O}[\mathbf{G}] - \mathbf{Y}\|_2^2 + \lambda(\mathrm{TV}(\mathbf{G}_{Re}) + i\mathrm{TV}(\mathbf{G}_{Im})), \tag{4.15}$$

respectively, where $\mathbf{g} = \mathbf{g}_{Re} + i\mathbf{g}_{Im}$ and $\mathbf{G} = \mathbf{G}_{Re} + i\mathbf{G}_{Im}$.

It is very important to point out that objective functions in (4.14) and (4.15) become complex-valued due to the way we formulate the sparsity constraints. It is well-known that the objective function can be used to decide if the iteration is going in the right direction by comparing its current value with the previous value. From the perspective of optimization algorithms, the complex-valued objective function does not make sense because one cannot compare complex numbers. In the algorithm implementation, the complex number comparison is defined by comparing the real parts only. According to our simulation results, this complex-valued sparsity constraint scheme actually outperforms other real number schemes, e.g. $(\mathrm{TV}(\mathbf{G}_{Re}) + \mathrm{TV}(\mathbf{G}_{Im}))$. It is also interesting to note that this scheme achieves better performance than the popular complex-to-real transformation scheme (real parts and imaginary parts are concatenated together for processing) when data is under-sampled. However, this complex number approach is not perfect. In few cases, it can take much longer iteration time than the complex-to-real

transformation scheme. Interested readers can also try to deal with complex-valued data using MMV methods as suggested in Section 3.5.3. Of course, how to find an optimal sparsity constraint shall be an object of further research.

### 4.4.3 Sampling Pattern And Sampling Interval

One of the main differences between switched array imaging and SAR imaging is that the sampling trajectory of the SAR imaging has great flexibility thus its sampling pattern can be completely random. The switched array imaging, on the other hand, can only rely on the fixed feeding points, which makes it less flexible than the SAR system and results in a sampling pattern looks like a binary matrix. Moreover, physical considerations like antenna gain, beamwidth and mutual coupling between antennas make engineering realization of an array that satisfy the Nyquist sampling interval very difficult in MMW frequency range. Generally, a tradeoff is to slightly increase the antenna spacing, for example, $2\lambda/3$ [14] or even higher.

There are two ways to push forward with this increased sampling interval. Firstly, if we use a linear array to perform 1-D mechanical scanning and 1-D electronic scanning, then the Nyquist criterion can be satisfied only in the mechanical scanning dimension. This scheme can be considered when a limited budget is available, as is adopted in [14]. There is also a trade-off between image quality and scan duration on how to choose the sampling rate in each dimension. Normally, under-sampling in the mechanical scanning dimension can save more time since skipping one position means abandoning one line of measurements in the electronic scanning dimension. However, the highly under-sampled data plus randomness reduced sampling pattern will impair the reconstruction. Secondly, if we use a rectangular full array to perform 2-D electronic scanning, Nyquist criterion will be violated in both dimensions. The advantage is the under-sampling can be completely random in both dimensions. Moreover, the already fast electronically scanning time can be further reduced by randomly activating only part of the antennas for data acquisition. For the following discussions, we only consider the second case for simplicity.

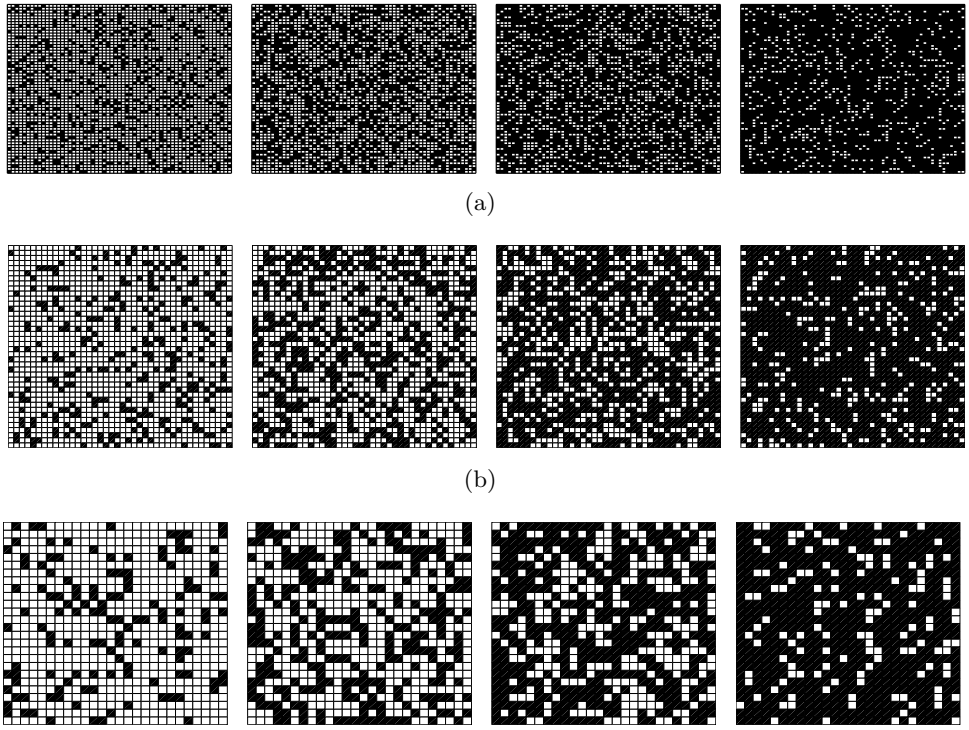

(a)

(b)

(c)

Figure 4.5: Four random under-sampling masks under (a) $\lambda/4$ element spacing, (b) $\lambda/2$ element spacing and (c) $3\lambda/4$ element spacing. From left to right, sampling rates of four masks are 80%, 60%, 40% and 20%, respectively.

#### 4.4.3.1 Qualitative Results

Since the transceiver-to-target distance is 30 $mm$, the Nyquist sampling interval is approximately $0.35\lambda$ according to (4.2). We acquired three sets of data with uniform under-sampling interval (element spacing) of $\lambda/4$, $\lambda/2$ and $3\lambda/4$. The last two intervals are both larger than the Nyquist sampling interval. These uniformly sampled data are then randomly sub-sampled by 80%, 60%, 40% and 20%, as shown in Figure 4.5, to mimic the random under-sampling process. It should be noted that random sampling is realized by first producing a random permutation of the measurements using the randperm function in Matlab and then selecting the first required number of samples. Here, the white pixels represent selected locations to sample. It can be noticed that since all cases have the same scanning aperture, small sampling interval case has denser pix-

els. Based on these sampling masks, conventional BP method and two CS methods are employed for image reconstruction.

As mentioned previously, the grid size of the target plane has a crucial influence on the performance of the D-CS reconstruction. Therefore, we also adopt three different grid spacings of $\lambda/8$, $\lambda/4$ and $\lambda/3$ for comparison. It is important to note that due to the differences in size of reconstructed image and measurement matrix, two CS methods have different optimal regularization parameters. For instance, in the following example, the regularization parameter is around 0.01 for D-CS methods and 0.001 for FT-CS methods.

Figure 4.6 shows the corresponding reconstructed images based on the three sets of under-sampled data. As we can see from the first three columns in Figure 4.6(a) and Figure 4.6(b), different grid sizes lead to different image resolutions in reconstruction. The number of pixels of the three grid sizes are $161 \times 161$, $81 \times 81$ and $61 \times 61$, from left to right, respectively. From Figure 4.6(b), It can be noticed that a finer grid size does not actually give better image reconstruction, especially when the sampling rate is low. This agrees with our analysis in the previous subsection since the $\lambda/2$ element spacing case is already highly under-sampled compared to the Nyquist rate. Reducing the grid size will require more measurements as the number of unknown pixels has also increased. However, this does not mean that a larger grid size is preferable. The grid size should be carefully chosen because too large grid size will lead to very low resolution and grid mismatch [15] may also occur at this case. The optimal grid size should consider both the sampling rate and the array element spacing such that the number of measurements is well above the minimum requirement posed by the CS theory. In comparison, the FT-CS and BP methods cannot freely choose the image size during reconstruction. This is because neither 2-D FT nor 2-D IFT of a matrix changes its size, which makes the reconstructed image the same resolution as the sampled aperture. It should be noted that although some conventional smoothing techniques like zero-padding and interpolation can also be used within the FT-CS method, they do not really increase the spatial

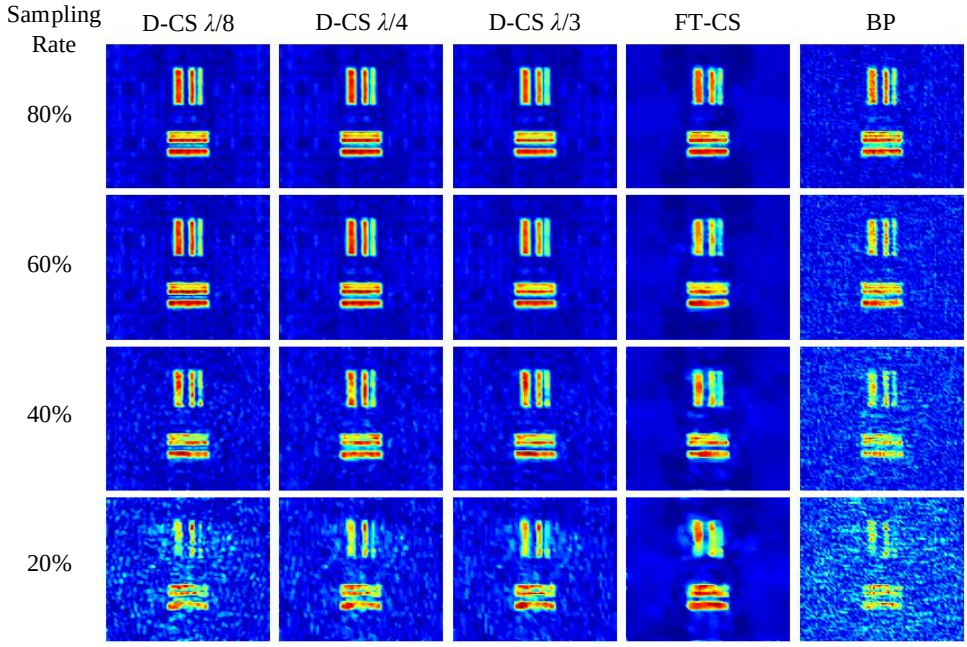


(a)

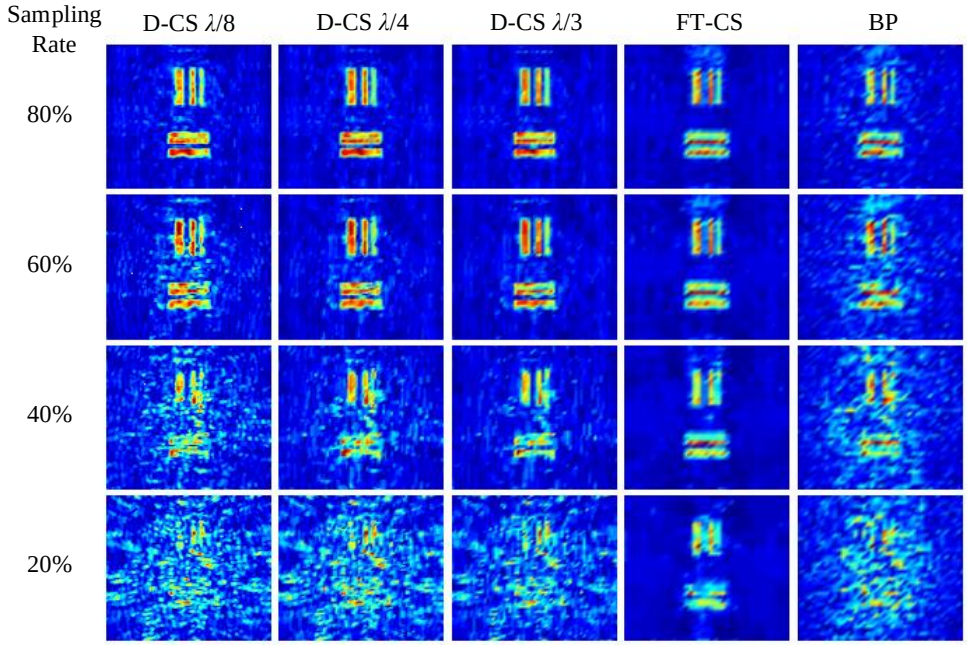


(b)

resolution, thus are not discussed here.

Figure 4.6(c) shows the results based on $3\lambda/4$ element spacing which is about twice the Nyquist sampling interval. Compared with the first two subfigures, the FT-CS and

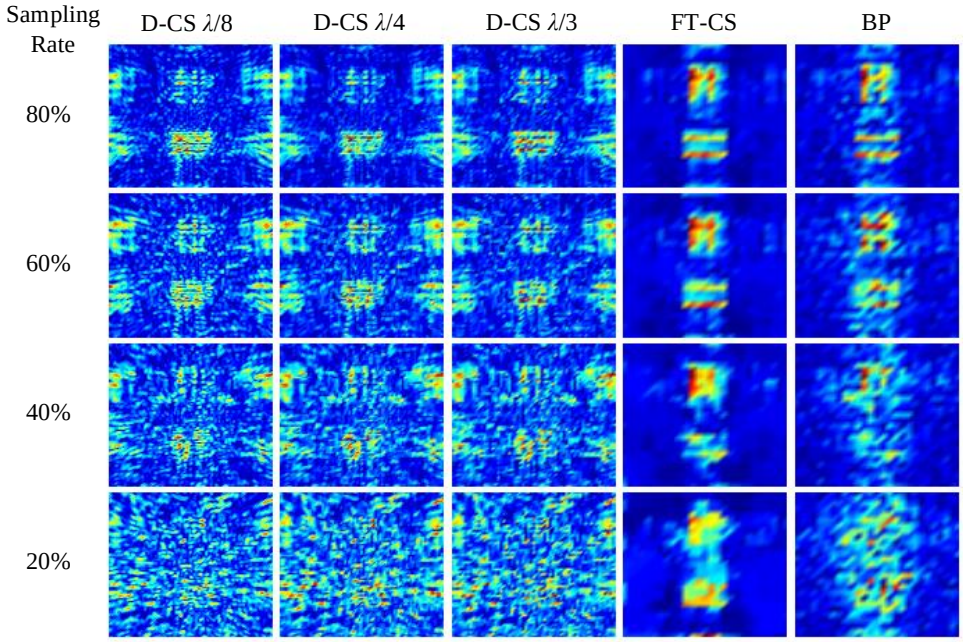


(c)

Figure 4.6: Simulation results showing the reconstruction quality of three methods based on (a) $\lambda/4$ element spacing, (b) $\lambda/2$ element spacing and (c) $3\lambda/4$ element spacing. In each subfigure, from left to right, D-CS methods with grid size of $\lambda/8$, $\lambda/4$ and $\lambda/3$, FT-CS method and BP method.

BP methods have blurrier images. This is because a larger sampling interval results in less pixels in the reconstruction. Interestingly, all D-CS methods with $3\lambda/4$ element spacing fail to reconstruct the image correctly as ghost targets can be observed in all cases. The FT-CS method, on the other hand, can still reconstruct the contour of the targets under very low sampling rate. This interesting result indicates that the FT-CS method is more robust to random under-sampling than the D-CS method.

#### 4.4.3.2 Quantitative Results

While Figure 4.6 only considers reconstructions with certain under-sampling masks, Figure 4.7 quantitatively summarizes the effect of random under-sampling on the MSEs of reconstructed images of different methods. Since the D-CS method fails to reconstruct images with $3\lambda/4$ element spacing, Figure 4.7 only shows the result based on element

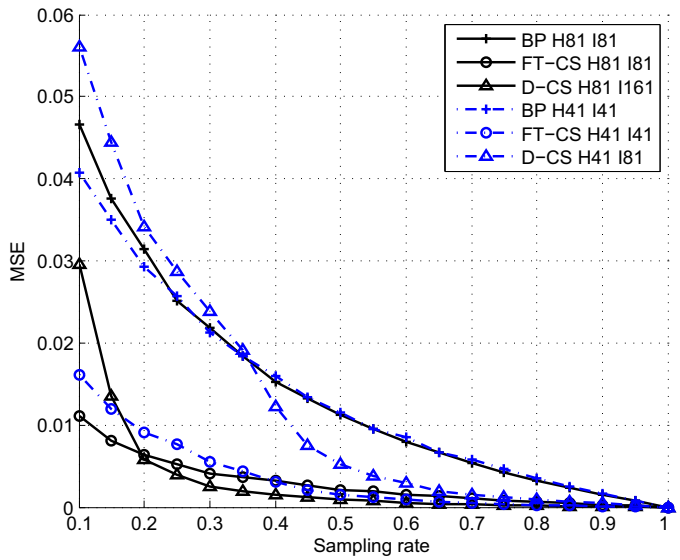


Figure 4.7: MSE trend of three methods with element spacing of $\lambda/2$ and $\lambda/4$.

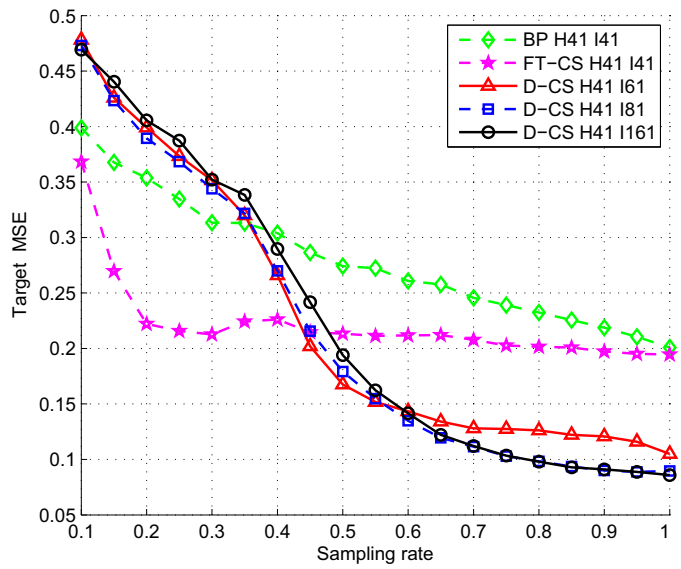


Figure 4.8: MSE of the target area for the BP, FT-CS and three D-CS methods.

spacing of $\lambda/2$ and $\lambda/4$. For the ease of annotation, we use H81 and I161 in the legend to indicate the switched array has $81 \times 81$ elements ($\lambda/4$ sampling interval) and the reconstructed image has $161 \times 161$ pixels ($\lambda/8$ grid spacing). The MSE of each method is calculated with respect to its own full sampling rate result and is averaged over the results of 40 independent trials for each sampling rate. An MSE curve with slow

variation against sampling rate means the corresponding method is robust to random under-sampling. Clearly, FT-CS achieves the best robustness in both element spacing cases which agrees with our qualitative results. More importantly, each method behaves distinctly in two element spacing cases. The MSE of the D-CS method starts to vary intensively when the sampling rate is below 50% in $\lambda/2$ element spacing case but a similar variation only happens under 20% sampling rate in the $\lambda/4$ element spacing case. On the contrary, the BP and FT-CS methods have relatively small differences in the two cases. This indicates the D-CS method is very susceptible to the element spacing or uniform under-sampling interval. Increasing the number of measurements is recommended for stable reconstruction.

However, it is not quite straightforward to compare the image quality among different methods since different regularization parameters of CS algorithm result in distinct levels of estimation error and thus render the total MSE ineffective to represent the true quality of the reconstruction. Therefore, we calculate the MSE of the target area (ignoring the background) with respect to the ground truth. Figure 4.8 compares the target MSE of three methods based on $\lambda/2$ element spacing. The D-CS method achieves the lowest error with high sampling rate beyond 45% while the FT-CS method performs better with low sampling rate. The improvement of the FT-CS method becomes less effective with very high sampling rate, which indicates the FT-CS method is more like a denosing technique based on the BP method. For D-CS methods with different grid sizes, a threshold point can be observed at 60% sampling rate. A smaller grid size achieves lower reconstruction error with the sampling rate higher than this threshold, but suffers from insufficient number of measurements compared to a larger grid size setting when the sampling rate is below this threshold. As the sampling rate goes below 35%, the randomness of D-CS methods start to dominate and the errors become even larger than the BP method.

Table 4-A: Complexity Comparison of D-CS Methods

| Configuration | Computing time (s) | Loading time (s) | Storage |
|---|---|---|---|
| $M = 41$, $N = 81$ | 15.03 | 1.67 | 72 MB |
| $M = 41$, $N = 121$ | 33.61 | 3.84 | 221 MB |
| $M = 81$, $N = 121$ | 140.67 | 17.28 | 1.04 GB |
| $M = 81$, $N = 161$ | 224.36 | 27.12 | 1.37 GB |
| $M = 134$, $N = 134$ | $1.45 \times 10^3$ | 88.65 | 2.94 GB |
| $M = 134$, $N = 178$ | $4.58 \times 10^3$ | 717.72 | 8.23 GB |

### 4.4.4 Computational Complexity

In this subsection, we consider the computational complexities of the aforementioned methods. It should be noted that the code for all three methods are not optimized for speed. Apparently, the BP method is the fastest as CS based methods need multiple iterations until they reach the convergence. Additionally, the FT-CS method is more computationally efficient than the D-CS method due to the adoption of the FFT algorithm. Since both CS methods use the same reconstruction algorithm, we can evaluate their complexity by simply comparing their models. Suppose the full switched array is of size $M \times M$ elements, the number of actually sampled points is K, the discretization of D-CS method is $N \times N$. The D-CS model in (4.6) consists of two matrix multiplication thus has time complexity of order $\mathcal{O}(KM^2N^2 + KN^2)$. If we keep $M$ fixed, then the number of grid points $N$ contributes most to the time complexity while the number of sampled points $K$ has less contribution. For the FT-CS model in (4.10), it includes two 2-D FFT/IFFT operations and two element-wise matrix multiplication. Considering the $\mathcal{O}(M \log M)$ complexity of 1-D FFT and $\mathcal{O}(M^2)$ complexity of element-wise matrix multiplication, the total time complexity is then about $\mathcal{O}(2M^2 + 4M^2 \log M)$ for the FT-CS method. Since the grid size of target plane is usually set to be finer than the sampling interval ($N > M$), the D-CS method will always has much higher time complexity than the FT-CS method.

As the time complexity quantifies the amount of time that one algorithm needs to run, the space complexity is a measure of the amount of working storage an algorithm needs. The space complexity of the D-CS method mainly comes from the system response

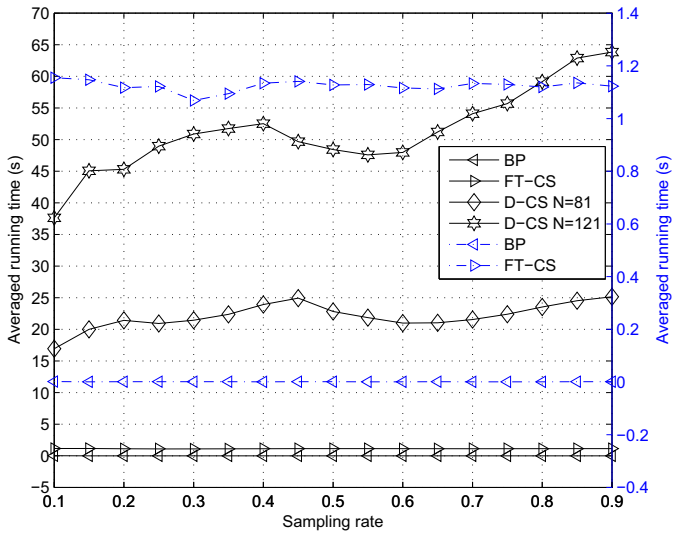


Figure 4.9: Averaged running time of different methods versus random under-sampling.

matrix **H** which contains the distance information from all pixels (voxels for 3-D case) in the target area to all sampling points in the aperture plane. According to (4.4), an $M \times M$ scanning aperture with $N \times N$ grid points will lead to an $M^2 \times N^2$ complex-valued **H**. As the BP and FT-CS methods do not need to compute such response matrix, their space complexities can be neglected. Table 4-A gives the computing time, loading time and required storage of **H** based on different scanning apertures and grid sizes. Note the data processed in Matlab is set as double precision. The constructing time and loading time of the D-CS method is non-negligible since the target distance might be unknown and real-time calculation of **H** is inevitable. While it is quite normal for any practical security imaging system to deal with sampling aperture as large as 1 $m \times 1$ $m$, the D-CS method will be incredibly slow in such cases.

To verify the above analysis, we evaluate the overall algorithm running time of each method against the sampling rate as shown in Figure 4.9. The test data has $81 \times 81$ array elements with $81 \times 81$ and $121 \times 121$ grid sizes adopted for the D-CS method. The running times are averaged over the results of 10 independent trials for each sampling rate. The dark colored curves show the superiority of FT based methods over D-CS methods. For example, the D-CS method with $N = 121$ has a running time nearly 50 times of the

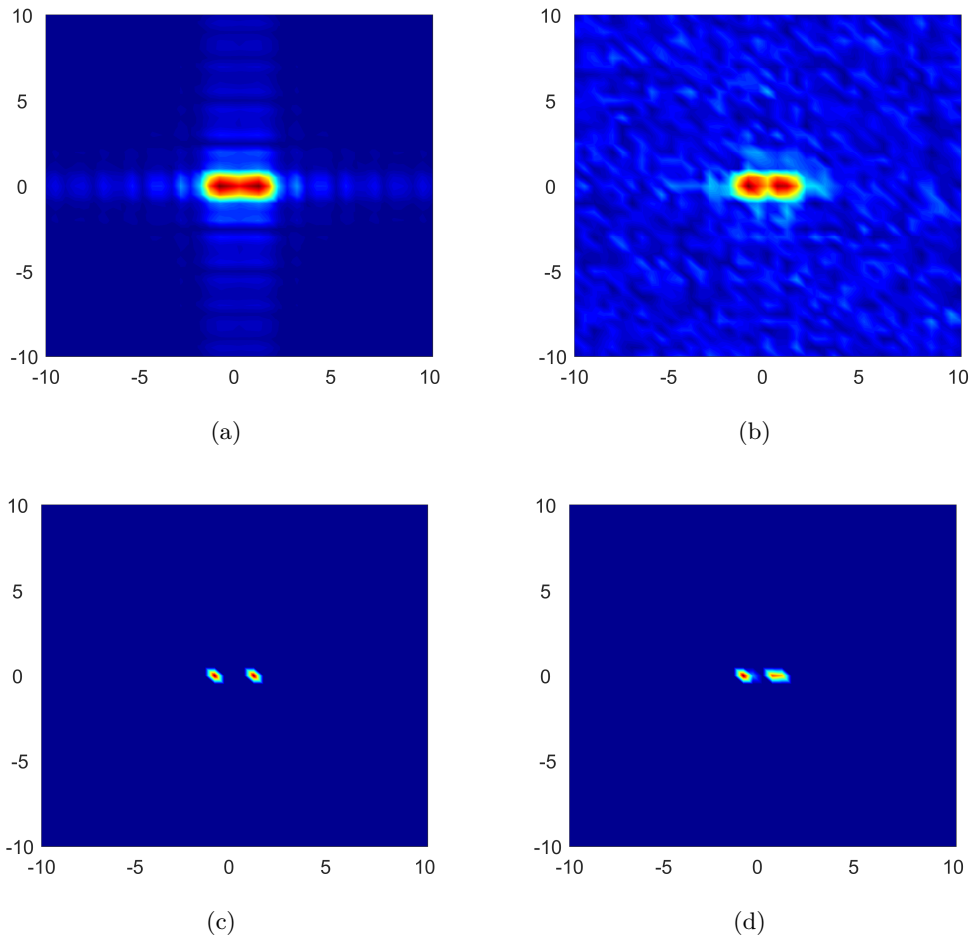


Figure 4.10: Reconstruction results of two point scatterers at $(\pm 0.9, 0)$ by (a) BP with 100% data, (b) BP with 50% data, (c) FT-CS with 100% data and (d) FT-CS with 50% data.

FT-CS method when the sampling rate is 50%. Further, the blue dashed curves give a better illustration of the FT-CS method and the BP method with a smaller scale. Both methods have little variation in running time as sampling rate increases. However, for D-CS methods, the variation becomes more obvious when $N$ gets bigger. This is expected as the number of grid points contributes more to the time complexity.

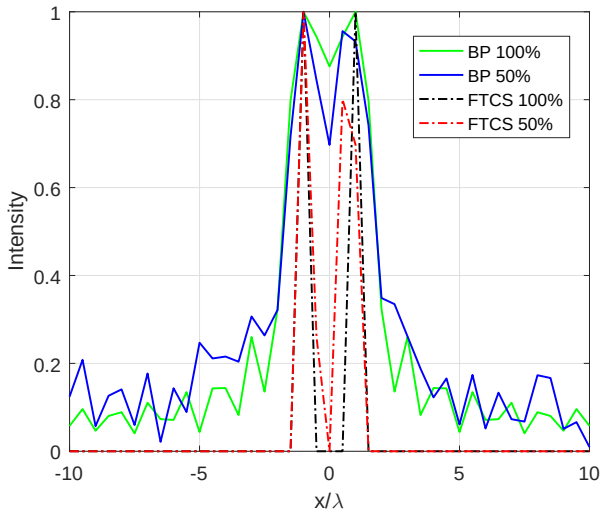


Figure 4.11: One-dimensional cut of BP and FT-CS methods for point scatterers at $(\pm 0.9, 0)$.

### 4.4.5 Resolution

One of the most important properties of an imaging system is probably its resolving power. However, most of the existing literature overlooked the effect of CS methods on the resolving power of the imaging system. The question arises whether CS methods can break the resolution limit and what are the factors determine the resolution. In this subsection, we study the spatial resolution of CS based methods and try to answer these questions. Therefore, we set up several synthetic point targets for resolution test. As the target scene is already sparse in the spatial domain, we adopt the $\ell_1$ norm instead of the TV norm.

Without loss of generality, the unit of the dimension is set as one wavelength. The simulation parameters are set as follows: scanning aperture $L_x = L_y = 20$, transceiver to target distance $z_0 = 50$ and antenna element spacing is kept at 0.5. We first consider two point scatterers located at $(\pm 0.9, 0)$. Figs. 4.10(a) gives an example of image reconstruction by the conventional BP method with full sampled data. Due to the resolution limitation, the two point scatterers in the reconstruction can not be distinguished from each other. Sidelobes of the two scatterers are also clearly visible. Then, Figure 4.10(b)

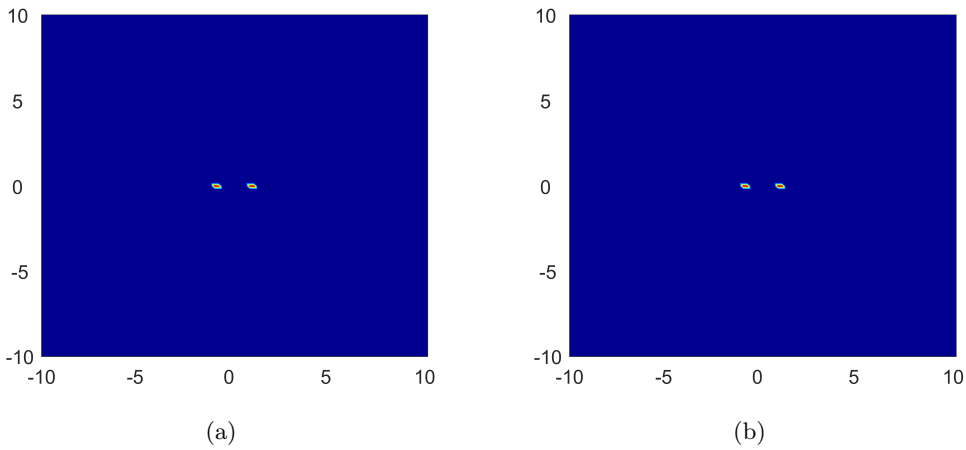


Figure 4.12: Reconstruction results of two point scatterers at $(\pm 0.9, 0)$ by (a) D-CS with 50% data and (b) D-CS with 10% data.

shows the results with only 50% random data. We can notice slightly distortion in the center area and the background is filled with noise-like speckles. When the BP method is combined with CS technique, as shown in Figure 4.10(c) and Figure 4.10(d), two point scatterers can be clearly observed in the center, with perfectly clean background. However, the under-sampled one shows weakened reflectivity on the right scatterer and its position is slightly shifted to the left. To better understand this, we plot the one-dimensional cut of Figure 4.10 at $y = 0$. From Figure 4.11, we can easily notice that methods with full data correctly reconstruct the two scatterers while the under-sampled methods failed to reconstruct the right scatterer at $(0.9, 0)$. If we focus on the two under-sampled methods, we can find the red dashed curve (FT-CS method) is actually a shrank version of the blue solid curve (BP method), but with lower dip between the two peaks. It seems that the FT-CS method inherited the displacement error from the under-sampled BP method. This is comprehensible considering that each iteration of the FT-CS method is based on the FT and IFT operations. From the very begining, the sparsity constraint is actually enforced to the under-sampled BP reconstruction. This result indicates that the performance of the FT-CS method is highly dependant on the BP reconstruction, which also means the FT-CS method might not be able correct the distortion if it comes from the BP reconstruction.

Recall that the difference between D-CS methods and FT-CS methods lies in the choice of the forward operator. D-CS methods simply discretize the accurate forward process into a matrix form and avoids the inaccurate FT operations. In this case, we expect the D-CS method to achieve better reconstruction than the FT-CS method. Here, we set the grid spacing of the (region of interest) ROI is as 0.2, which is smaller than the 0.5 sampling interval. Figure 4.12(a) and Figure 4.12(b) demonstrate the D-CS reconstruction with 50% data and 10% data, respectively. No visible difference can be observed from the two figures, which suggests the D-CS method does not suffer from the same issue like the FT-CS method does. Moerover, as the grid spacing of the D-CS method is much smaller than the FT-CS method, the reconstructed two scatterers are more focused in the center, showing definitely better resolving power.

So far, we have learned that both CS methods are capable of increasing the resolving power of the imaging system. However, when sufficient measurements are guaranteed, the D-CS method is more reliable than the FT-CS method in faithfully reconstructing the target scene. To better understand the resolving power of the D-CS method, we consider if the size of the ROI can affect the resolving power. Therefore we simulate a half-wavelength spaced array with the aperture size $L_x = L_y = 6$ and the target plane at $z_0 = 50$. The resolution is around 2 for traditional methods. Two point scatterers with 1 spacing are tested for three different sizes of ROI denoted by $L_{ROI} = 20$, 12 and 4, respectively. It is important to note that the optimal regularization parameter can be affected by random under-sampling, size of the aperture, element spacing, target sparsity, size of the ROI, grid spacing and so on. Here, we set two examples that focus on the ROI, with one keeps all ROIs have the same number of pixels in the target scene while the other keeps all grid spacings the same.

In the first example, the number of pixels for all cases are fixed at $81 \times 81$. The corresponding grid spacings are 0.25, 0.15 and 0.05, respectively. The regularization parameter for each case is optimized to achieve best reconstruction. Figure 4.13 shows the reconstruction comparison when full sampled data is used. All three schemes can

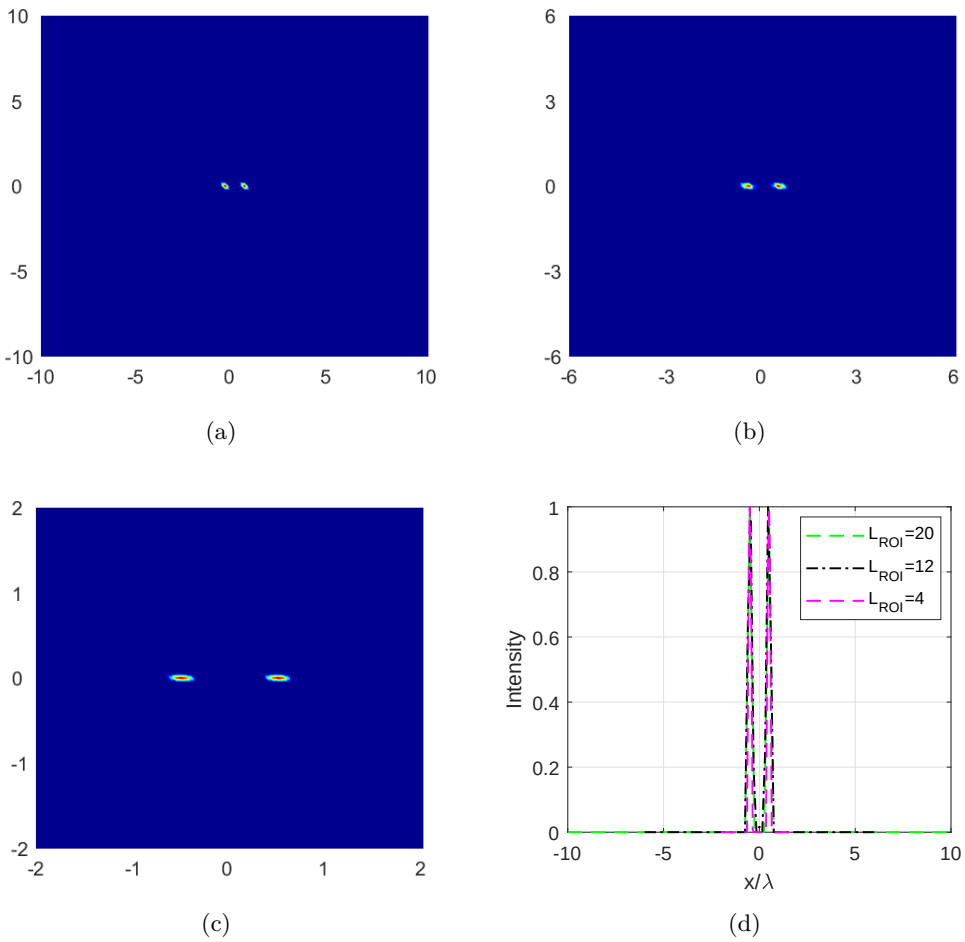


Figure 4.13: Reconstruction results of two point scatterers at $(\pm 0.5, 0)$ with (a) $L_{ROI} = 20$, (b) $L_{ROI} = 12$ and (c) $L_{ROI} = 4$. (d) One-dimensional reconstruction at $y = 0$.

resolve the two point scatterers and the 1-D cut comparison shows similar resolving power. However, according to our test, when the data is randomly undersampled and the regularization parameters are fixed (same as in the full sampling), the larger the ROI is, the more likely the reconstruction will fail to resolve the targets. It is interesting to point out that by increasing the aperture size or the scatterers' spacing, the need for frequently calibration of the regularization parameters can be alleviated. This result indicates that to achieve very fine resolution, the regularization parameters should be carefully calibrated and smaller ROI require less tuning of the parameters.

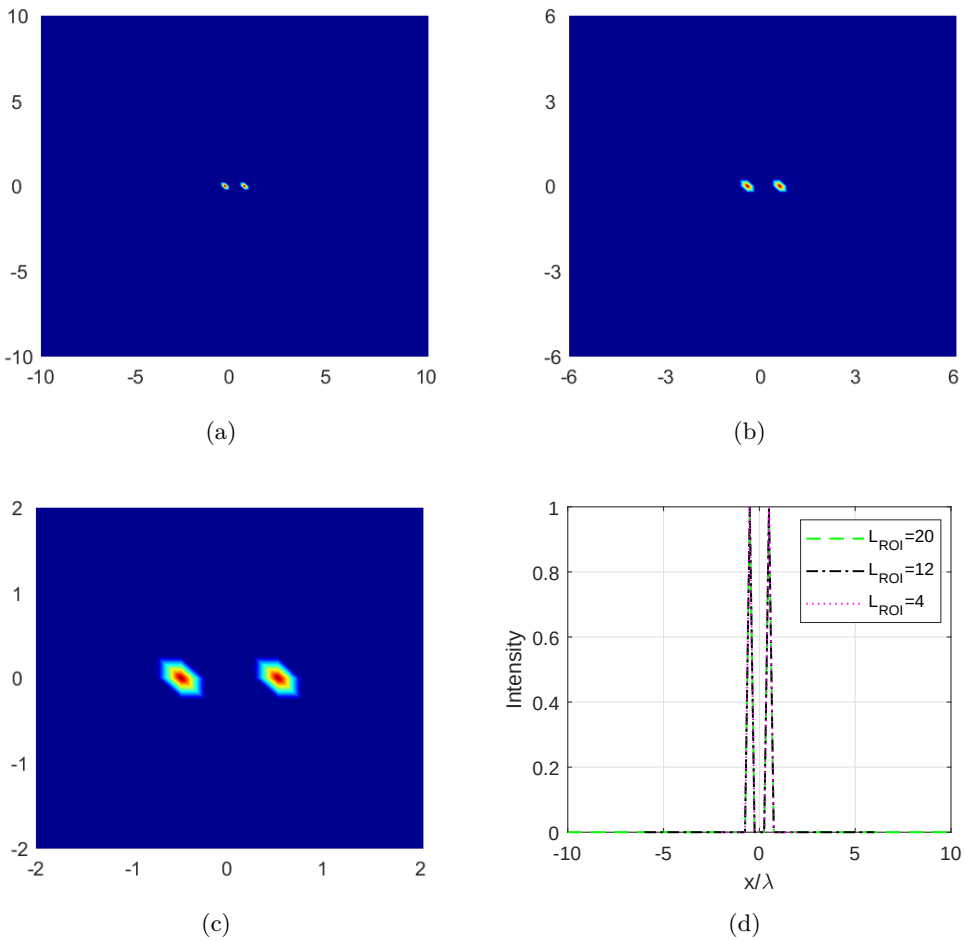


Figure 4.14: Reconstruction results of two point scatterers at $(\pm 0.5, 0)$ with (a) $L_{ROI} = 20$, (b) $L_{ROI} = 12$ and (c) $L_{ROI} = 4$. (d) One-dimensional reconstruction at $y = 0$.

In the second example, the grid spacings are fixed 0.25. The corresponding discretizations for each case are $81 \times 81$, $49 \times 49$ and $17 \times 17$, respectively. Figure 4.14 shows the reconstruction comparison when full sampled data is used. Similarly, all three schemes can resolve the two point scatterers. However, in comparison to the first example, the curves as shown in Figure 4.14(d) overlapped on each other. This interesting difference is because in the first example, due to the same number of pixels but different sizes of ROI, the grid and the targets are not perfectly aligned. Then by using random undersampling and keep the regularization parameters fixed, we observe similar phenomenon like the first example.

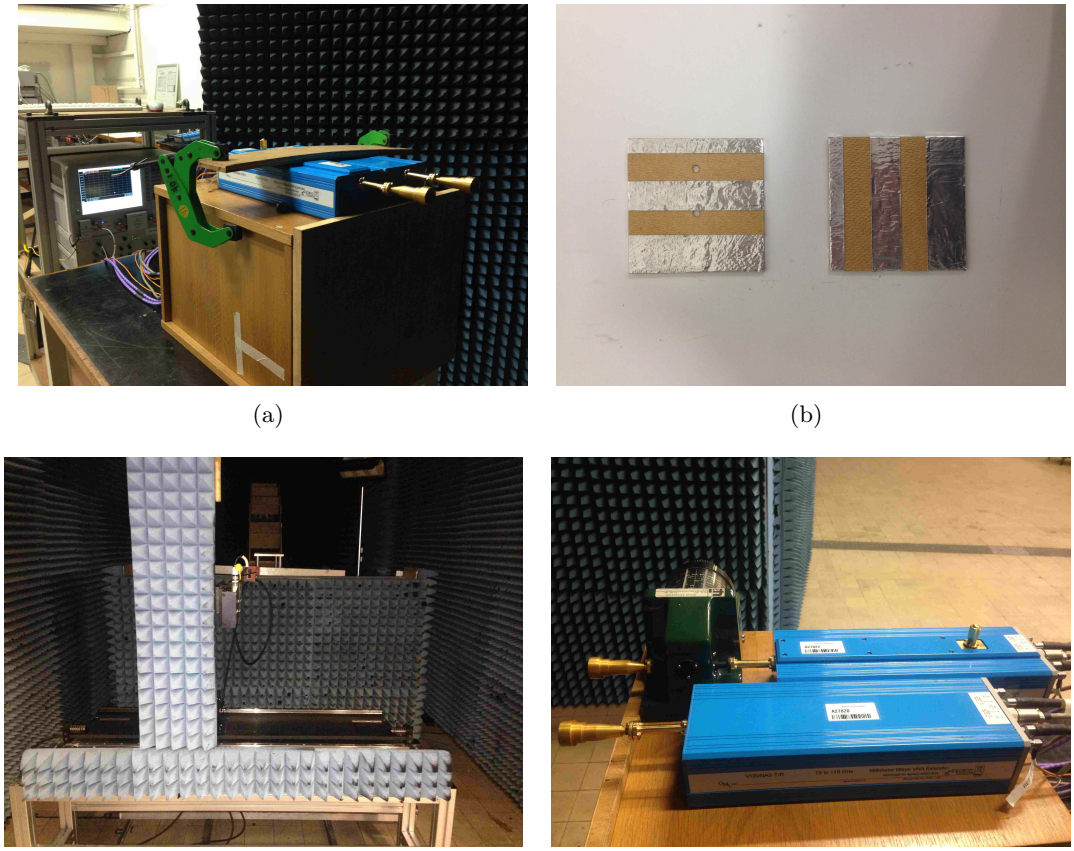

(a) (b)

(c) (d)

Figure 4.15: System setup: (a) measuring equipments, (b) two identical targets with metallic stripes, (c) NSI scanner and (d) measuring equipments with an attenuator.

From the above two examples, we cannot say the size of the ROI will make much difference to the resolution but we can conclude that it is easier to calibrate the regularization parameters with a smaller ROI. It should also be noted that as the scanning aperture is a square, the resolution in both $x$ and $y$ dimensions should be identical in theory. Therefore, the aforementioned conclusions in this subsection also apply to the case where points scatterers are aligned parallel to the $y$ axis. However, these figures are not shown here such that this chapter can be more concise.

## 4.5 Experimental Results

To make the simulation results more solid, we conducted several experiments in the antenna lab of Queen Mary University of London (QMUL) which located in the basement of the Engineering building. In Figure 4.15(a), two corrugated conical horn antennas with frequency multipliers are connected to a vector network analyzer (VNA) to work as transmitter and receiver, respectively. The VNA is an Agilent N5244A PNA-X with a maximum frequency of 43.5 GHz. The original signals are then extended to 100 GHz by the 75-110 GHz frequency multiplier. Both horn antennas have a flare angle of 15°.

Our targets are two wooden plates wrapped with metallic stripes as shown in Figure 4.15(b), with a distance of 1.6 $m$ to the transmitter plane. As it is not easy to do raster scan with the bulky frequency multipliers, the measuring equipments are kept still while the target is mounted on an NSI xyz scanner as shown in Figure 4.15(c). The scanning region is confined in an area of 400 $mm \times 400$ $mm$. According to (4.2), the required Nyquist sampling interval is approximately $1.9\lambda$. Here, we adopt $2.25\lambda$, $3\lambda$ and $3.75\lambda$ sampling interval (element spacing) for comparison. The grid spacing of the target plane is fixed at $\lambda$. Figure 4.16 shows results of the D-CS, FT-CS and BP methods under different sampling rates. Similar to the simulation results, the D-CS method can achieve better resolution than the FT-CS method but has serious ghost image problem in the reconstruction under approximately twice the Nyquist sampling interval. The FT-CS method is more robust to highly random under-sampling which can be very useful when fast scanning is needed. Both two CS methods perform better than the BP method with reasonable sampling intervals.

To investigate the robustness of CS methods over different transmitting power, we manually reduce the power by connecting an attenuator between the transmitting antenna and the frequency multiplier, as shown in Figure 4.15(d). The original 5-10 dBm transmitting power is attenuated by 25 dB, 35 dB, 45 dB and 50 dB. Two random under-sampling masks of 100% sampling rate and 60% sampling rate are tested with data under

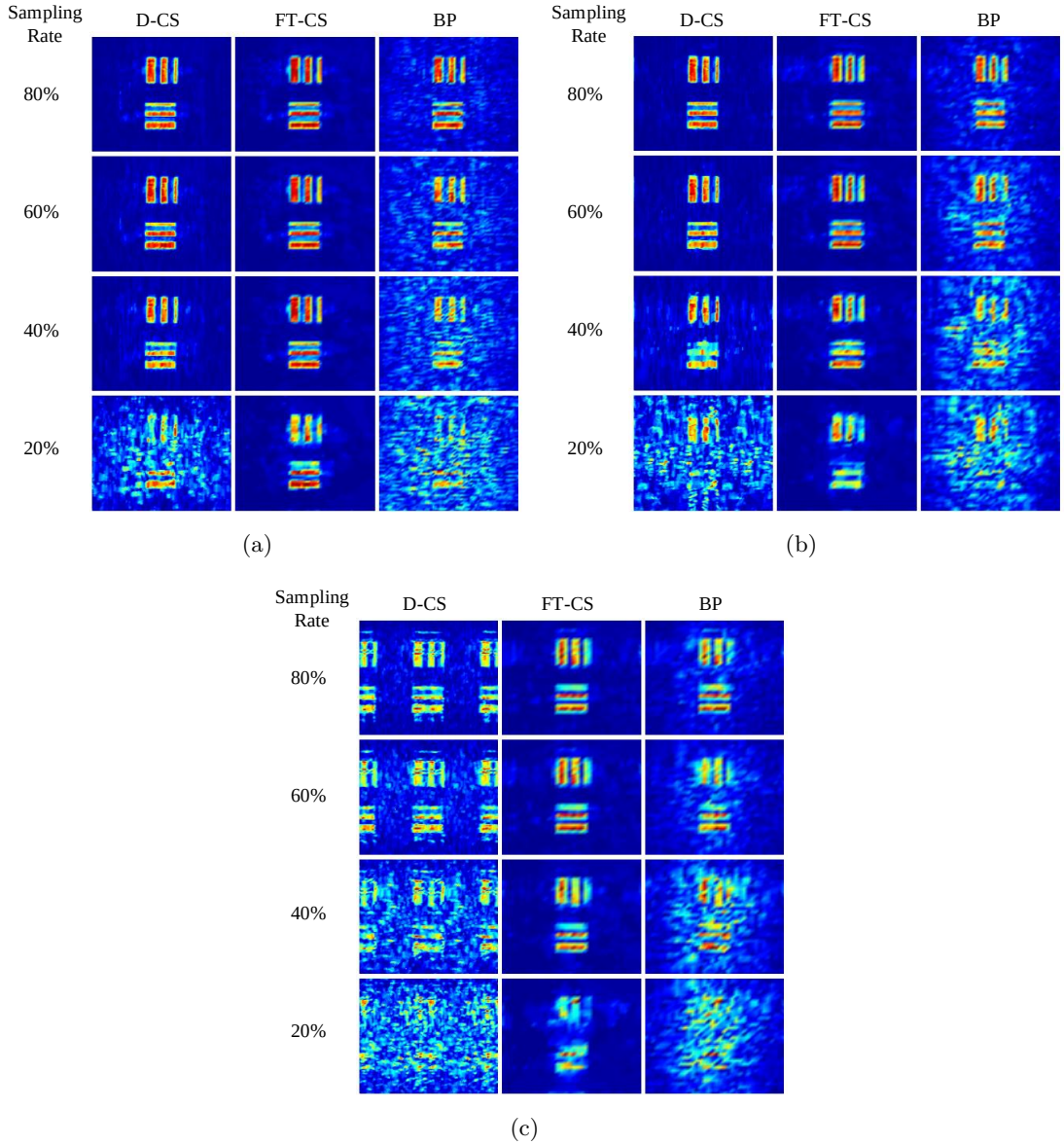


Figure 4.16: Experimental results showing the reconstruction quality of three methods based on element spacing of (a) $2.25\lambda$, (b) $3\lambda$ and (c) $3.75\lambda$.

$2\lambda$ uniform sampling interval. From Figure 4.17, we can see the number of speckles begin to increase as the attenuation increases. CS based methods show a good noise reduction over the BP method. Particularly, the FT-CS method is the most robust to the imaging system with low transmitting power. The comparison between Figure 4.17(a) and Figure 4.17(b) indicates more measurements can help produce a better image under low

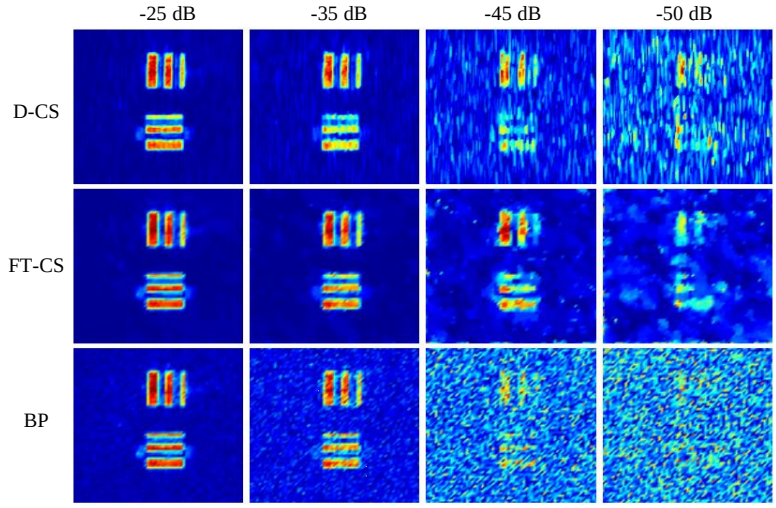


(a)

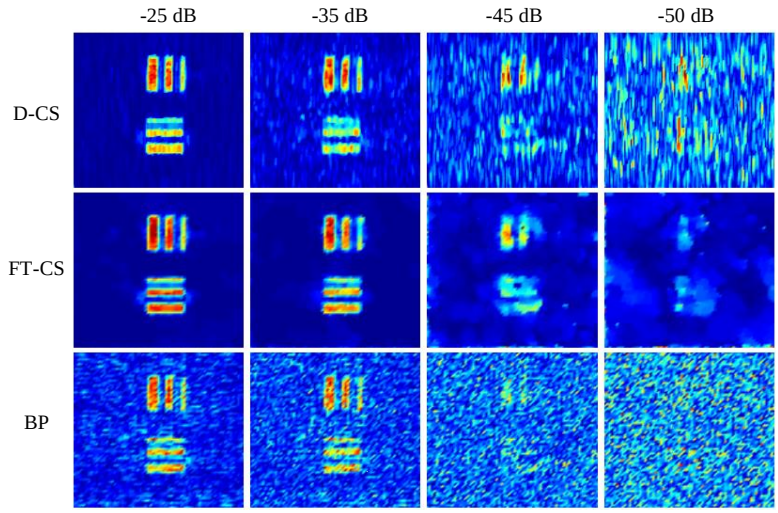


(b)

Figure 4.17: Experimental results showing the effect of transmitting power of three methods with different sampling rates. (a) 100% sampling rate (full sampling). (b) 60% sampling rate.

transmitting power.

## 4.6 Summary

In this chapter, compressive switched array imaging techniques have been thoroughly studied. The D-CS method was compared with the FT-CS method and the conventional

BP method. For the optimal reconstruction of CS methods, sparsity constraint and regularization parameter should be carefully calibrated with respect to different under-sampling rates and targets. When the data is randomly under-sampled to save scanning time, CS based methods outperforms the BP method with better image reconstruction and higher resolving power. Particularly, for practical antenna array imaging systems where element spacing does not satisfy the Nyquist criterion, D-CS methods achieve better resolution than other methods at the cost of much higher computational complexity. However, it should be noted that D-CS methods start to show ghost targets in reconstruction when the element spacing is too large. On the other hand, the FT-CS method are more stable than D-CS methods in the case of large element spacing, low number of measurements and low transmit power.

In regards to the objective mentioned in the beginning of this chapter, we can finally conclude that, for a practical switched array imaging system, the FT-CS and D-CS methods are complementary techniques that can be used together for optimized efficiency and image reconstruction. More specifically, the FT-CS method can be used to significantly reduce number of samples for a fast but coarse view of the scene. The D-CS method can be later used for higher resolution in the ROI if necessary.

## References

[1] J. Case, M. Ghasr, and R. Zoughi, "Optimum two-dimensional uniform spatial sampling for microwave sar-based nde imaging systems," *IEEE Transactions on Instrumentation and Measurement*, vol. 60, no. 12, pp. 3806–3815, Dec 2011.

[2] Y. Rivenson and A. Stern, "Compressed imaging with a separable sensing operator," *IEEE Signal Processing Letters*, vol. 16, no. 6, pp. 449–452, June 2009.

[3] S. Li, G. Zhao, H. Li, B. Ren, W. Hu, Y. Liu, W. Yu, and H. Sun, "Near-field radar imaging via compressive sensing," *IEEE Transactions on Antennas and Propagation*, vol. 63, no. 2, pp. 828–833, Feb 2015.

[4] D. L. Donoho and M. Elad, "Optimally sparse representation in general (nonorthogonal) dictionaries via $\ell_1$ minimization," *Proceedings of the National Academy of Sciences*, vol. 100, no. 5, pp. 2197–2202, 2003.

[5] J. Tropp and A. Gilbert, "Signal recovery from random measurements via orthogonal matching pursuit," *IEEE Transactions on Information Theory*, vol. 53, no. 12, pp. 4655–4666, Dec 2007.

[6] E. Candes, J. Romberg, and T. Tao, "Robust uncertainty principles: exact signal reconstruction from highly incomplete frequency information," *IEEE Transactions on Information Theory*, vol. 52, no. 2, pp. 489–509, Feb 2006.

[7] J. M. Bioucas-Dias and M. A. Figueiredo, "A new twist: two-step iterative shrinkage/thresholding algorithms for image restoration," *IEEE Transactions on Image Processing*, vol. 16, no. 12, pp. 2992–3004, 2007.

[8] L. I. Rudin, S. Osher, and E. Fatemi, "Nonlinear total variation based noise removal algorithms," *Physica D: Nonlinear Phenomena*, vol. 60, no. 1, pp. 259–268, 1992.

[9] E. J. Candès, "The restricted isometry property and its implications for compressed sensing," *Comptes Rendus Mathematique*, vol. 346, no. 910, pp. 589 – 592, 2008.

[10] R. K. Amineh, M. Ravan, A. Trehan, and N. K. Nikolova, "Near-field microwave imaging based on aperture raster scanning with tem horn antennas," *IEEE Transactions on Antennas and Propagation*, vol. 59, no. 3, pp. 928–940, 2011.

[11] M. Cetin and W. Karl, "Feature-enhanced synthetic aperture radar image formation based on nonquadratic regularization," *IEEE Transactions on Image Processing*, vol. 10, no. 4, pp. 623–631, Apr 2001.

[12] Z. Xu and E. Y. Lam, "Image reconstruction using spectroscopic and hyperspectral information for compressive terahertz imaging," *J. Opt. Soc. Am. A*, vol. 27, no. 7, pp. 1638–1646, Jul 2010.

[13] J. Trzasko and A. Manduca, "Highly undersampled magnetic resonance image reconstruction via homotopic $\ell_0$-minimization," *IEEE Transactions on Medical Imaging*, vol. 28, no. 1, pp. 106–121, Jan 2009.

[14] D. Sheen, D. McMakin, and T. Hall, "Three-dimensional millimeter-wave imaging for concealed weapon detection," *IEEE Transactions on Microwave Theory and Techniques*, vol. 49, no. 9, pp. 1581–1592, Sep 2001.

[15] Y. Chi, L. Scharf, A. Pezeshki, and A. Calderbank, "Sensitivity to basis mismatch in compressed sensing," *IEEE Transactions on Signal Processing*, vol. 59, no. 5, pp. 2182–2195, May 2011.

# Chapter 5

# Compressive Sensing for Phased Array Imaging

## 5.1 Introduction

Signal-to-noise ratio (SNR) is a critical parameter in radar system which essentially describes the difference between the desired signal and the unwanted noise. If the amplitude of the noise approaches that of the transmitted or received signal, loss of accuracy will be observed in reconstruction due to distortion of the reflected signal as it does not reveal the true target information. While it is intuitive to increase the transmitted power to assure the noise does not become dominant, there are also other ways to alleviate the noise issue, e.g., use high-gain antennas or low-noise amplifiers. Reflector antenna is one of the high-gain antennas that has been successfully introduced to security imaging [1–3]. A common reflector antenna system consists of a feeding antenna or a feeding array and a reflecting surface, commonly in parabolic shape. The feeding antenna is directed towards the reflector such that its relatively wide beam can be collimated to generate a narrow beam in the direction of reflection. Reflector antennas provide a relatively low-cost and straightforward solution for achieving high antenna gain. Their downside

is that beam-steering can only be achieved by the use of mechanical rotator, which is usually slow in scanning.

On the other hand, phased array antennas provide electronic flexibility in exciting the elements, allowing for reconfiguration and scanning of the beam pattern in real time. The gain of a phased array antenna is increased in a way that its main beam is focused in one particular direction while the sidelobes are suppressed in undesired directions. By electronically steering the main beam towards desired target region, the imaging system greatly maximizes its SNR [4] and hence we expect the image reconstruction will be more robust to background noise.

This chapter presents the CS method for phased array imaging. A general 3-D array imaging model has been derived in Section 5.2. Section 5.3 presents the compressive phased array imaging method together with numerical analysis. In Section 5.4, a near-field focusing technique is integrated into the compressive phased array imaging method to offer better imaging quality for near-field applications. The conclusions are given in Section 5.5.

## 5.2 Phased Array Forward Imaging Model

The 3-D imaging model shown in Figure 5.1 is interpreted in the dimension of range and cross-range. The range ($z$) is the direction of wave propagation and the cross-range ($x$ or $y$) is the direction parallel to the array aperture. A 2-D planar array is located in the $x$-$y$ plane with its center in the origin. All elements are evenly spaced in both $x$ and $y$ dimensions. The amplitude and phase of the elements across the array are adjusted so that the main beam of the radiation pattern is directed towards a specified direction. By continuously illuminating the target region with directional beams of different elevation angle $\theta$ and azimuth angle $\phi$, where $\theta \in [0, \pi/2]$ and $\phi \in [0, 2\pi)$, the reflectivity information of the target region can be reconstructed from the reflected data.

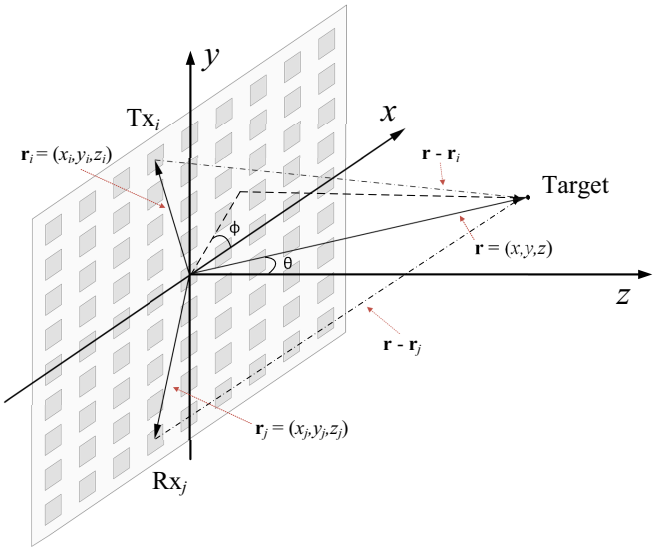


Figure 5.1: Three-dimensional imaging using 2-D phased array and wideband signals. By assigning appropriate weights to each element, the main beam of the array is focused in the direction of $(\theta, \phi)$ while the sidelobes are suppressed in the undesired directions.

Assuming an observing point $\mathbf{r} = (x, y, z)$ is at the far field of an antenna element, the electric field radiated from the $i$-th antenna at $\mathbf{r}_i = (x_i, y_i, z_i)$ can be written as [5]

$$\mathbf{E}_i(\mathbf{r}, k) = P_i(\mathbf{r}) \frac{\exp(-jk|\mathbf{r} - \mathbf{r}_i|)}{|\mathbf{r} - \mathbf{r}_i|}, \tag{5.1}$$

where $P_i(\mathbf{r})$ is the element pattern, $k = 2\pi f/c$ is the wavenumber at frequency $f$ and $|\mathbf{r} - \mathbf{r}_i| = \sqrt{(x - x_i)^2 + (y - y_i)^2 + (z - z_i)^2}$ is the distance between $\mathbf{r}$ and $\mathbf{r}_i$. In general, it is assumed that all element patterns are the same. Assuming the mutual coupling effects among elements can be neglected, the total transmitted electric field can be calculated by the superposition of all elements

$$\mathbf{E}_\mathbf{T}(\mathbf{r}, k) = P(\mathbf{r}) \sum_i W_i \frac{\exp(-jk|\mathbf{r} - \mathbf{r}_i|)}{|\mathbf{r} - \mathbf{r}_i|}. \tag{5.2}$$

The coefficient $W_i = |W_i| \exp(-j\Psi_i)$ is the complex weight with amplitude $|W_i|$ and phase $\Psi_i$ added to the $i$th element. In order to steer the antenna beam in a certain

direction, e.g., $(\theta, \phi)$, the phase term has to be in the form of [5]

$$\Psi_i = k\hat{\mathbf{r}}_0 \cdot \mathbf{r}_i, \tag{5.3}$$

where $\hat{\mathbf{r}}_0 = \hat{\mathbf{x}} \sin\theta \cos\phi + \hat{\mathbf{y}} \sin\theta \sin\phi + \hat{\mathbf{z}} \cos\theta$ is the unit vector in the direction of $(\theta, \phi)$. By substituting (5.3) into (5.2) and neglecting the amplitude term, we get the total field when beam is steered towards $(\theta, \phi)$

$$\mathbf{E_T}(\mathbf{r}, k, \theta, \phi) = P(\mathbf{r}) \sum_i \frac{\exp[-jk(\hat{\mathbf{r}}_0 \cdot \mathbf{r}_i + |\mathbf{r} - \mathbf{r}_i|)]}{|\mathbf{r} - \mathbf{r}_i|}. \tag{5.4}$$

According to the reciprocity theorem, the transmit and receive properties of an antenna are identical. Therefore, each element in the phased array shares the same pattern and phase delay in both transmitting and receiving modes. Assuming there is a point scatterer at the observing point $\mathbf{r} = (x, y, z)$ with frequency independent reflectivity $g(\mathbf{r})$. The reflected electric field received by the $j$-th antenna at $\mathbf{r}_j = (x_j, y_j, z_j)$ can be denoted as

$$\mathbf{E}_j(\mathbf{r}, k, \theta, \phi) = P(\mathbf{r}) g(\mathbf{r}) \mathbf{E_T}(\mathbf{r}, k, \theta, \phi) \frac{\exp[-jk(\hat{\mathbf{r}}_0 \cdot \mathbf{r}_j + |\mathbf{r} - \mathbf{r}_j|)]}{|\mathbf{r} - \mathbf{r}_j|}. \tag{5.5}$$

Similarly, by summing the electric field of all receiving elements and combining (5.4), the total received field of the phased array due to a point scatterer at $\mathbf{r}$ can be written as

$$\mathbf{E_R}(\mathbf{r}, k, \theta, \phi) = P(\mathbf{r})^2 g(\mathbf{r}) \sum_i \sum_j \frac{\exp[-jk(\hat{\mathbf{r}}_0 \cdot \mathbf{r}_i + |\mathbf{r} - \mathbf{r}_i| + \hat{\mathbf{r}}_0 \cdot \mathbf{r}_j + |\mathbf{r} - \mathbf{r}_j|)]}{|\mathbf{r} - \mathbf{r}_i||\mathbf{r} - \mathbf{r}_j|}. \tag{5.6}$$

Under the assumption of the BA, i.e., neglecting any mutual interaction between the targets, the total reflected field from all scatterers can be expressed as

$$s(k, \theta, \phi) = \iiint_V \mathbf{E_R}(\mathbf{r}, k, \theta, \phi)\, dx\, dy\, dz, \tag{5.7}$$

where $V$ represents the 3-D volume of the target region.

It is worth noting that although we assume using transceiver module based array, the above forward model is also applicable to other phased array configurations, e.g., digital beamforming receiver array case can just ignore the transmitter beamforming in (5.2). Moreover, by assigning random complex weight $W_i$ to each antenna, the forward model can be used for arrays with arbitrary radiation patterns. Since the far field assumption in (5.1) is based on a single antenna and the near field region of an array is usually much farther than it is of a single antenna, the forward model is still effective in the near field region.

The term $P(\mathbf{r})$ in (5.6), which is also called the element factor, plays an important role in the beamforming performance. In the case of using isotropic antenna which has the same intensity of radiation in all directions, the $P(\mathbf{r})$ term can be dropped in the above equations. By doing so and rewriting the vectors as in the Cartesian coordinates, (5.6) becomes identical to those in [6] (2-D in range and cross-range) and [7] (2-D in cross-range). Without loss of generality, we also adopt this isotropic antenna assumption in the following discussions.

The forward model in (5.7) describes how electromagnetic waves interact with targets. Our goal is to reconstruct the reflectivity function $g(\mathbf{r})$ from the received data. To avoid missing vital information, the angles $\phi$ and $\theta$ should be chosen to cover the complete target region. The sampling intervals in both angle and frequency domains should follow the Nyquist theorem to avoid aliasing. In conventional FT inversion techniques [6, 7], the term $\exp(-jk|\mathbf{r}-\mathbf{r}_i|)/|\mathbf{r}-\mathbf{r}_i|$ and $\exp(-jk|\mathbf{r}-\mathbf{r}_j|)/|\mathbf{r}-\mathbf{r}_j|$ are first decomposed into integrals over wavenumber domain and then processed with inverse FT algorithms. As the inverse FT requires uniformly spaced data in $(k_x, k_y, k_z)$ domain, the received data which is uniformly spaced in $(k, \theta, \phi)$ domain needs to be interpolated according to dispersion relations. There are drawbacks in this process though. Firstly, by utilizing the Fourier decomposition, the FT method is actually trying to solve an approximated model of (5.7). In other words, the FT solution is only an approximation to the true

reflectivity. Secondly, the accuracy of interpolation from $(k, \theta, \phi)$ domain to $(k_x, k_y, k_z)$ domain is highly dependent on the choice of interpolation techniques. Owing to the approximation nature of interpolation, the inaccuracy of this process cannot be avoided. In the next section, we will show the proposed CS method can overcome both issues.

## 5.3 Compressive Sensing Implementation to Phased Array

### 5.3.1 CS Forward Imaging Model

We first rewrite the vectors in (5.7) into coordinates form. Suppose $N_{tx} \times N_{ty}$ is the number of antennas in the transmitting aperture and $N_{rx} \times N_{ry}$ is the number of antennas in the receiving aperture. As the array is 2-D, we denote by $(a(i), b(j))$ the $x$-$y$ coordinates of the $(i, j)$-th element in the transmitting array and $(u(i), v(j))$ the $x$-$y$ coordinates of the $(i, j)$-th element in the receiving array. Thus, (5.7) can be rewritten as

$$\begin{aligned} s(k,\theta,\phi) = \iiint_V \sum_{m_1=1}^{N_{tx}} \sum_{m_2=1}^{N_{ty}} \sum_{n_1=1}^{N_{rx}} \sum_{n_2=1}^{N_{ry}} & g(x,y,z) C(a(m_1), b(m_2), x, y, z, k) \\ & \times C(u(n_1), v(n_2), x, y, z, k) \exp[-j(\Psi(a(m_1), b(m_2), k, \theta, \phi) \\ & + \Psi(u(m_1), v(m_2), k, \theta, \phi))]\, dx\, dy\, dz, \end{aligned} \tag{5.8}$$

where

$$C(x_0, y_0, x, y, z, k) = \frac{\exp(-jk\sqrt{(x-x_0)^2 + (y-y_0)^2 + (z-0)^2})}{\sqrt{(x-x_0)^2 + (y-y_0)^2 + (z-0)^2}} \tag{5.9}$$

and

$$\Psi(x_0, y_0, k, \theta, \phi) = k(x_0 \sin\theta \cos\phi + y_0 \sin\theta \sin\phi). \tag{5.10}$$

In order to apply CS algorithms, the target region needs to be discretized and (5.8) should be reformulated into the following matrix multiplication form

$$\mathbf{s} = \mathbf{H}\mathbf{g}, \tag{5.11}$$

where $\mathbf{s}$ and $\mathbf{g}$ are the vector versions of $s(k, \theta, \phi)$ and $g(x, y, z)$, respectively. $\mathbf{H}$ is the system response matrix and can be treated as the sensing matrix with full sampling rate from the perspective of CS theory. More specifically, suppose the 3-D target region $V$ can be discretized into $P \times Q \times R$ voxels and we denote by $I$, $J$ and $K$ the number of frequency points, azimuth angles and elevation angles used during data acquisition. Then (5.11) can be rewritten as

$$\begin{bmatrix} \mathbf{s}(1) \\ \vdots \\ \mathbf{s}(IJK) \end{bmatrix} = \begin{bmatrix} \mathbf{H}_{1,1} & \dots & \mathbf{H}_{1,PQR} \\ \vdots & \ddots & \vdots \\ \mathbf{H}_{IJK,1} & \cdots & \mathbf{H}_{IJK,PQR} \end{bmatrix} \begin{bmatrix} \mathbf{g}(1) \\ \vdots \\ \mathbf{g}(PQR) \end{bmatrix}, \tag{5.12}$$

where element $\mathbf{H}_{i,j}$ is determined by the summation in (5.8) with certain $k$, $\theta$, $\phi$ and voxel coordinates. Specifically, the $i$-th column of $\mathbf{H}$ is related to the coordinates of the $i$-th voxel in $\mathbf{g}$. Each row of $\mathbf{H}$ is related to specific values of $k$, $\theta$ and $\phi$. These parameters are of vital importance in determining the quality of CS reconstruction, which will be discussed in the next section.

### 5.3.2 Reconstruction Algorithms

In conventional FT methods, the sampling intervals have to satisfy the Nyquist theorem to avoid aliasing. With CS theory, we are able to break this restriction by randomly undersampling in the $\theta$, $\phi$ and $k$ domains. Mathematically, this is realized by randomly selecting a set of rows in $\mathbf{H}$. Let $\mathbf{y}$ be the undersampled data and $\mathbf{A}$ the row selection matrix, the final CS model can be written as

$$\mathbf{y} = \mathbf{AHg}. \tag{5.13}$$

As (5.13) is an underdetermined system, it has infinite solutions. CS theory offers an alternative way to solve this by enforcing a sparsity constraint on the solution:

$$\min_{\mathbf{g}} \|\mathbf{g}\|_0 \quad s.t. \;\; \mathbf{y} = \mathbf{AHg}, \tag{5.14}$$

where $\|\mathbf{g}\|_0$ is the number of nonzeros of vector $\mathbf{g}$. Unfortunately, (5.14) is computationally difficult to solve. A more general approach is to relax the $\ell_0$ norm to $\ell_1$ norm:

$$\min_{\mathbf{g}} \|\mathbf{g}\|_1 \quad s.t. \;\; \mathbf{y} = \mathbf{AHg}, \tag{5.15}$$

where $\|\mathbf{g}\|_1 = \sum_i |\mathbf{g}_i|$ is the $\ell_1$ norm of vector $\mathbf{g}$. This minimization problem is the known Basis Pursuit (BP) we introduced in Chapter 3. Considering the imaging system is always accompanied with noise, we use the more realistic Basis Pursuit Denoising (BPDN) [8] to solve (5.15):

$$\min_{\mathbf{g}} \|\mathbf{g}\|_1 \quad s.t. \;\; \|\mathbf{AHg} - \mathbf{y}\|_2^2 \leq \epsilon, \tag{5.16}$$

where $\epsilon$ is a nonnegative real parameter that defines the noise level. There are many algorithms available to solve the above $\ell_1$ minimization. We adopt the same TwIST algorithm which used in Chapter 4. The final Lagrangian relaxed minimization problem can be expressed as:

$$\hat{\mathbf{g}} = \underset{\mathbf{g}}{\operatorname{argmin}} \frac{1}{2} \|\mathbf{AHg} - \mathbf{y}\|_2^2 + \lambda \|\mathbf{g}\|_1, \tag{5.17}$$

where $\lambda$ is the regularization parameter which controls the tradeoff between the sparsity of the solution and its closeness to the least squares solution.

The key requirement to ensure the solution to both (5.14) and (5.15) will coincide is the sensing matrix $\mathbf{\Phi} = \mathbf{AH}$ has to satisfy the RIP [9]. It has been proven that certain matrices satisfy the RIP with high probability, e.g., random Gaussian and Bernoulli matrices. However, in our case, the sensing matrix does not follow a certain statistical characteristics, which makes it very challenging to prove its RIP conditions. Fortunately,

the mutual coherence [10] is an alternative measure of the system ability to accurately reconstruct a signal. This metric was empirically shown to be proportional to MSE values for reconstructions [11]. Generally, a sensing configuration that has lower mutual coherence in $\mathbf{\Phi}$ gives lower MSE in reconstruction. Although simple in formulation, this mutual coherence metric is sometimes too conservative for imaging applications. This is due to the fact that there might be some similar columns in $\mathbf{\Phi}$, which can unfairly dominate the mutual coherence. To address this issue, researchers have proposed average mutual coherence [12], $t$-average mutual coherence [13] and $t_{\%}$-average mutual coherence [14]. The $t_{\%}$-average mutual coherence is defined as:

$$\mu_{t_{\%}}(\mathbf{\Phi}) = \frac{\sum_{i \neq j} g_{ij}\sigma_{ij}}{\sum_{i \neq j} \sigma_{ij}}, \quad \sigma_{ij} = \begin{cases} 1, & g_{ij} \in \mathcal{E}_{t_{\%}} \\ 0, & \text{otherwise}, \end{cases} \tag{5.18}$$

where $\mathcal{E}_{\%}$ is the set of $t_{\%}$ percent of the largest column cross-correlations $g_{ij}$. This metric mitigates the outlier issue and hence is better suited as an indication of the reconstruction performance.

As has been shown in Chapter 4, both TV and $\ell_1$ norms can be adopted depending on the target type. When the target region is dominated by few point scatterers, e.g., some SAR imaging applications, the $\ell_1$ norm as shown in (5.26) is already enough to exploit the image sparsity. On the other hand, when the target region is much more complicated or the image scene is no longer sparse in the spatial domain, e.g., security imaging for concealed weapon detection, sparsity transformations like TV [15] are usually added to promote the image sparsity.

### 5.3.3 Numerical Investigations and Analysis

To examine the effectiveness of the proposed method, we first demonstrate image reconstruction in 3-D space. The imaging capabilities are then thoroughly studied for 2-D imaging with both qualitative and quantitative results.

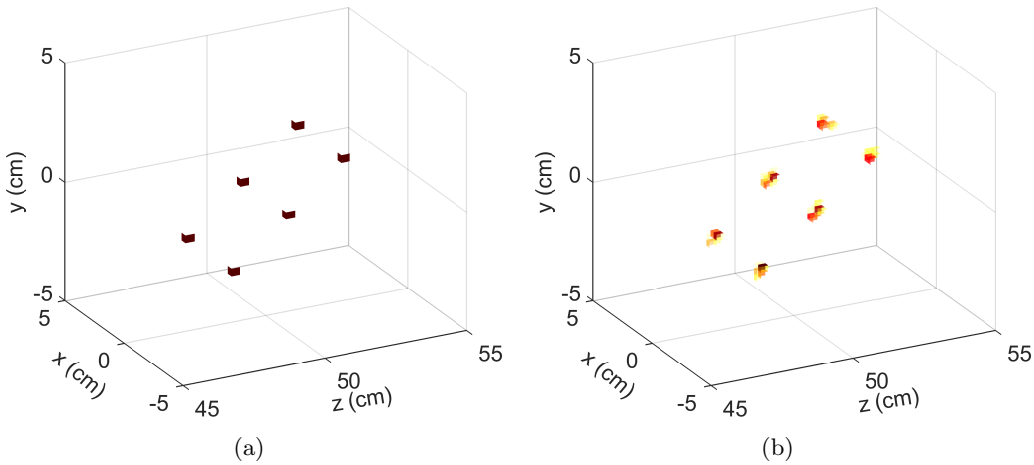


Figure 5.2: Three-dimensional reconstruction of 6 point scatterers. (a) Ground truth of the target scene. (b) Reconstruction by the proposed method.

#### 5.3.3.1 Imaging of 3-D Scene

The simulation is carried out in the MMW frequency band centered at 60 GHz. We assume 20 GHz bandwidth for high range resolution. The length of the array is 6 cm in both $x$ and $y$ dimensions with element spacing fixed at the half of the wavelength of the highest frequency, that is, 2.1 mm. It is worth noting that half-wavelength spacing may violate the Nyquist sampling requirement, but it is chosen so for two reasons. Firstly, element spacing smaller than half-wavelength can be challenging in engineering realization. Secondly, mutual coupling of antenna elements becomes a big issue with closely spaced elements. The resulting array geometry consists of 29 elements in each dimension and 841 elements in total. Elevation angle and azimuth angle are varied within the interval of $[0°, 8°]$ and $[0, 360°)$, respectively, to cover the target region. During data acquisition, 20 frequency points, 15 azimuth angles and 15 elevation angles, all evenly spaced, are deployed to illuminate the target area.

The 3-D target scene, shown in Figure 5.2(a), is 45 cm away from the aperture with dimension of 10 cm×10 cm×10 cm. We consider 6 point scatterers in the target region, each with unit reflectivity. The coordinates of the 6 targets are $(\pm 2, -2, 48)$, $(\pm 2, 0, 50)$

and $(\pm 2, 2, 52)$. Equation (5.8) is adopted to calculate the reflected fields in simulation. In CS implementation, for the ease of computation, we discretize the target scene into $41\times41\times41$ voxels. It should be noted that the selected sampling intervals in frequency and spatial domain already violate the Nyquist criteria according to [6]. Figure 5.2(b) gives the reconstruction result of using only 10% random samples of the undersampled $20\times15\times15$ measurements. As clearly shown, all 6 targets have been correctly reconstructed by the proposed method.

#### 5.3.3.2 Imaging of 2-D Scene

Compared to the 2-D imaging, the 3-D case is computationally more expensive and requires higher memory usage. The construction of the $\mathbf{H}$ matrix can be extremely time-consuming when fine grid spacing is adopted. For these reasons, we concentrate our analysis on the 2-D imaging in cross-range ($x$) and range ($z$) dimensions, in a similar fashion to the 2-D SAR imaging. Because the missing $y$-dimension is the same as the $x$-dimension, the results in the 2-D case can be easily scaled to the 3-D case with suitable computational powers.

In the 2-D case, the azimuth angle $\phi$ is fixed at 0° or 180°, hence equation (5.10) can be simplified to $\Psi(x_0, k, \theta, \phi) = kx_0 \sin\theta \cos\phi$. We assume a linear array of length 8 cm (40 elements) is centered at the origin along the $x$ axis. One hundred equally spaced elevation angles are scanned from 0° to 24°. The bandwidth is still 20 GHz but 40 frequency points are used in this case. The reconstructed area is extended to 30 cm in both range and cross-range dimensions. A finer discretization of $121\times121$ pixels is adopted. We consider $9\times9$ equally spaced point scatterers with an interval of 2.5 cm. Figure 5.3(a) and Figure 5.3(b) represent the reconstruction results of the FT method [6, 16] with 40% data and 100% data, respectively. Both figures are very blurry and the reconstructed targets are barely identifiable. Moreover, just like the case in the switched array imaging, Figure 5.3(a) exhibits more noise in the background due to undersampling. In contrast, as shown in Figure 5.3(c), the CS method accurately

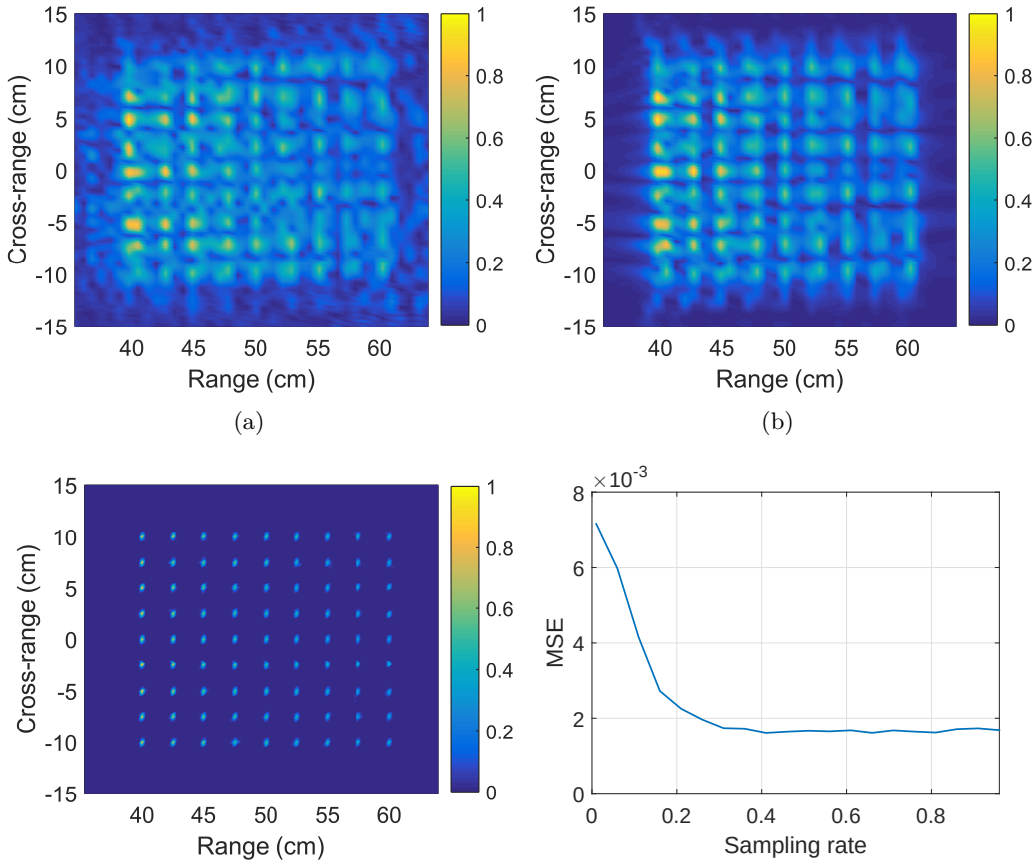


Figure 5.3: Reconstruction results of point scatterers by (a) FT method with 40% data, (b) FT method with 100% data and (c) CS method with 40% data. (d) Averaged MSE of the CS method as a function of sampling rate.

reconstructed all targets and is free from background noise.

Given a sensing configuration, the minimum required number of measurements for accurate reconstruction is determined by the sparsity of the target scene. Generally, the sparser the target scene is, the fewer measurements are required. Figure 5.3(d) quantitatively summarizes the reconstruction quality of the proposed method as a function of undersampling rate. Note the MSE is averaged over the results of 50 independent trials for each sampling rate. It can be observed that the curve gradually becomes flat as the sampling rate reaches 30%, which indicates the minimum required number of measurements for this case is around 30% of the full measurements. Increasing the number of

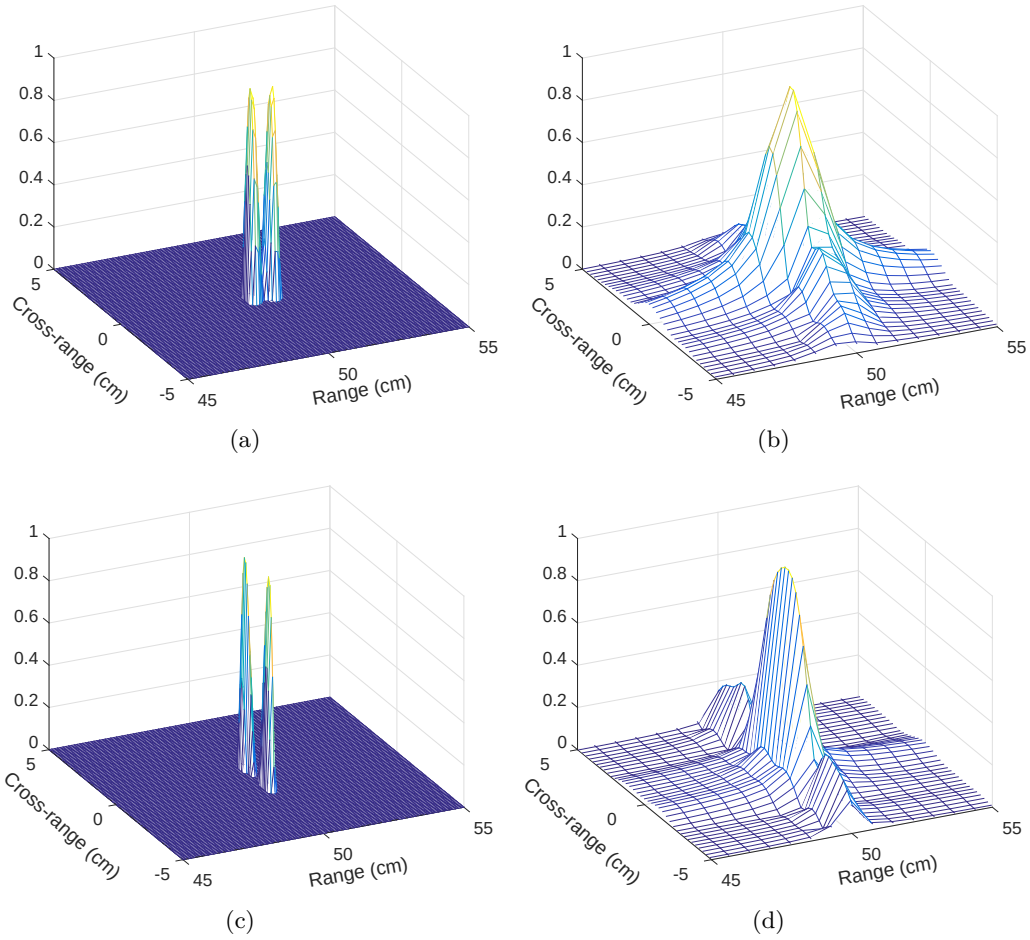


Figure 5.4: Two-dimensional reconstruction of double-point scatterers at $(0, 0, 50 \pm 0.175)$ and $(0, \pm 1, 0)$. (a and c) CS method with 10% data. (b and d) FT method with 100% data.

measurements after the 30% threshold is a waste of time as no obvious improvement can be observed. In most practical situations, the target scene can be much more complicated. Therefore, it is of great importance to obtain empirically the minimum required number of measurements such that the data acquisition time can be maximally reduced.

The resolution of FT methods is determined by the data coverage in the wavenumber domain [6]. It is of interest to establish whether the CS method has the same limitation. Therefore, we employ several sets of closely spaced double-point scatterers for test. The CS reconstruction based on 10% data is compared to full data reconstruction of the FT

method. Reconstructed reflectivity is normalized to $[0, 1]$ for the ease of comparison. In the first example, two scatterers with a spacing of 0.35 cm are centered along the range direction. The two targets can be clearly identified in Figure 5.4(a) while only one single peak is shown in Figure 5.4(b). In a similar manner, the second example compares the reconstructions of 2 cm apart point scatterers in the cross-range direction, as shown in Figure 5.4(c) and Figure 5.4(d). The CS method again makes the two targets discernible. To better analyze the resolving power of the proposed method, we define the resolution of an imaging system as the distance between two targets when the intersection of the two peaks is at the half power level. Figure 5.5(a) and Figure 5.5(b) demonstrate the one-dimensional reconstruction intensity of two sets of double-point scatterers located at $(0, 0, 50 \pm 0.17)$ and $(0, 0, 50 \pm 0.65)$, respectively. It can be observed the FT method has a range resolution of 1.3 cm whereas the CS method has improved the resolution to 0.34 cm. Similarly, Figure 5.5(c) and Figure 5.5(d) show the cross-range direction case where double-point scatterers are located at $(0, \pm 0.4, 0)$ and $(0, \pm 2.3, 0)$. The CS method again has improved the resolution from 4.6 cm to 0.8 cm. Therefore, it can be concluded that the CS method is able to outperform the resolution limit of the FT method in both the range and cross-range directions.

One of the most important advantages of the phased array is the sharpened main beam with suppressed sidelobes. The resulting high gain pattern greatly maximizes the SNR of the imaging systems. To verify this, the imaging results are compared to the results using the switched array scheme in various noise conditions. To do so, we manually add independent and identically distributed (i.i.d.) Gaussian noise to each of the receiving antennas before reconstruction. The noise is with mean zero and variance

$$\sigma_n^2 = \sigma_g^2/(10^{\mathrm{SNR}/10}), \tag{5.19}$$

where $\sigma_g^2 = (1/N)\sum_{i=1}^{N} |g_i|^2$ is the average signal energy. The two imaging systems share the same array configuration and target scene, i.e., same number of antennas in the same aperture. The main difference is the data acquisition process, that is, the phased array

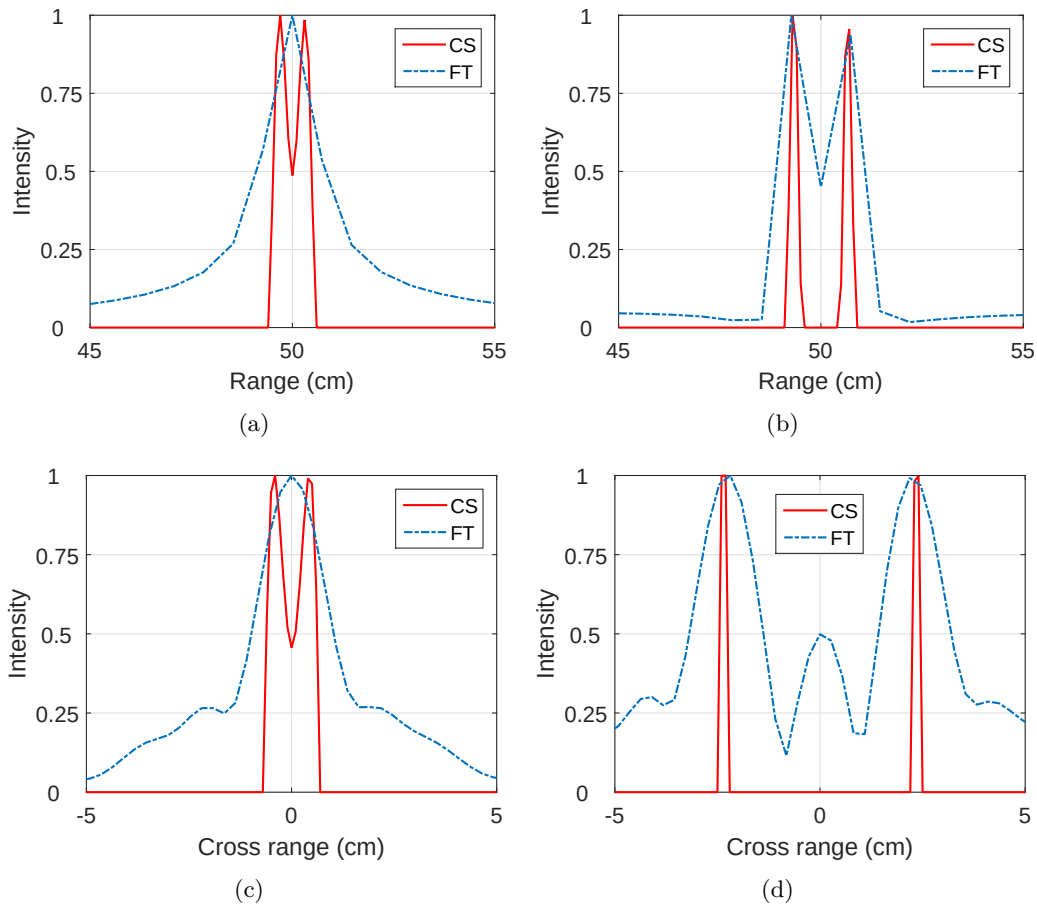


Figure 5.5: One-dimensional slice reconstruction of double-point scatterers at (a) $(0, 0, 50 \pm 0.17)$, (b) $(0, 0, 50 \pm 0.65)$, (c) $(0, \pm 0.4, 0)$ and (d) $(0, \pm 2.3, 0)$.

scheme varies the elevation angle while the switched array scheme sequentially switch on and off the linear array (varies antenna locations). It should be noted that both schemes have the same power generation, i.e., the transmitted power of each switched antenna is the same as the total transmitted power of the phased array. The imaging forward model of the switched array scheme is based on Chapter 4 by adding the attenuation factor $|\mathbf{r} - \mathbf{r}_i|^2$ as

$$\mathbf{E}(\mathbf{r}_i, k) = \iiint_V g(\mathbf{r}) \frac{\exp(-j2k|\mathbf{r} - \mathbf{r}_i|)}{|\mathbf{r} - \mathbf{r}_i|^2} \, dx \, dy \, dz, \tag{5.20}$$

where $\mathbf{E}(\mathbf{r}_i, k)$ stands for the received field at the $i$-th antenna in the array.

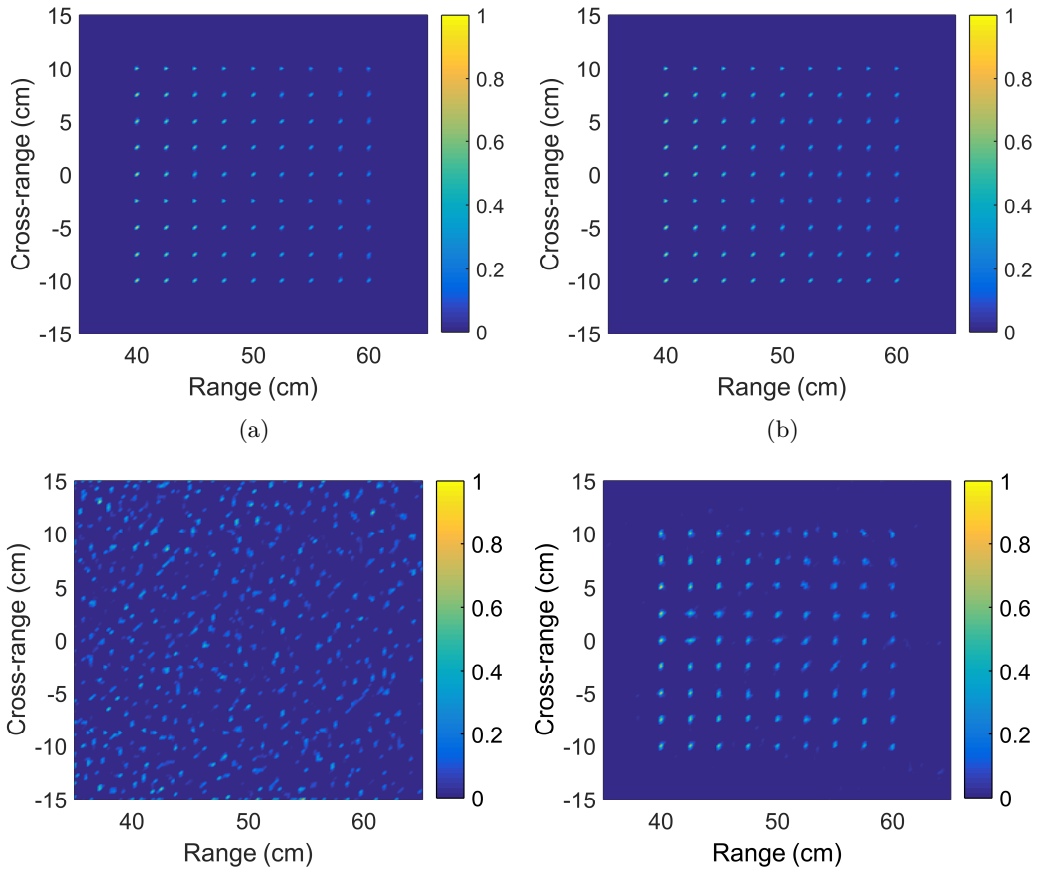


(a) (b) (c) (d)

Figure 5.6: CS reconstructions of different array configurations using the same number of measurements. (a) Switched array and (b) phased array with 20 dB SNR. (c) Switched array and (d) phased array with -50 dB SNR.

In the algorithm implementation, we ensure the regularization parameter $\lambda$ for both schemes are adjusted appropriately so that the reconstructed results are optimized. For fair comparison, the phased array scheme adopts the same number of samples as the switched array scheme, which is 40% random measurements of the fully sampled switched array scheme. Figure 5.6(a) and Figure 5.6(b) demonstrate the CS reconstruction based on switched array scheme and phased array scheme, respectively, with 20 dB SNR. Both schemes show good agreement in reconstruction. However, when the SNR level is decreased to -50 dB, as shown in Figure 5.6(c) and Figure 5.6(d), the switched array scheme fails to reconstruct the targets as the background is filled with speckles. In

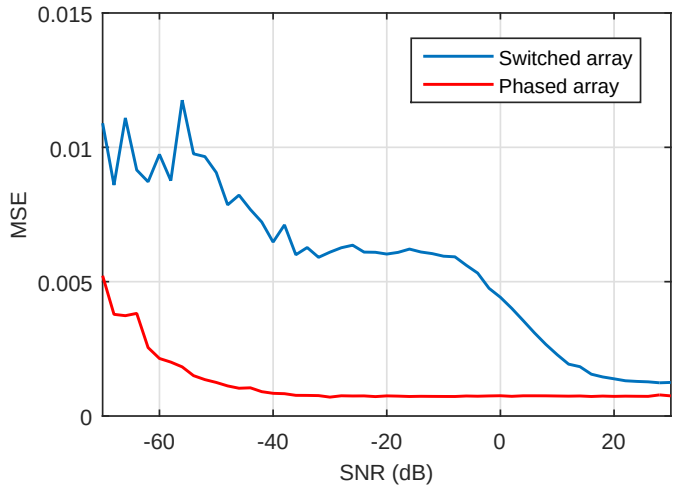


Figure 5.7: Averaged MSE comparison of switched array and phased array schemes as a function of SNR.

contrast, the phased array scheme shows acceptable reconstruction with little background noise. More specifically, Figure 5.7 depicts the averaged MSE of the two schemes as a function of SNR from -70 dB to 30 dB. For each SNR value, 10 independent trials are used to compare with the ground truth. It can be noticed that the phased array scheme achieves much lower MSE than the switched array scheme in the low SNR cases. However, this advantage gradually disappears as the SNR increases to 30 dB, which indicates both schemes, when combined with CS theory, have very similar performance when noise contribution is low.

#### 5.3.3.3 Input Parameters and Coherence Analysis

As previously explained in section 5.2, mutual coherence of the sensing matrix is proportional to the MSE values of reconstruction. In our phased array system, the sensing matrix is determined by many factors like array aperture, scanning region, frequency range and so on. With these parameters, we are more interested in designing a sensing configuration such that high quality reconstruction can be achieved. Therefore, for each realization of $\mathbf{H}$, we measure its $t_{\%}$-average mutual coherence as a prediction of the reconstruction quality. The parameter $t$ is set as 0.5, which is shown to better agrees

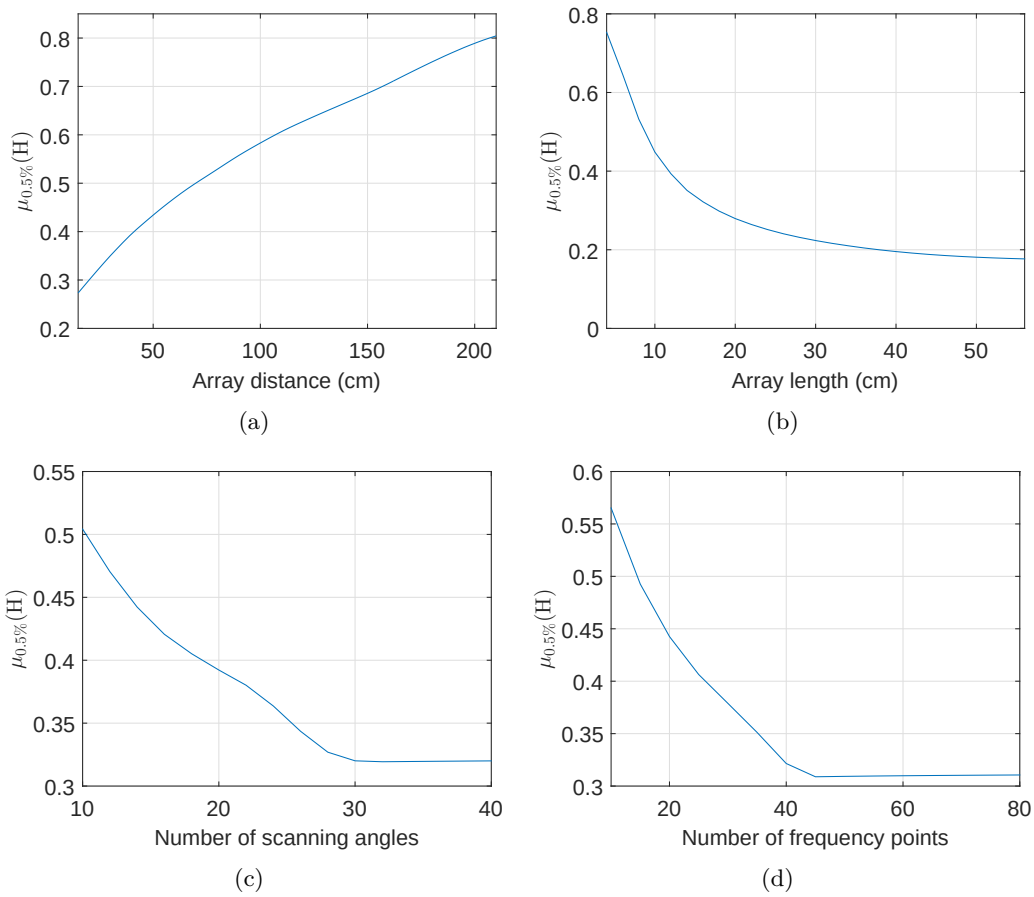


Figure 5.8: The $t_{\%}$-average mutual coherence as a function of (a) array distance, (b) array length (c) number of angles and (d) number of frequency points.

with the MSE trend [14]. All simulations are based on the 2-D case for simplicity. Only one parameter is varied at a time and other parameters are kept fixed to avoid interference. The reconstruction region is fixed in a 30 cm×30 cm area with a discretization of 101×101 pixels.

We first vary the distance between the array aperture and the reconstruction region. Forty frequency points and 80 angles are adopted for illumination. The array aperture is of length 16 cm in cross-range dimension. Figure 5.8(a) shows the $\mu_{0.5\%}(\mathbf{H})$ increases as the distance goes farther. This is expected because the distance difference among adjacent pixels approaches zero as the distance approaches infinite. In other words, the columns of $\mathbf{H}$ becomes less independent as the distance increases. Therefore, the

compressive phased array technique is better-behaved in the close range of the array aperture.

The array dimension is another important factor in the phased array system. For an array of fixed element spacing, a larger array consists of more elements. Increasing the number of elements further increases the directivity of the array, which results in more distinct system responses from pixels that are far apart from one another in cross-range direction. Figure 5.8(b) clearly interprets this relationship when 40 frequency points and 100 angles are adopted for a reconstruction area from 35 cm to 65 cm. However, increasing the array size is less effective when the length is greater than 20 cm.

Unlike the array length which is usually fixed in a given system, the range of frequencies and scanning angles are more easily adjustable. Figure 5.8(c) and Figure 5.8(d) represent the $\mu_{0.5\%}(\mathbf{H})$ variation as a function of the number of angles and frequency points, respectively. Both curves show coherence reduction as the number increases. As previously shown in Section 5.2, the number of rows of $\mathbf{H}$ is determined by the total number of frequency points and angles used. Increasing the number of frequency points or scanning angles increases the dimension of column vectors in $\mathbf{H}$. With a fixed number of columns in $\mathbf{H}$, increasing column vector dimension provides more information and hence make the columns more unique from one another. Then, similar to the array length case, when the number of scanning angles or frequency points is increased to a certain level, the $\mu_{0.5\%}(\mathbf{H})$ does not decrease anymore.

## 5.4 Compressive Phased Array Imaging with Near-field Focusing

Many security imaging applications like personnel screening and standoff concealed weapon detection are required to have short range sensing capabilities in the near-field region. The corresponding reconstruction algorithm in the near-field differs from its far-

field counterpart. This is because many assumptions made in the far-field no longer hold true in the near-field. For monostatic and MIMO arrays, this can be easily overcome by using Fourier transform based range migration algorithms [17]. However, for the phased array system, this issue has rarely been mentioned in the literature. To the author's best knowledge, the FT based algorithm for near-field phased array has not been proposed before. Although the CS method proposed in Section 5.2 is capable of both far-field and near-field imaging, its performance in the near-field region will be impaired since the beam might be unfocused or not well focused in the near-field region. This is because the beam focusing of the forward imaging model is based on the assumption of far-field approximation [5]. The electric power distribution in the near-field region can be much smaller than that in the far-field region. Therefore, it is desirable to have an imaging system such that its beams can be freely focused at any direction and any depth in the near-field region.

Near-field focusing is a well-known technique that has been used in several areas such as microwave hyperthermia and imaging in biomedical systems [18], as well as radio frequency identification (RFID) for access control [19] and library book management [20]. The main idea is to calibrate the phase of the radiating elements in such a way that all their contributions sum in phase at a focal point in the near-field region. An ID card can then be more easily identified in the near-field region than in the far-field region. Considering that the phased array has dynamic control of each element, this near-field focusing technique can be utilized in a way that the various focus points can cover the whole ROI. Although this scheme seems feasible, conventional FT reconstruction algorithms [6, 7] can not be directly applied here as the integral approximations no longer hold true in the near-field region. Therefore, a new imaging algorithm which can process the near-field focusing data is desperately needed to realize our goal.

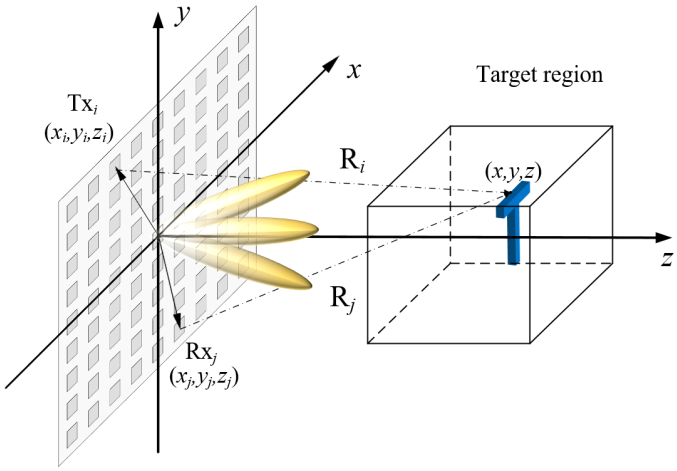


Figure 5.9: Phased array imaging system. Antenna main beam is steered toward various directions to probe the target region.

### 5.4.1 Comparison of Far-field Focusing and Near-field Focusing

Figure 5.9 shows the phased array imaging system using 2-D planar array. The amplitude and phase of each element are adjusted in the beamforming process. Assuming the element antenna is isotropic, we rewrite the scattered field in (5.7) as

$$s(k,\theta,\phi) \;=\; \iiint_V g(x,y,z) \sum_i \sum_j \frac{\exp[-jk(R_i+R_j)]}{R_i R_j} \exp[-j(\Psi_i \;+\; \Psi_j)]\, dx\, dy\, dz, \tag{5.21}$$

where $k$ is the wavenumber, $g(x,y,z)$ is the reflectivity of the target at an observing point $(x,y,z)$, $R_i$ is the distance from the $i$-th transmitting antenna to the observing point and $R_j$ is the distance from the the observing point to the $j$-th receiving antenna. $\Psi_i$ and $\Psi_j$ stand for the assigned phases to the $i$-th and $j$-th antenna, respectively.

In the conventional phased array focusing mentioned in Section 5.2, the phase term is given by [5]

$$\Psi_i = k(x_i \sin\theta\cos\phi + y_i \sin\theta\sin\phi), \tag{5.22}$$

where $(x_i, y_i, 0)$ is the coordinate of the $i$-th element. The assigned phase can steer the beam peak to the direction $(\theta,\phi)$ is because the resulting two exponential terms in

(5.21) can roughly cancel each other out in and only in that direction. Nonetheless, this approximation is only effective in the far-field region, i.e, distance greater than $2L^2/\lambda$ [5], where $\lambda$ is the wavelength. The resulting unfocused or less focused beams can degrade the imaging performance for near-field applications.

Near-field focusing technique has often been used in antenna design for RFID gate control [19]. This focusing method compensates the phase difference arising from wave propagations so that the phases of each element are equal at a desired focusing point. Consequently, the required phase of the $i$-th element to focus at a near-field point $(x_0, y_0, z_0)$ is given by

$$\Psi_i = k(\sqrt{x_0^2 + y_0^2 + z_0^2} - \sqrt{(x_0 - x_i)^2 + (y_0 - y_i)^2 + z_0^2})). \tag{5.23}$$

Figure 5.10 shows the focusing performance in terms of electric field distribution in a near-field plane of the phased array. These values are normalized to their maximum. Clearly, the focusing spot of the near-field method is much smaller than that of the far-field method. More importantly, the maximum field density of the near-field method is 7 dB greater than that of the far-field method. The sharpened beam and increased field density is favorable for the proposed near-field imaging system. By adopting this focusing method, we expect the imaging performance to be improved in the near-field region.

During data acquisition, interrogating signals are required to illuminate the whole target area. The traditional far-field focusing technique adopts equally spaced elevation and azimuth angles in scanning. However, for near-field imaging applications, this will result in many sampling points steered towards the center of the target plane and leads to too much redundancy in the acquired data. Alternatively, we adopt the near-field focusing technique and make sure full sampling points are evenly distributed in the ROI. In comparison to the far-field focusing method, this scheme can focus at different depths in the ROI and thus offers much more information in 3-D imaging applications.

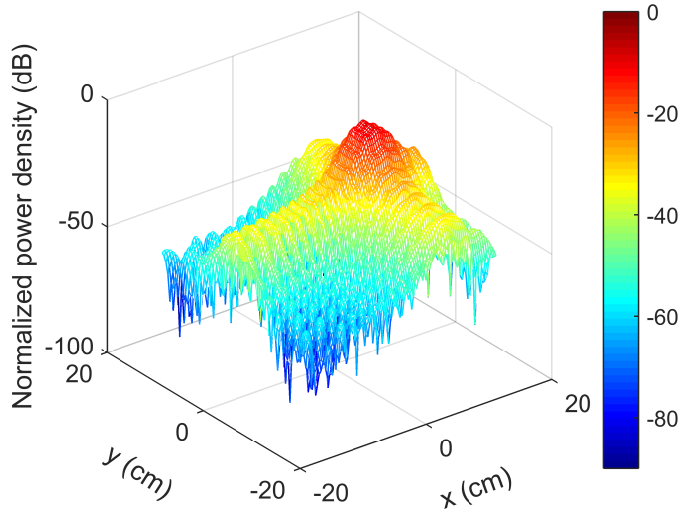


(a)

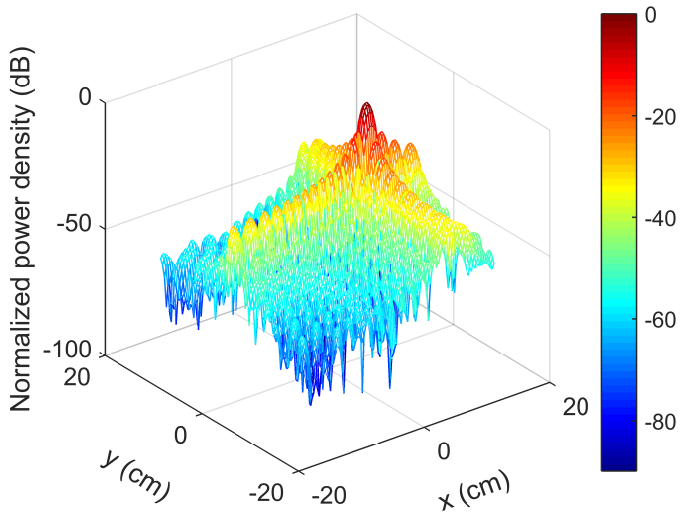


(b)

Figure 5.10: Simulated electric field distribution in the near-field region at a distance of 15 cm from a 6 cm × 6 cm aperture in 60 GHz. (a) Far-field focusing. (b) Near-field focusing.

Figure 5.11 gives an example of the sampling difference in the 2-D cross-range imaging with the same number of sampling points. The blue dots in Figure 5.11(a) represent the intersections of steered directions and the target plane, whereas the same blue dots stand for near-field focusing points in Figure 5.11(b). As mentioned previously, existing far-field FT imaging algorithms [6] are incapable of processing the data acquired by the proposed near-field sampling scheme. Instead of deriving a near-field FT method

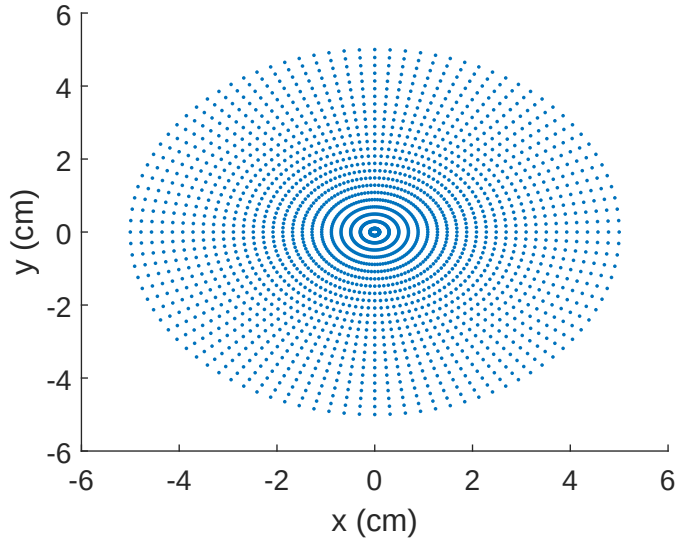


(a)

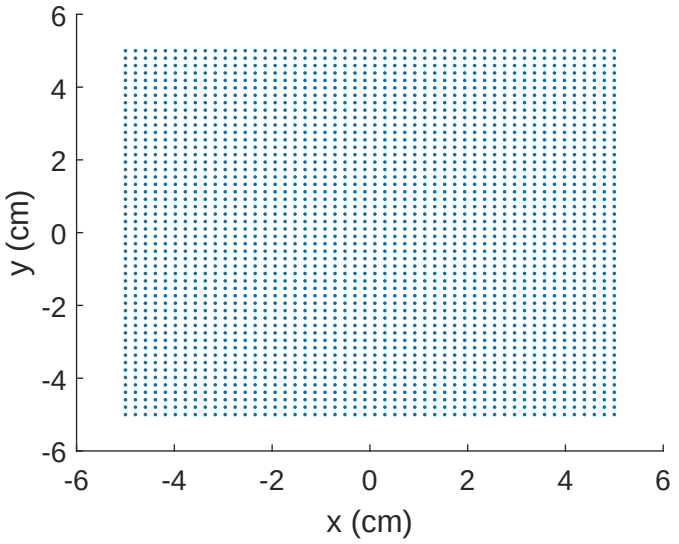


(b)

Figure 5.11: Comparison of two sampling methods in 2-D cross-range imaging case. Both methods have the same number of measurements. (a) Intersection points of the angle steered beams and the target plane. (b) Sampling points of the proposed near-field method on the target plane.

algorithm, we integrate the CS theory in our sampling scheme, as will be demonstrated in the next subsection.

### 5.4.2 Compressive Sensing Implementation based on Near-field Focusing Technique

In order to apply CS to the imaging model, the sampled data needs to be discretized first. Let $P$, $Q$, $M$ and $N$ be the number of focused points, frequency points, elements in the phased array and voxel points in the target region, respectively. The scattered field that focused at the $p$-th point with the $q$-th frequency can be rewritten as

$$s(p,q) = \sum_{i=1}^{M}\sum_{j=1}^{M}\sum_{l=1}^{N} g(l)\frac{\exp[-j(k(q)(R_i+R_j)+\Psi_i+\Psi_j)]}{R_iR_j}, \tag{5.24}$$

where $\Psi_i$ and $\Psi_j$ are given by (5.23), $g(l)$ is the reflectivity of the $l$-th voxel. $R_i$ ($R_j$) represents the distance from the $i$-th ($j$-th) antenna to the $l$-th voxel in the target region. The matrix multiplication form of (5.24) can then be expressed as

$$\mathbf{s} = \mathbf{H}\mathbf{g}, \tag{5.25}$$

where $\mathbf{s}$ is of dimension $PQ \times 1$ and $\mathbf{g}$ is of dimension $N \times 1$. $\mathbf{H}$ is the system response matrix whose entries are determined by the exponential term in (5.24). With the CS theory, the number of sampling points in the spatial domain and the frequency domain can be greatly reduced while satisfactory reconstruction can still be achieved. Similarly, we use matrix $\mathbf{A}$ as the undersampling operator. Let $\mathbf{y}$ be the undersampled data, then the final CS model can be written as

$$\mathbf{y} = \mathbf{A}\mathbf{H}\mathbf{g}. \tag{5.26}$$

The final minimization problem that will be solved by the TwIST algorithm is expressed as:

$$\hat{\mathbf{g}} = \underset{\mathbf{g}}{\operatorname{argmin}}\,\frac{1}{2}\,\|\mathbf{A}\mathbf{H}\mathbf{g}-\mathbf{y}\|_2^2 + \lambda\|\mathbf{g}\|_{TV}, \tag{5.27}$$

where $\|\bullet\|_{TV}$ is the TV of both the real and imaginary parts of $\mathbf{g}$. Note that TV

regularization is adopted to promote sparsity when complicated targets are employed. For point targets, we still use $\ell_1$ norm for simplicity.

### 5.4.3 Numerical Results and Analysis

To examine the effectiveness of the proposed method, we compare its image reconstruction performance to the far-field method in the near-field region. As the 3-D reconstruction is computationally very expensive and requires high memory usage, the construction of the $\mathbf{H}$ matrix can be extremely time-consuming when a fine grid is adopted. Therefore, we simplify the imaging analysis by discussing the 2-D cross-range image reconstruction using single frequency signals. The simulation is carried out in the MMW frequency range at 60 GHz. The length of the array is 8 cm in both $x$ and $y$ dimensions with an element spacing fixed at $0.5\lambda$, resulting in $33 \times 33$ elements in total. Targets with uniform reflectivity are placed 15 cm away from the aperture. According to $2L^2/\lambda = 256$ cm, the targets are in the near-field zone. The discretization of the target plane is related to the quality of reconstruction. In general, the discretization interval should be smaller than the resolution of the system to avoid grid mismatch. Here we define the ROI as a square of 10 cm $\times$ 10 cm with discretization of 101 $\times$ 101 pixels.

#### 5.4.3.1 Resolution

It has been shown that the far-field CS method outperforms the traditional Fourier method in both range and cross-range dimensions. However, the resolution based on near-field focusing method is still unknown. Theoretically, due to the same aperture size, the focusing approach should have little impact on the imaging resolution while using conventional FT algorithms. According to the resolution formula introduced in (2.9), the cross-range resolution for the 8 cm $\times$ 8 cm array configuration is 0.47 cm at $R = 15$ cm. To examine whether the resolution of the near-field CS method differs from its far-field counterpart, the following example is given.

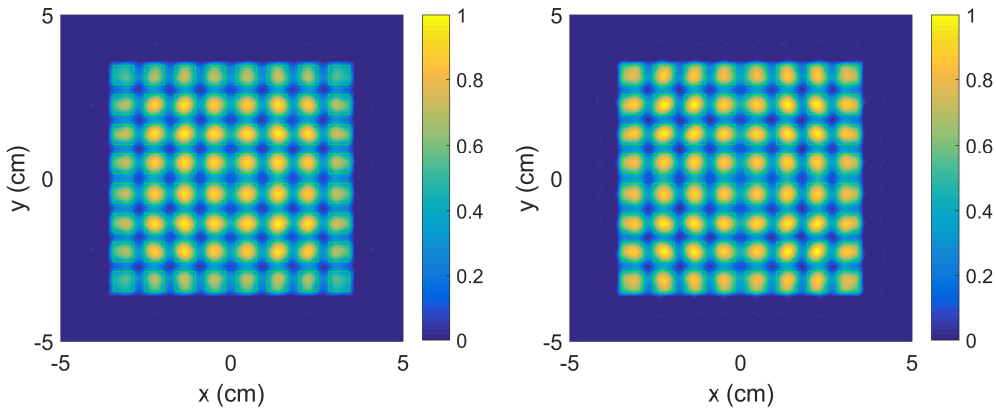


(a) (b)

Figure 5.12: Image reconstruction of 64 squares by the (a) far-field focusing and (b) near-field focusing methods. The squares have 0.6 cm length and 0.3 cm spacing. Ground truth targets are also marked in green dotted lines for reference.

We employ 64 squares with 0.6 cm length and 0.3 cm spacing in the target scene. The reconstructed images are shown in Figure 5.12(a) and Figure 5.12(b), respectively. The contours of the ground truth targets are also marked in green dotted lines as references. Although not perfect, the square targets can still be resolved in both cases, indicating they have similar resolving power. It can also be noticed that in the far-field focusing case, the reconstructed squares farther from the center are relatively less discernible. This result implies that the uniform angle scanning method can cause information loss near the boundary of the scanning region. In comparison, the uniform scanning approach can perfectly solve this issue.

#### 5.4.3.2 Noise Effect

We manually add Independent and Identically Distributed (i.i.d.) Gaussian noise to each of the receiving antennas just like what we did in Chapter 5. Note that the SNR calculation is based on the average signal power at the receiving antennas [12].

In the first example, we consider $5 \times 5$ equally spaced point scatterers in the target region. The spacing of the scatterers is 1.5 cm. Figure 5.13(a) and Figure 5.13(b)

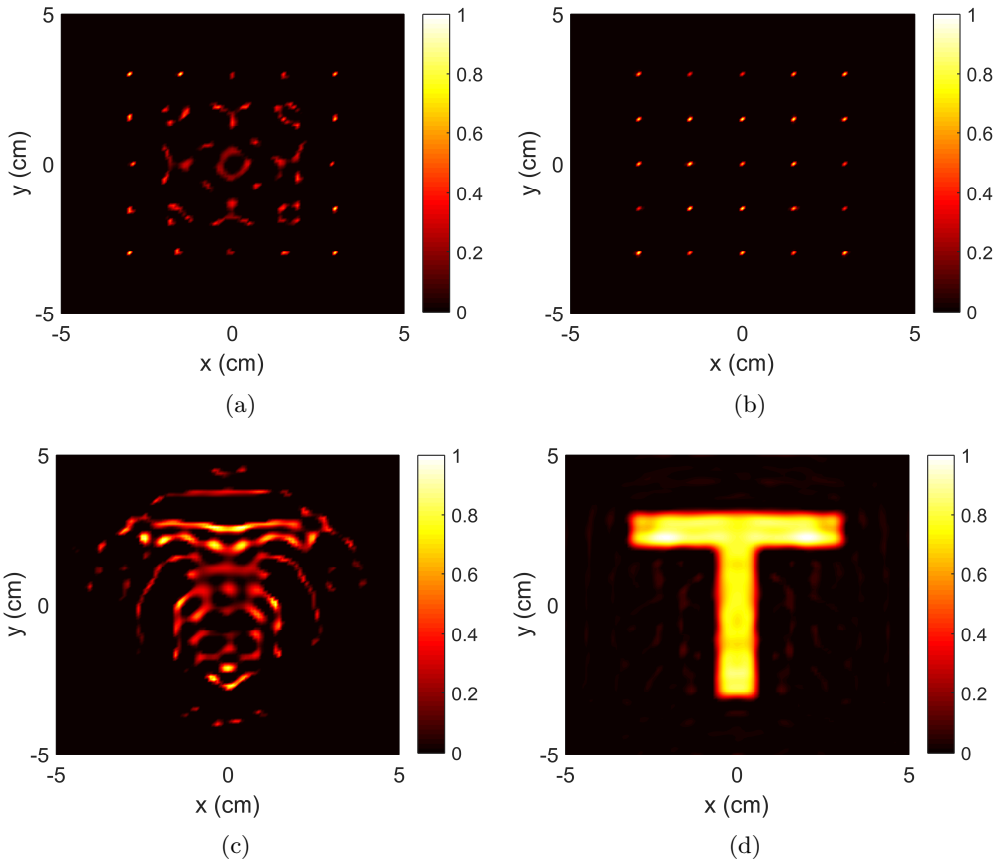


Figure 5.13: Two-dimensional reconstruction of targets at a distance of 15 cm from the aperture under -50 dB SNR. $5 \times 5$ point scatterers reconstruction of (a) far-field method and (b) near-field method. T-shaped target reconstruction of (c) far-field method and (d) near-field method.

demonstrate the image reconstruction of two focusing methods with an SNR of -50 dB. Only 20 % random samples are selected from the full $70 \times 70$ samples. The far-field focusing scheme shows deteriorated reconstruction as the scatterers in the center can not be clearly identified. In contrast, the near-field approach still gives correct reconstruction of all point scatterers.

For most imaging systems, the target may not be sparse at all. In such cases, aforementioned point scatterer example is no longer appropriate to represent the imaging performance. Taking this into consideration, a more complex 2-D T-shaped target, with a height of 6 cm and width of 6 cm, is adopted in the second example. Since the

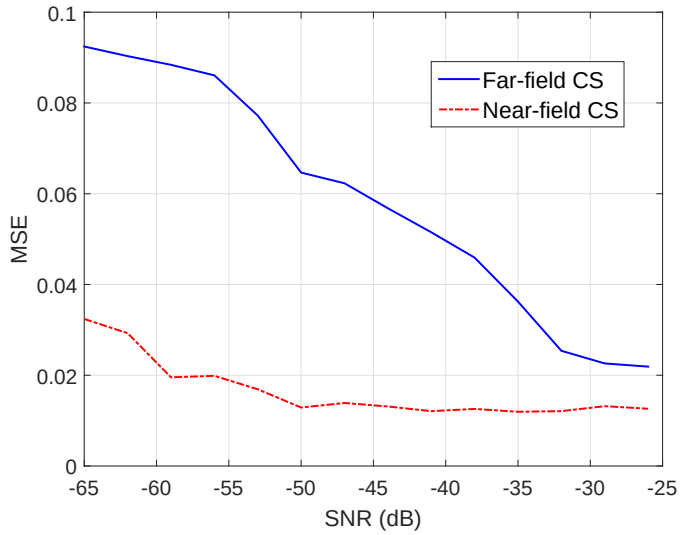


Figure 5.14: Averaged MSE comparison of the far-field and near-field schemes as a function of SNR.

target is not as sparse as in the first example, it requires more measurements for acceptable reconstruction. Figure 5.13(c) and Figure 5.13(d) demonstrate the corresponding reconstructions using 30 % random samples with the same -50 dB SNR. The near-field approach clearly shows much better reconstruction than the far-field focusing scheme with only limited background noise. More specifically, Figure 5.14 quantitatively summarizes the averaged MSE of the two methods as a function of SNR from -65 dB to -25 dB. Each SNR value is averaged over 15 independent trials. It can be noticed that the near-field method outperforms the far-field method. Both examples confirm that the near-field focusing technique enables robust image reconstruction in the presence of high background noise. This advantage helps to reduce the imaging system cost, e.g., using lower transmitting power and low gain antenna element.

#### 5.4.3.3 Background Interference

In security imaging applications like conceal weapon detection in the airport, we are more interested in imaging within a certain range. Objects outside the ROI might interfere with the person under scanning. A good imaging system is supposed to be capable of

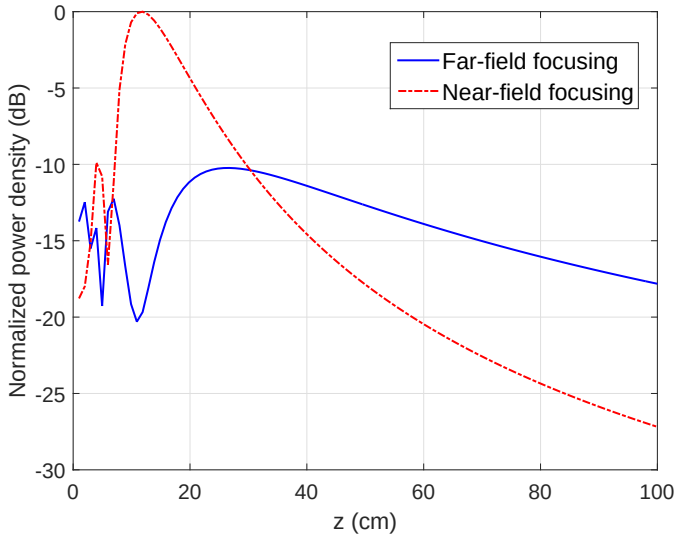


Figure 5.15: Normalized power density along the $z$-axis as a function of the distance from the aperture.

minimizing such interference. To understand how the near-field method works in such situations, we set the radiated power density of a 6 cm $\times$ 6 cm array along the range direction, as shown in Figure 5.15. The near-field method focuses at a near-field point on the $z$-axis where $z = 15$ cm while the far-field method steers its beam along the $z$-axis. The power density of the near-field method reaches its peak at around $z = 12$ cm, which means the array will receive its strongest reflection from a point scatterer at $z = 12$ cm. A point scatterer at $z = 20$ cm will lead to about 5 dB decrease in the receiving power. Seeing that the power density of the near-field focusing method apparently decays more rapidly than that of the corresponding far-field method, we expect it to be more robust to interference from outside the ROI.

To evaluate the effectiveness of this property, we introduce two rectangular plates as interfering targets and place them 20 cm away from the T-shaped target. The simulation is based on 50% random data with 60 dB SNR. Other parameters are kept the same as in the second example. Figure 5.16(a) and Figure 5.16(b) demonstrate the 2-D cross-range view and 3-D view of the composite target, respectively. Both plates are of size 0.5 cm $\times$ 1 cm and share the same reflectivity as the T-shaped target. The reconstruction results are shown in Figure 5.16(c) and Figure 5.16(d). We can clearly see the near-field method

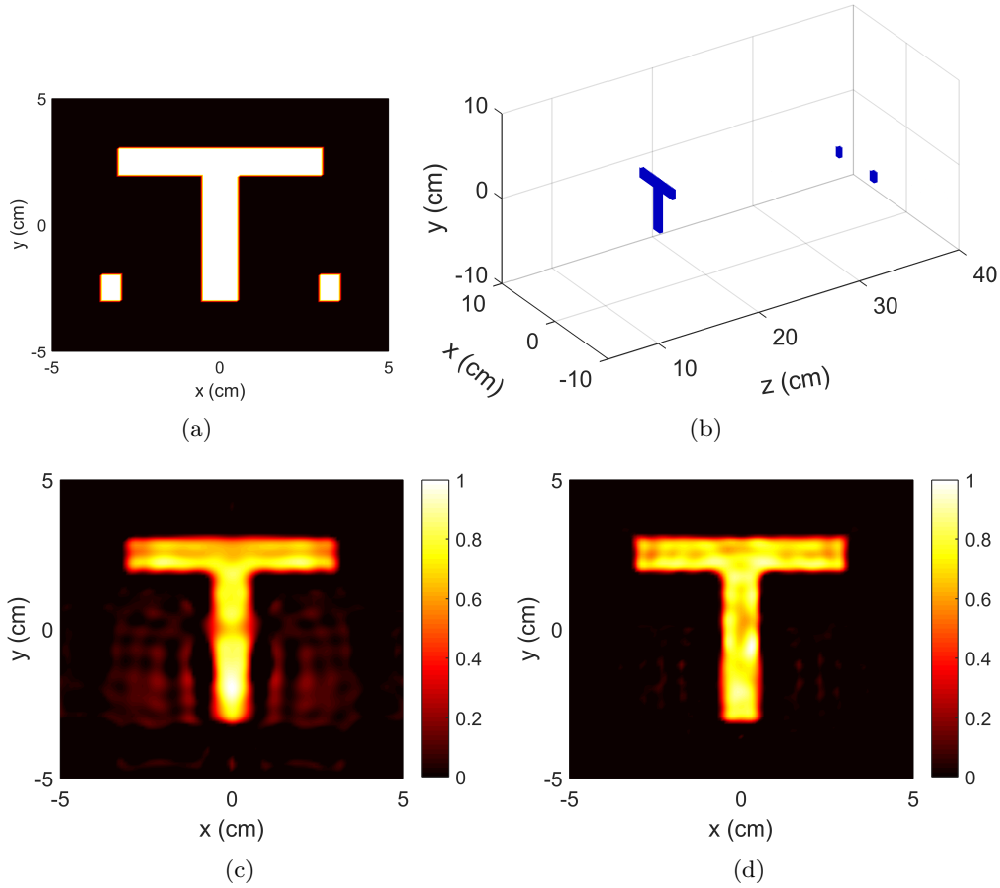


Figure 5.16: Composite target visualization. (a)Cross range view. (b) 3-D view. Two-dimensional images are reconstructed using 50% data under 60 dB SNR. (c) Far-field method. (d) Near-field method.

achieves better robustness against the interfering targets.

## 5.5 Summary

In this chapter, a general 3-D compressive imaging model has been derived for phased array systems. With the CS theory, far fewer angles and frequency points are required for image reconstruction, which further accelerate the scanning speed of phased array imaging systems. The image reconstruction performance of the proposed method are demonstrated with both qualitative and quantitative results. Particularly, the resolving power has been significantly enhanced about 74% and 68% in range and cross-range

dimensions, respectively. The effect of implementation aspects including array distance, array length, number of angles and number of frequency points have also been presented as guidelines on how to design sensing configurations for better CS reconstruction.

Furthermore, we presented a compressive near-field phased array imaging method. The basic idea is to apply near-field focusing technique to strengthen the beamforming performance in the near-field region. A new scanning method has also been provided to focus array beams at different spots with various depths so that they can cover the whole target region. Compared to the far-field imaging approach, the new method has superior performance in imaging applications where the object is in the near-field zone of the array aperture. The increased robustness under noisy environment also help to lower the system requirements on transmitting power and antenna design.

## References

[1] K. B. Cooper, R. J. Dengler, N. Llombart, T. Bryllert, G. Chattopadhyay, E. Schlecht, J. Gill, C. Lee, A. Skalare, I. Mehdi *et al.*, "Penetrating 3-d imaging at 4-and 25-m range using a submillimeter-wave radar," *IEEE Transactions on Microwave Theory and Techniques*, vol. 56, no. 12, pp. 2771–2778, 2008.

[2] K. Cooper, R. Dengler, G. Chattopadhyay, E. Schlecht, J. Gill, A. Skalare, I. Mehdi, and P. Siegel, "A high-resolution imaging radar at 580 ghz," *IEEE Microwave and wireless components letters*, vol. 18, no. 1, pp. 64–66, 2008.

[3] K. B. Cooper, R. J. Dengler, N. Llombart, B. Thomas, G. Chattopadhyay, and P. H. Siegel, "Thz imaging radar for standoff personnel screening," *IEEE Transactions on Terahertz Science and Technology*, vol. 1, no. 1, pp. 169–182, 2011.

[4] J. Li and P. Stoica, "The phased array is the maximum snr active array," *IEEE Signal Processing Magazine*, vol. 27, no. 2, pp. 143–144, 2010.

[5] R. J. Mailloux, "Phased array antenna handbook," *Boston, MA: Artech House,*

*1994.*, 1994.

[6] M. Soumekh, "Array imaging with beam-steered data," *IEEE Transactions on Image Processing*, vol. 1, no. 3, pp. 379–390, Jul 1992.

[7] S. Patole and M. Torlak, "Two dimensional array imaging with beam steered data," *IEEE Transactions on Image Processing*, vol. 22, no. 12, pp. 5181–5189, Dec 2013.

[8] S. S. Chen, D. L. Donoho, and M. A. Saunders, "Atomic decomposition by basis pursuit," *SIAM review*, vol. 43, no. 1, pp. 129–159, 2001.

[9] E. J. Candès, "The restricted isometry property and its implications for compressed sensing," *Comptes Rendus Mathematique*, vol. 346, no. 910, pp. 589 – 592, 2008.

[10] E. Candès and J. Romberg, "Sparsity and incoherence in compressive sampling," *Inverse Problems*, vol. 23, no. 3, pp. 969–985, 2007.

[11] J. M. Duarte-Carvajalino and G. Sapiro, "Learning to sense sparse signals: Simultaneous sensing matrix and sparsifying dictionary optimization," *IEEE Transactions on Image Processing*, vol. 18, no. 7, pp. 1395–1408, 2009.

[12] G. Lipworth, A. Mrozack, J. Hunt, D. L. Marks, T. Driscoll, D. Brady, and D. R. Smith, "Metamaterial apertures for coherent computational imaging on the physical layer," *J. Opt. Soc. Am. A*, vol. 30, no. 8, pp. 1603–1612, 2013.

[13] M. Elad, "Optimized projections for compressed sensing," *IEEE Transactions on Signal Processing*, vol. 55, no. 12, pp. 5695–5702, 2007.

[14] I. Stojanovic, M. Cetin, and W. C. Karl, "Compressed sensing of monostatic and multistatic SAR," *IEEE Geoscience and Remote Sensing Letters*, vol. 10, no. 6, pp. 1444–1448, 2013.

[15] L. I. Rudin, S. Osher, and E. Fatemi, "Nonlinear total variation based noise removal algorithms," *Physica D: Nonlinear Phenomena*, vol. 60, no. 1, pp. 259–268, 1992.

[16] M. Soumekh, *Fourier array imaging.* Prentice-Hall, Inc., 1994.

[17] J. M. Lopez-Sanchez and J. Fortuny-Guasch, "3-d radar imaging using range migration techniques," *IEEE Transactions on Antennas and Propagation*, vol. 48,

no. 5, pp. 728–737, May 2000.

[18] X. He, W. Geyi, and S. Wang, "A hexagonal focused array for microwave hyperthermia: Optimal design and experiment," *IEEE Antennas and Wireless Propagation Letters*, vol. 15, pp. 56–59, 2016.

[19] A. Buffi, A. A. Serra, P. Nepa, H. . T. Chou, and G. Manara, "A focused planar microstrip array for 2.4 ghz rfid readers," *IEEE Transactions on Antennas and Propagation*, vol. 58, no. 5, pp. 1536–1544, May 2010.

[20] H.-W. Liu, C.-H. Weng, C.-F. Yang, Y.-S. Lin, F.-S. Chen, Y.-C. Huang, and C.-W. Hsu, "Design of rfid near-field focusing circular patch array antenna at 2.4 ghz with applications," in *Internet of Things (IOT), 2010*. IEEE, 2010, pp. 1–4.

# Chapter 6

# Comparative Study of Compressive Sensing Methods in Different Array Configurations

## 6.1 Introduction

The previous two chapters have demonstrated the effectiveness of CS methods in switched array and phased array configurations. In comparison with conventional FT methods, CS methods can achieve better image reconstruction with far fewer samples. The CS implementation in these two approaches is carried out in a similar way. The only difference is the construction of the system response matrix. To better understand this, we consider the rows of the response matrix as different signal modes used to interrogate the target scene. Then each mode in the switched array case is related to the radiation pattern of an antenna at a particular position using a particular frequency. On the other hand, in the phased array case, these modes are determined by different frequency points and beam steering angles. According to the CS theory, a response matrix that strictly satisfies the RIP or has low mutual coherence leads to high stability in reconstruction.

The discrepancy in constructing the response matrix might lead to different imaging performance. Among the three array configurations introduced in Chapter 2, one would like to know how they differ from each other under similar system specifications. Therefore, this chapter aims to investigate the performance of CS methods with different antenna array schemes.

This chapter is organized as follows. The MIMO array design and its CS implementation are presented in Section 6.2. Then Section 6.3 gives the numerical analysis of CS methods using switched array, MIMO array and phased array configurations. Conclusions are drawn in Section 6.4.

## 6.2 Compressive MIMO Array Imaging

As we have mentioned in Chapter 2, security imaging for personnel screening requires relatively large area to operate. By satisfying the half a wavelength element spacing criterion, the switched array approach will end up with an extremely dense array to achieve a moderate aperture size and resolution. The fabrication of such a dense array is still prohibitive using existing technologies and can cause several other problems such as heavy weight, complex electronics, large data flow, severe mutual coupling. The MIMO array configuration offers an alternative way to solve these issues by using only a small number of spatially distributed transmit and receive antennas. In this section, we will explain a typical imaging MIMO array design and present the compressive MIMO array imaging method.

### 6.2.1 MIMO Array Design

The ultimate goal of MIMO array design is to obtain an array topology that achieves the required imaging performance with a minimum number of antenna elements. The array performance is usually evaluated by the well-known point spread function (PSF).

The PSF describes the response of an imaging system to a point source or point object. According to the formulation introduced in [1], the PSF of an UWB MIMO array can be expressed as

$$\mathrm{PSF}_{\mathrm{WB}} = \int_{\{\mathbf{r}_{\mathrm{Tx}}\}} (4\pi|\mathbf{r}_0 - \mathbf{r}_{\mathrm{Tx}}|)^{-1} \cdot \omega_{\mathrm{Tx}}(\mathbf{r}_{\mathrm{Tx}}) \cdot \delta(t - \mathrm{T}_{\mathrm{Tx}}(\mathbf{r}, \mathbf{r}_{\mathrm{Tx}}))\mathrm{d}\mathbf{r}_{\mathrm{Tx}} \\ * \int_{\{\mathbf{r}_{\mathrm{Rx}}\}} (4\pi|\mathbf{r}_{\mathrm{Rx}} - \mathbf{r}_0|)^{-1} \cdot \omega_{\mathrm{Rx}}(\mathbf{r}_{\mathrm{Rx}}) \cdot \delta(t - \mathrm{T}_{\mathrm{Rx}}(\mathbf{r}, \mathbf{r}_{\mathrm{Rx}}))\mathrm{d}\mathbf{r}_{\mathrm{Rx}} \quad (6.1)$$

where $*$ denotes convolution in the time domain, $\mathbf{r}_0$ is the position of the target, $\mathbf{r}$ denotes the focusing point, and $\mathbf{r}_{\mathrm{Tx}}$ and $\mathbf{r}_{\mathrm{Rx}}$ represent the location of the transmit and receive elements, respectively. The aperture function $\omega_{\mathrm{Tx}}$ and $\omega_{\mathrm{Rx}}$ define the distribution of antenna elements within the transmit and receive apertures, respectively, and

$$\begin{aligned} \mathrm{T}_{\mathrm{Tx}}(\mathbf{r}, \mathbf{r}_{\mathrm{Tx}}) &= (|\mathbf{r}_0 - \mathbf{r}_{\mathrm{Tx}}| - |\mathbf{r} - \mathbf{r}_{\mathrm{Tx}}|)/c \\ \mathrm{T}_{\mathrm{Rx}}(\mathbf{r}, \mathbf{r}_{\mathrm{Rx}}) &= (|\mathbf{r}_{\mathrm{Rx}} - \mathbf{r}_0| - |\mathbf{r}_{\mathrm{Rx}} - \mathbf{r}|)/c. \end{aligned} \quad (6.2)$$

As we can see from (6.1), the PSF of the complete MIMO aperture is determined by the convolution between the transmit and receive apertures. The convolution of aperture functions is equivalent to a synthetic aperture function whose elements are the midpoints of the lines connecting each transmit/receive pair. This synthetic aperture is also known as virtual aperture and its virtual elements are assumed as co-located transmit/receive transceivers like the switched array configuration [1, 2]. While such a relation is exact in the far-field, it is approximate in the near-field which results in a moderate deviation of beam pattern between the MIMO array and its virtual aperture. Fortunately, this deviation is still acceptable, allowing the virtual aperture concept to be an effective MIMO array design tool [3].

The MIMO array design process is as follows. Firstly the number of virtual array elements $N_{\mathrm{E}}$ is determined either by the requirement of the minimum sidelobe level and system specifications. The ideal sidelobe level defined as $ISL = -20\log_{10}N_{\mathrm{E}}$ is usually

used to determine the minimum required number of elements. The exact value of $N_{\mathrm{E}}$ depends on the element spacing and aperture size. Then the minimum required aperture size $L$ is obtained by the cross-range resolution formula

$$L_{x,y} = \frac{\lambda D}{2\delta_{x,y}}, \tag{6.3}$$

where $D$ is the target range, $\lambda$ is the wavelength at the center frequency and $\delta_{x,y}$ is the required resolution in cross-range dimensions. Next, the numbers of transmit and receive antennas are chosen by $N_{\mathrm{E}} = N_{\mathrm{Tx}} \cdot N_{\mathrm{Rx}}$ which makes the total number of antennas as $N_{\mathrm{total}} = N_{\mathrm{Tx}} + N_{\mathrm{Rx}}$. Note that this relation is invalid when array redundancy exists, e.g., two or more virtual elements overlap within the virtual aperture. Because of different choices of sub-arrays, the factorization of $N_{\mathrm{E}}$ is not unique and allows for multiple solutions. The optimal choice should consider some practical issues, such as aperture size, mutual coupling and overall system cost. This process is to some extent similar to the conventional array pattern synthesis where numerical methods can be applied to optimize the MIMO topology iteratively. There also exist some other MIMO array design approaches but they are out of the scope of this thesis. A detailed discussion of 1-D and 2-D MIMO array design can be found in [4].

It is worth noting that from the imaging point of view, high level grating lobes can severely impair the imaging performance, and in extreme cases produce overlapping multiple images of the same target [4]. Generally, for narrow band arrays, the element spacing is usually chosen to be smaller than half a wavelength to avoid grating lobes. In the UWB case, the element spacing can be slightly relaxed to a larger distance while keeping the sidelobe level under control [5]. Here we take the narrow band MIMO array design as an example. Suppose we want to have an imaging system with 1 cm cross-range resolution at a distance of 50 cm. The frequency of the system is 30 GHz (wavelength is 1 cm). According to (6.3), the required aperture size of the virtual aperture should be at least 20 cm in both $x$ and $y$ dimensions. To reduce the computational complexity, we set the aperture size as 20 cm in both dimensions. $40 \times 40$ antennas (elements spacing

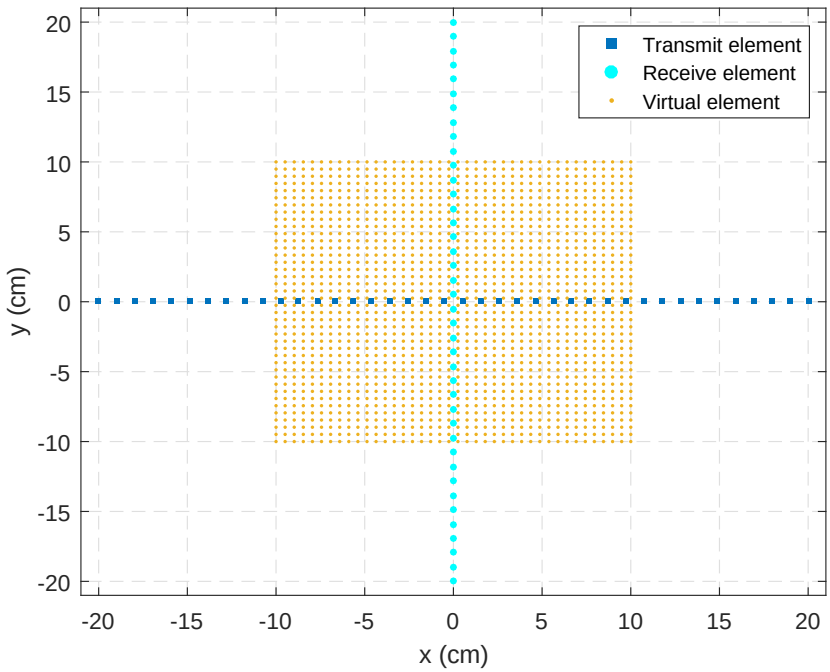


Figure 6.1: Cross MIMO array and its equivalent virtual array.

is around half-wavelength) are employed to satisfy the narrowband requirement. To obtain an equivalent MIMO array, we adopt the cross array topology with orthogonal transmit array and receive array. The total number of antennas of the MIMO array will be minimal when $N_{\mathrm{Tx}} = N_{\mathrm{Rx}} = 40$.

Figure 6.1 shows the geometry of the MIMO array and its equivalent virtual aperture. It can be noticed that virtual elements form a perfect uniform square array. In comparison, the MIMO configuration uses only 80 antennas to achieve a comparable performance of a $40 \times 40$ switched array. This huge reduction of antennas makes MIMO array a promising scheme towards real-time imaging applications. Due to the nature of sperate transmit and receive arrays, MIMO array typically has larger size than its equivalent switched array. As shown in the figure, the cross MIMO array aperture is twice the size of the virtual aperture.

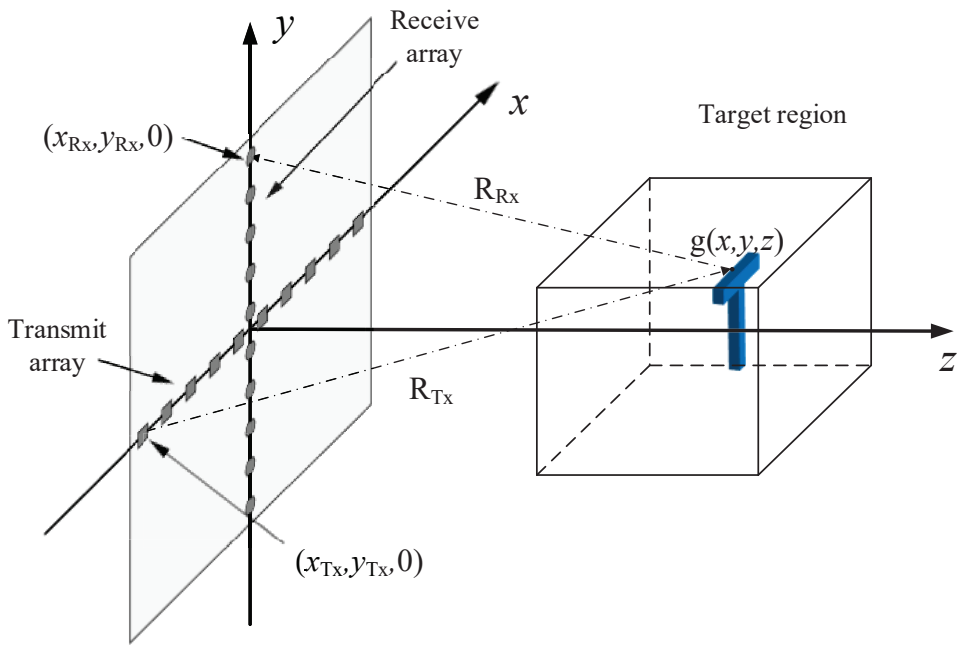


Figure 6.2: Cross MIMO array imaging system.

### 6.2.2 CS Implementation

An example MIMO array imaging system with cross configuration is shown in Figure 6.2. Assuming the same BA as we did in both the switched array and phased array cases, the received field at the corresponding transceiver pair can be expressed as

$$s(x_{\mathrm{Tx}}, y_{\mathrm{Tx}}, x_{\mathrm{Rx}}, y_{\mathrm{Rx}}, k) = \iiint_V \frac{g(x,y,z)}{R_{\mathrm{Tx}} R_{\mathrm{Rx}}} \exp(-jkR_{\mathrm{Tx}}) \exp(-jkR_{\mathrm{Rx}})\, dx\, dy\, dz, \tag{6.4}$$

where $k$ is the wavenumber at frequency $f$, $R_{\mathrm{Tx}}$ and $R_{\mathrm{Rx}}$ are the distances from the transmitter and receiver to the target, respectively, as shown in the following:

$$\begin{aligned} R_{\mathrm{Tx}} &= \sqrt{(x_{\mathrm{Tx}} - x)^2 + (y_{\mathrm{Tx}} - y)^2 + (z - 0)^2} \\ R_{\mathrm{Rx}} &= \sqrt{(x_{\mathrm{Rx}} - x)^2 + (y_{\mathrm{Rx}} - y)^2 + (z - 0)^2}. \end{aligned} \tag{6.5}$$

This signal model takes into consideration the spreading losses due to the free-space propagation just like the switched array model (5.20) shown in Chapter 5. In comparison, the electromagnetic wave in the MIMO signal model travels further than the switched

array case due to separate transmitter and receiver pair. The reflectivity map $g(x, y, z)$ can be obtained by using 3D-IFT in a similar way like the switched array case. Interested readers are referred to [6] for a detailed derivation of the FT based MIMO imaging algorithm.

While the range resolution of the MIMO array is still the same as the switched array and phased array, the cross-range resolutions are related to the widths of the transmit and receive arrays:

$$\begin{aligned} \delta_x &= \frac{\lambda D}{L_{\text{Tx_}x} + L_{\text{Rx_}x}} \\ \delta_y &= \frac{\lambda D}{L_{\text{Tx_}y} + L_{\text{Rx_}y}}, \end{aligned} \tag{6.6}$$

where $L_{\text{Tx_}x}$ and $L_{\text{Rx_}x}$ are the widths of the transmit and receive apertures along the horizontal direction, whereas $L_{\text{Tx_}y}$ and $L_{\text{Rx_}y}$ are the widths along the vertical direction. Since the width of the receive array along the horizontal direction is almost negligible, the resolution in the horizontal direction is actually determined by the length of the transmit array. Recall that the cross-range resolution of a switched array is $\delta_x = \lambda D/2L_x$, it is easy to calculate that the cross MIMO array needs twice the size of the switched array to achieve the same resolution.

The discretization process of the MIMO forward imaging model is the same as previous chapters. Let $M$, $N$, $Q$ and $L$ be the number of transmit antennas, receive antennas, frequency points and voxel points in the target region, respectively. The scattered field due to a signal transmitted from the $m$-th transmit antenna and received by the $n$-th receive antenna with the $q$-th frequency can be rewritten as

$$s(m, n, q) = \sum_{l=1}^{L} g(l) \frac{\exp[-jk(q)(R_{\text{Tx}}(m, l) + R_{\text{Rx}}(n, l))]}{R_{\text{Tx}}(m, l) R_{\text{Rx}}(n, l)}, \tag{6.7}$$

where $g(l)$ is the reflectivity of the $l$-th voxel and $k(q)$ is the wavenumber of the $q$-th

frequency. The CS model of (6.7) is then expressed in a matrix multiplication form as

$$\mathbf{s} = \mathbf{H}\mathbf{g}, \tag{6.8}$$

where $\mathbf{s}$ is of dimension $MNQ \times 1$ and $\mathbf{g}$ is of dimension $L \times 1$. After adding the undersampling operator $\mathbf{A}$, the final CS model can be written as

$$\mathbf{y} = \mathbf{A}\mathbf{H}\mathbf{g}. \tag{6.9}$$

The recovery of the reflectivity map is the same as the compressive switched array and phased array imaging. Different sparsity transformations can be utilized to promote sparsity during reconstruction.

## 6.3 Numerical Analysis

As has been shown in previous chapters, D-CS method offers better resolving abilities than conventional Fourier methods in switched array and phased array imaging. Its performance on the three array configurations will be studied in this section. To make the comparison less computational demanding, single frequency cross-range 2-D imaging is considered. The array parameters concerning aperture size, element spacing, target distance and frequency selection follow the example in the above cross MIMO array design. That is, the switched array and the phased array use the same array geometry; the MIMO array is designed to have a virtual aperture that is equivalent to the switched array.

The imaging area is 20 cm $\times$ 20 cm which is the same as the switched array aperture size. This area is discretized into 81 $\times$ 81 pixels which makes the grid spacing as 0.25 cm. The target to array aperture distance is set as 50 cm. As 50 cm is still in the near-field region, the near-field focusing technique is considered for the phased array

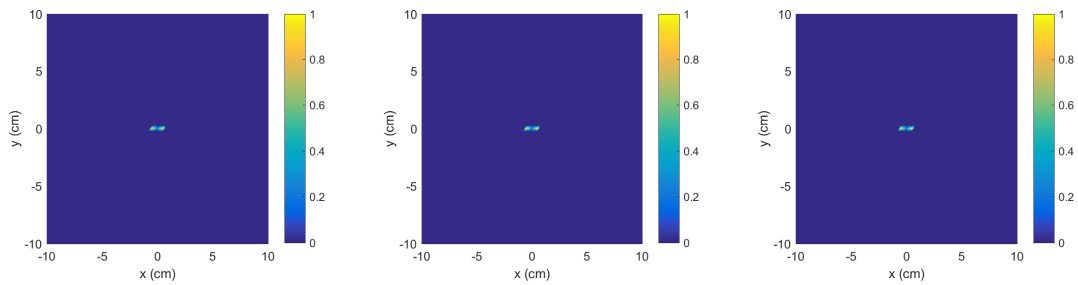


(a) (b) (c)

Figure 6.3: Image reconstruction of two point scatterers with a spacing of 0.8 cm by the (a) switched array, (b) MIMO array and (c) phased array.

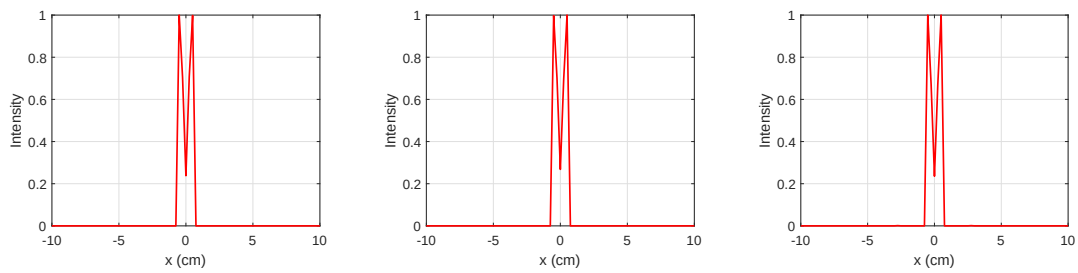


(a) (b) (c)

Figure 6.4: One-dimensional cut of the 2-D reconstruction at $y = 0$ by the (a) switched array, (b) MIMO array and (c) phased array.

imaging method. The focusing points are selected to uniformly cover the imaging area. The number of focusing points is the same as the number of samples the switched array can offer. The sampling rate here is fixed at 100% to see the full potential of all three array configurations. The split augmented lagrangian shrinkage algorithm (SALSA) [7] is adopted as the recovery algorithm.

### 6.3.1 Resolution

Resolution is one of the most important factors of an imaging system. Theoretically, due to the same effective aperture, the aforementioned three array configurations should have approximately the same cross-range resolution while using conventional FT algorithms.

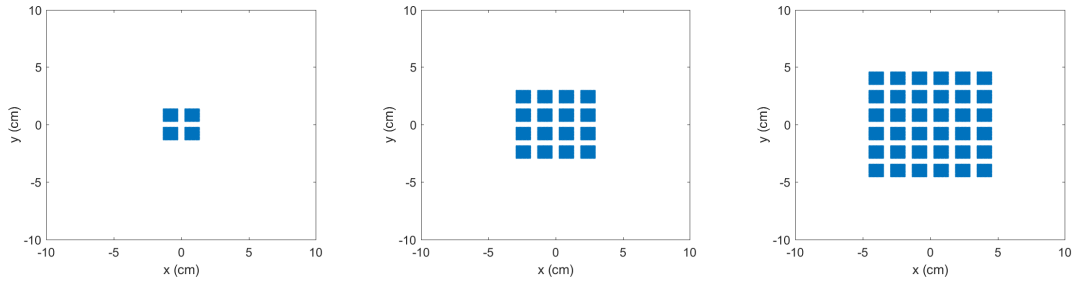


(a) (b) (c)

Figure 6.5: Three sets of target scenes with different level of sparsity. (a) 4 squares, (b) 16 squares and (c) 36 squares with length of 1 cm and spacing of 0.6 cm.

According to (2.9) and (6.6), this cross-range resolution is around $\delta_{x,y} = (1 \times 50)/40 = 1.25$ cm. We first set two point scatterers with spacing of 0.8 cm. Figure 6.3 shows the reconstruction of three methods. All three methods correctly reconstruct the two point scatterers, showing the ability of super-resolution. Figure 6.4 further shows the 1-D cut of the 2-D reconstruction at $y = 0$. Not much difference can be observed as all three curves show similar dip levels. The similar performance between the switched array and the MIMO array is expected as the MIMO array can be considered as a special case of the switched array.

Although the resolution study was presented in previous chapters, the effect of sparsity has been overlooked. The sparsity of the unknown signal plays a critical role in the CS reconstruction. It is well known that a signal with a higher sparsity requires fewer measurements for reconstruction. One would like to know if the sparsity of the target scene can affect the resolution of the CS imaging system. Therefore, we set three sets of target scenes with different level of sparsity, as shown in Figure 6.5. The square targets in all three figures are the same and have a length of 1 cm. The spacings between the squares are fixed at 0.6 cm. Here the sparsity level is adjusted by using different number of squares. Each row of Figure 6.6 presents the image reconstruction of the same target scene by the three array configurations. There is no big difference among the three methods for all three target scenes, suggesting their resolving powers are at the same level.

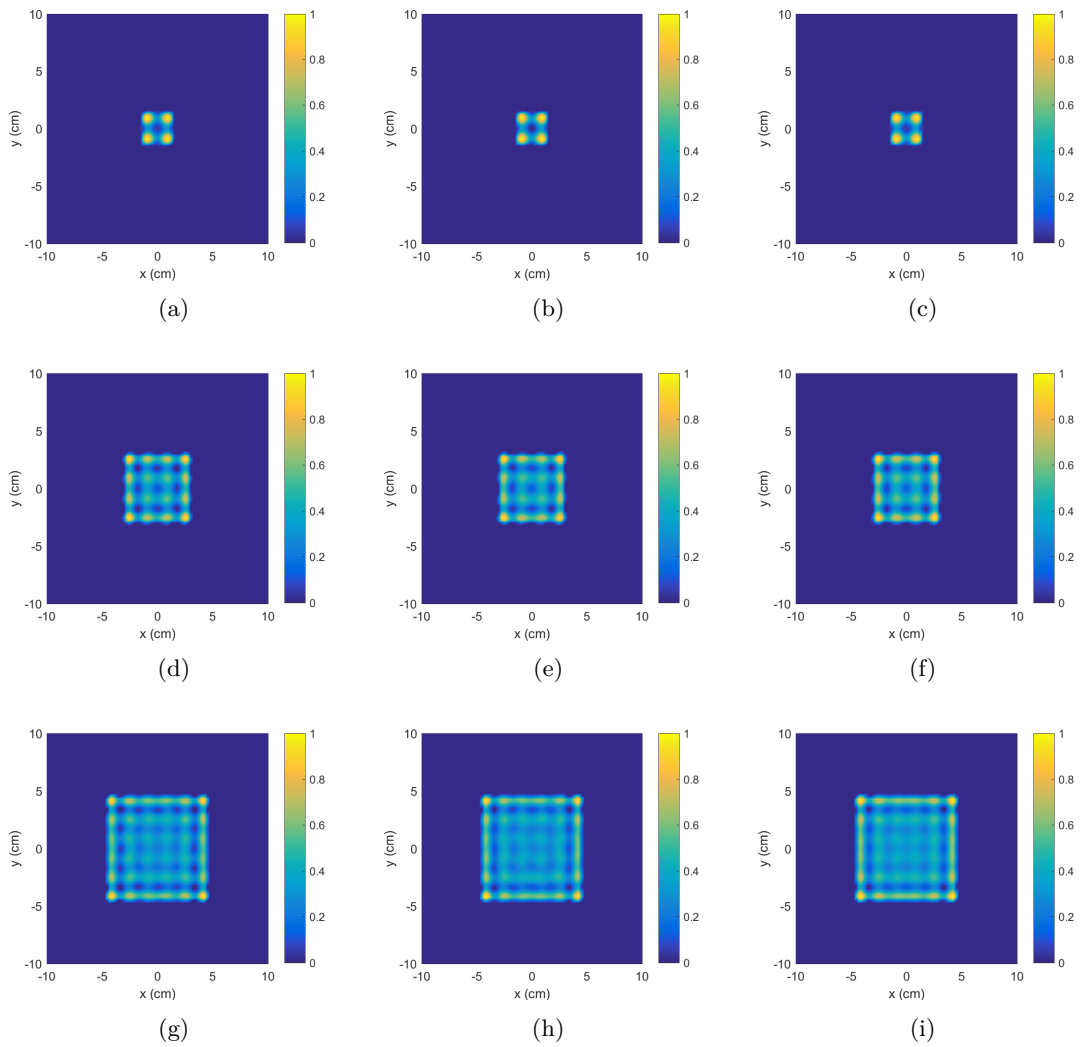


Figure 6.6: Image reconstruction of 4 squares by (a) switched array (b) MIMO array and (c) phased array. Image reconstruction of the 16 squares by (d) switched array (e) MIMO array and (f) phased array. Image reconstruction of 36 squares by (g) switched array (h) MIMO array and (i) phased array.

However, it can be noticed from each column that the reconstruction quality varies. The squares become less distinguishable as the sparsity level decreases. This result indicates the sparsity level of the target scene does affect the resolution to some extent.

As for comparison, we increase the square spacing of the third target scene to the theoretical resolution 1.25 cm. With the true locations of the targets marked as red

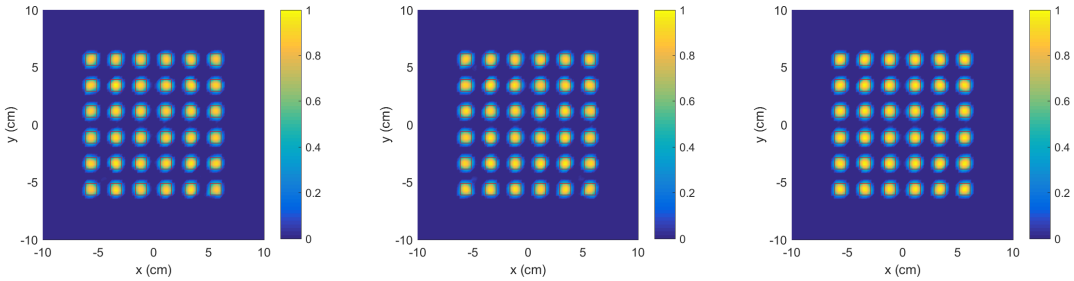


(a) (b) (c)

Figure 6.7: Image reconstruction of 36 squares with 1.2 cm spacing by (a) switched array (b) MIMO array and (c) phased array.

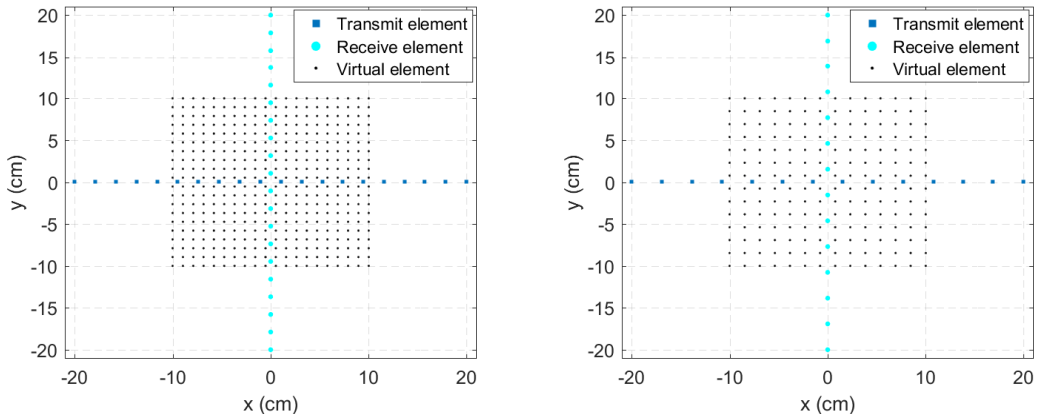


(a) (b)

Figure 6.8: Array topology of the MIMO array with (a) one wavelength spacing in virtual aperture and (b) one and a half wavelength spacing in virtual aperture.

squares for reference, Figure 6.7 demonstrates that the square targets can still be perfectly resolved in all cases, showing the effectiveness of the CS technique.

### 6.3.2 Impact of Element Spacing

As has been shown in Chapter 4, too large element spacing might fail the CS reconstruction. It is interesting to see if the three array configurations have similar performance under sub-Nyquist element spacing. Therefore, we increase the element spacing of the switched array and phased array in the following examples. Two element spacings are

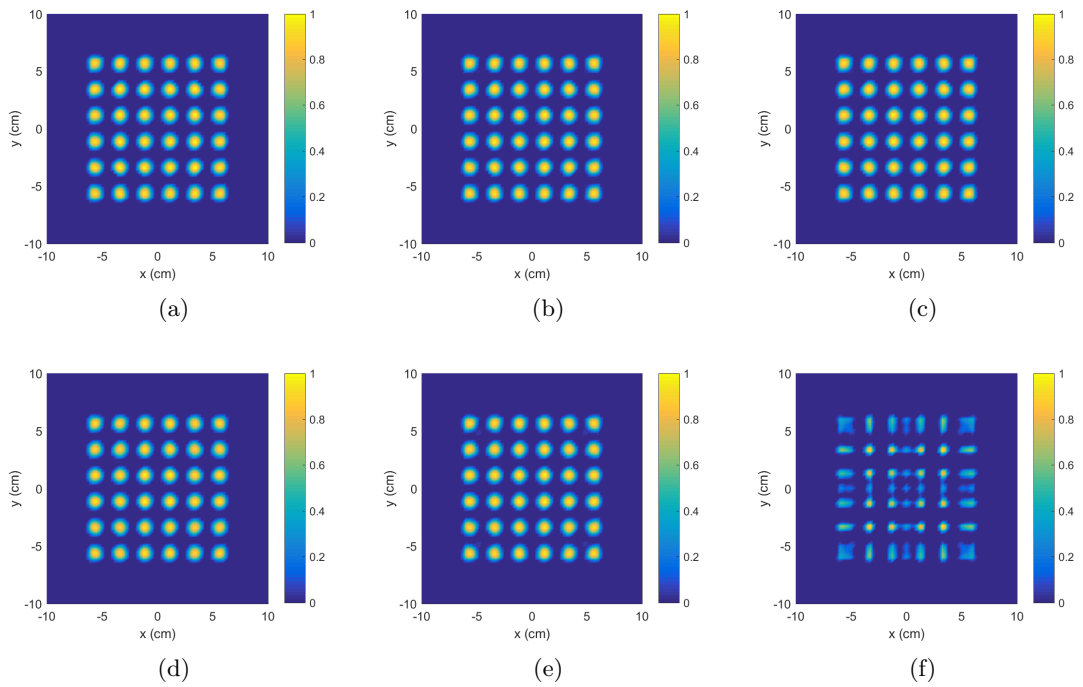


Figure 6.9: Image reconstruction of 36 squares by (a) switched array (b) MIMO array and (c) phased array with one wavelength element spacing. Image reconstruction of 36 squares by (d) switched array (e) MIMO array and (f) phased array with one and a half wavelength element spacing.

adopted: one wavelength and one and a half wavelength. The MIMO array geometries are designed accordingly and are shown in Figure 6.8. The virtual array apertures have $20 \times 20$ elements and $14 \times 14$ elements in the two element spacing configurations, respectively. The MIMO array designs consist of $20 + 20 = 40$ elements and $14 + 14 = 28$ elements, respectively. The same grid of 36 square targets with spacing of 1.25 cm are used as the target scene.

In the one-wavelength example, as shown in the first row of Figure 6.9, all three array configurations correctly reconstruct the target scene as the previous half-wavelength element spacing example. This indicates that the integration of CS technique successfully makes all three imaging systems tolerant to sub-Nyquist element spacing. However, in the one and a half wavelength example, as shown in the second row of Figure 6.9, the phased array configuration fails to reconstruct the target scene while the other two

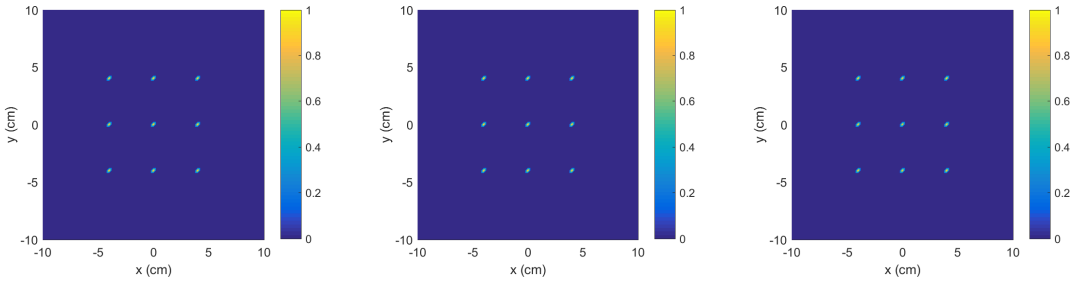


(a) (b) (c)

Figure 6.10: Image reconstruction of 9 point scatterers by (a) switched array (b) MIMO array and (c) phased array with one and a half wavelength element spacing.

configurations still give perfect reconstructions. This result suggests that the switched array and MIMO array are more robust to sub-Nyquist element spacing.

We further test the one and a half wavelength element spacing configuration with a much sparser target scene which has only nine point scatterers. Figure 6.10 shows the corresponding reconstruction results. This time, the phased array configuration gives the correct reconstruction as the switched array and phased array configurations. The difference indicates the minimum required element spacing of the array imaging system is related to the target sparsity, that is, the sparser the target scene is, the less dense the array is required. This property is quite useful as we can design the imaging array with as few antenna as possible if the sparsity level of the target scene can be empirically determined.

### 6.3.3 Robustness against Noise

Apart from system parameters like antenna gain, the SNR of an array imaging system is also related to the number of interrogating modes it can offer. It is well known that noise can be substantially eliminated through averaging. From the information point of view, increasing the number of modes leads to better SNR.

It is easy to understand the number of modes of the switched array scheme is the

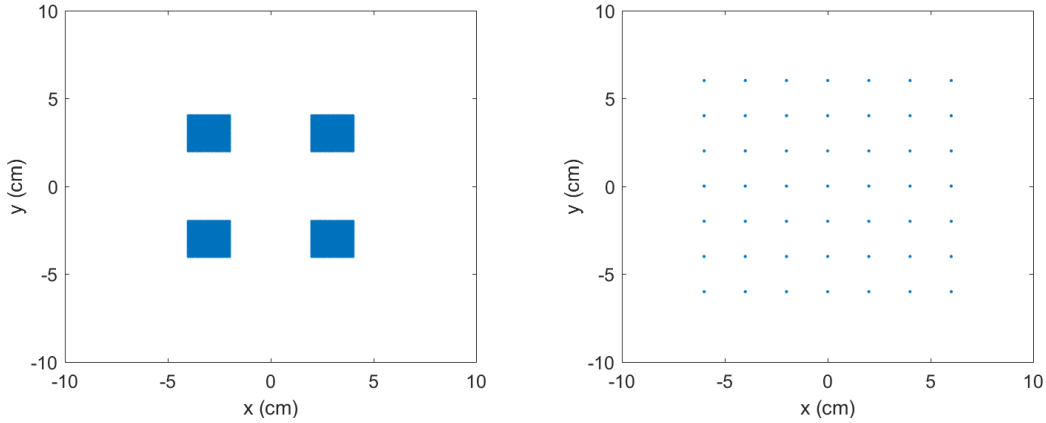


(a) (b)

Figure 6.11: Two sets of target scenes with different level of sparsity. (a) 4 squares and (b) 49 point scatterers.

same as its number of antennas. The MIMO array scheme, as designed to replace the switched array with fewer antennas, has the same number of modes as the switched array scheme. Nevertheless, the MIMO array scheme can easily increase the number of modes by adding a few more transmit and receive antennas. In this regard, the MIMO array has higher potential than the switched array in dealing with noise environment. The phased array scheme, on the other hand, can offer infinite modes since its main beam can be steered towards numerous directions.

We have already shown the phased array is more robust to noise than the switched array in Chapter 5. Here we take the MIMO array into consideration as well. Independent and identically distributed (i.i.d.) Gaussian noise is considered and added to each of the receiving antennas before reconstruction. To make a fair comparison, the same effective aperture, same number of samples and same noise are included. Note that this noise addition is on the condition that all three configurations have the same number of samples.

As previously illustrated, two sets of target scenes with different sparsity levels are tested here. The first target scene, as shown in Figure 6.11(a), consists of four squares with length of 2 cm and spacing of 4 cm. The second target scene, as shown in Figure

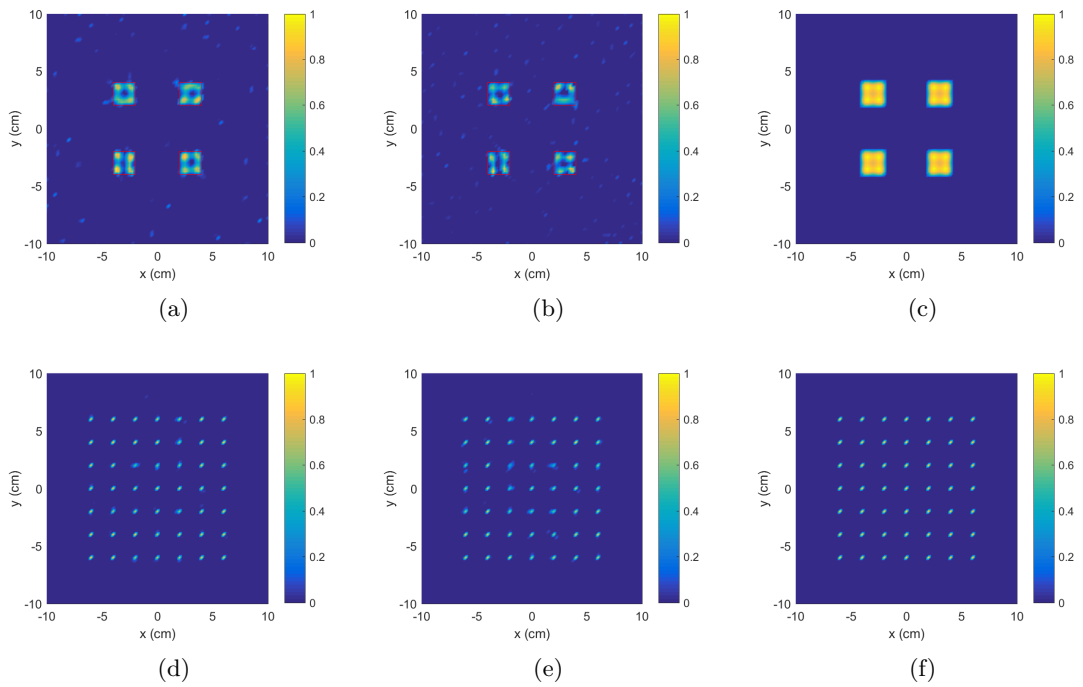


Figure 6.12: Image reconstruction of 4 squares by (a) switched array (b) MIMO array and (c) phased array. Image reconstruction of 49 point scatterers by (d) switched array (e) MIMO array and (f) phased array.

6.11(b), has 49 point scatterers with spacing of 2 cm. Although the phased array is capable of imaging at very low SNR level, the SNR is set as 15 dB here for better comparison. The first row of Figure 6.12 give the reconstruction of the first target scene. While the phased array faithfully reconstruct the four squares, the switched array and MIMO array only show some blurry and unevenly distributed patches in the target area. When compared with the switched array case, there is not much improvement nor degradation can be observed from the MIMO array reconstruction. The second row of Figure 6.12 present the reconstruction of the sparse target scene. The phased array shows a very clean reconstruction as expected. This time, the switched array and MIMO array manage to reconstruct the true locations of the point scatterers, although not perfectly. However, there is still not much difference between the switched array and MIMO array reconstructions.

From the above examples, we can conclude that in the system the MIMO array has similar performance like the switched array when the noise level is the same. The phased array is more robust than other two array configurations in noisy conditions due to its high gain property. Meanwhile, sparsity level can affect the minimum required SNR level for reconstruction, generally a sparse target tends to require lower SNR than a complex target.

### 6.3.4 Computational Complexity

As has been introduced in Chapter 4, the computational complexity of the imaging algorithm can be discussed using both time and space complexity. The space complexity is mainly determined by the system response matrix **H** which has to be stored for computation. Since the number of measurements and grid points is kept the same in all three array configurations for fair comparison, the dimension of the **H** matrix in all cases remain the same, which is to say there is no difference in space complexity. The time complexity mainly consists of the image reconstruction and the construction of the response matrix **H**. The image reconstruction process relies on the response matrix **H** and the CS algorithm used. As the same reconstruction algorithm has been adopted here, the time complexity difference in this process is expected to be small. Therefore, we can conclude that the main computational complexity difference comes from the construction the response matrix **H**.

Table 4-A has shown the computing time and loading time of the response matrix can be problematic when its dimension increases. To make the D-CS method more useful in practical situations, this time complexity has to be reduced as much as possible. Listing 6.1 presents the unoptimized Matlab code of constructing the **H** of the switched array. We can see two for-loops are used to compute the entries of **H** sequentially. However, the for-loop is extremely inefficient and should be totally avoided when the dimension of antenna arrays is high. Another point is the default data type in Matlab is double precision. A complex-valued **H** with double precision can be very large as the dimension

increases. Therefore, these two issues should be solved in the optimized code.

Listing 6.1: Unoptimized code for switched array

```
%========= input parameters ==========
% k: wavenumber
% z0: target to aperture distance
% power: transmit power
% Txy_x & Txy_y: x and y coordinates of the transceiver antennas
% gridxy_x & gridxy_y: x and y coordinates of the grid points
% % ----use traditional for loop --- % %
H=zeros(length(Txy_x),length(gridxy_x));
for i=1:length(Txy_x)                    % loop antenna locations
    for j=1:length(gridxy_x)             % loop grid coordinates
        R=sqrt((gridxy_x(j)-Txy_x(i))^2+(gridxy_y(j)-Txy_y(i))^2+(z0-0)^2);
        H(i,j)=Power*exp(-1i*2*k*R)/(R^2);
    end
end
```

Listing 6.2 gives the optimized code for the **H** construction. Single precision is forced in all the calculations. From our simulations, we can hardly find any difference between single precision based reconstruction and double precision based reconstruction. The use of for-loop is avoided by using the bsxfun function which supports element-wise operation. The reason the bsxfun is faster is because the element-wise operation is actually doing a multithreaded caculation of the **H**.

Listing 6.2: Optimized code for switched array

```
% % ----use bsxfun for fast computation --- % %
R=sqrt((bsxfun(@minus,gridxy_x.',Txy_x)).^2+(bsxfun(@minus,
    gridxy_y.',Txy_y)).^2+(z0-0)^2);
H=Power*exp(-1i*2*k*R)./(R.^2);
```

To verify the effectiveness of the optimized code, we evaluate the two codes with different array configurations and target discretizations. Suppose the number of samples is $M^2$ and the number of grid points is $N^2$. Table 6-A shows the complexity comparison of the unoptimized and optimized codes. It can be noticed the optimized code achieves better efficiency than the unoptimized one in all three cases. The space required to save the **H** matrix is only half of the unoptimized one due to the single precision adopted. More importantly, the improvement becomes more pronounced as the **H** gets bigger. Note that results shown here are a little different from the results in 4-A. This is because we used a desktop computer with an Intel i7-4770 @3.40 GHz and 16 GB memory. The Matlab version is R2016a (x64) and was installed on a Windows 7 operating system.

Table 6-A: Complexity Comparison of the Unoptimized Code and the Optimized Code

| Configuration | Unoptimized Code | | Optimized Code | |
|---|---|---|---|---|
| | Computing (s) | Storage | Computing (s) | Storage |
| $M = 40$, $N = 81$ | 4.09 | 148 MB | 0.30 | 70 MB |
| $M = 40$, $N = 121$ | 9.18 | 321 MB | 0.64 | 152 MB |
| $M = 80$, $N = 121$ | 37.06 | 1.32 GB | 2.80 | 638 MB |

In the process of constructing the **H** matrix, the MIMO array scheme needs to calculate $R_{\mathrm{Tx}}$ and $R_{\mathrm{Rx}}$ while they are equivalent in the switched array case. Therefore, the complexity of the MIMO array method is higher than that of the switched array method. Listing 6.3 shows the **H** construction code for the MIMO array. The phased array, on the other hand, is more complicated than the switched array and MIMO array. This is because, for each interrogating mode, all antennas are involved in calculating

the beamforming signal, making the use of for-loop difficult to avoid. Nevertheless, the Parallel Computing Toolbox™ can be used to speed up the calculation.

Listing 6.3: Optimized code for MIMO array

```
% % ----H reonstruction for MIMO array --- % %
R_tx=sqrt((bsxfun(@minus,gridxy_x.',Txy_x)).^2+(bsxfun(@
    minus,gridxy_y.',Txy_y)).^2+(z0-0)^2);
R_rx=sqrt((bsxfun(@minus,gridxy_x.',Rxy_x)).^2+(bsxfun(@
    minus,gridxy_y.',Rxy_y)).^2+(z0-0)^2);
H=Power*exp(-1i*k*(R_tx+R_rx))./(R_tx.*R_rx);
```

Table 6-B shows the complexity comparison of the three array configurations. It can be noticed the switched array scheme is the most efficient one. The MIMO array scheme is slightly worse than the switched scheme. However, the phased array scheme takes too much time in calculating the **H** matrix, making it unsuitable for real-time imaging at the moment.

Table 6-B: Computing Time of the **H** matrix

| Configuration | Switched array | MIMO array | Phased array |
|---|---|---|---|
| $M = 20$, $N = 41$ | 0.03 s | 0.06 s | 181 s |
| $M = 30$, $N = 61$ | 0.12 s | 0.29 s | 160 m |
| $M = 40$, $N = 81$ | 0.30 s | 0.85 s | 1559 m |

## 6.4 Summary

This chapter first introduces the theory of MIMO array design and then gives the formulation of compressive MIMO array imaging. The performance of the three array configurations are studied in detail in the rest of this chapter, considering parameters such as resolution, effects of element spacing, robustness against noise and computational complexity. Generally, the MIMO array achieves comparable performance as the

switched array with far fewer antennas. The phased array has much better robustness against noise environment than other two array configurations but suffer from higher computational complexity. The switched array and MIMO array are more stable than the phased array when the arrays have sub-Nyquist element spacing. The resolving powers of all three array configurations are basically the same and the sparsity level of the target scene can slightly affect the resolving power of the system. Finally, we discussed the computational complexity and made some efforts in improving the efficiency of the code.

## References

[1] X. Zhuge and A. G. Yarovoy, "Study on two-dimensional sparse mimo uwb arrays for high resolution near-field imaging," *IEEE Transactions on Antennas and Propagation*, vol. 60, no. 9, pp. 4173–4182, 2012.

[2] G. Lookwood and F. S. Foster, "Optimizing the radiation pattern of sparse periodic two-dimensional arrays," *IEEE transactions on ultrasonics, ferroelectrics, and frequency control*, vol. 43, no. 1, pp. 15–19, 1996.

[3] C. Cooley and B. Robinson, "Synthetic focus imaging using partial datasets," in *1994 IEEE Ultrasonics Symposium*, vol. 3. IEEE, 1994, pp. 1539–1542.

[4] X. Zhuge, "Short-range ultra-wdieband imaging with multiple-input multiple-output arrays," Ph.D. dissertation, Delft University of Technology, Delft, November 2010.

[5] Y.-C. Yang, "Uwb antennas and mimo antenna arrays development for near-field imaging," Ph.D. dissertation, Delft University of Technology, Delft, October 2011.

[6] X. Zhuge and A. G. Yarovoy, "Three-dimensional near-field MIMO array imaging using range migration techniques," *IEEE Transactions on Image Processing*, vol. 21, no. 6, pp. 3026–3033, June 2012.

[7] M. V. Afonso, J. M. Bioucas-Dias, and M. A. Figueiredo, "Split augmented lagrangian shrinkage algorithm," http://cascais.lx.it.pt/~mafonso/salsa.html, 2010.

# Chapter 7

# Compressive Luneburg Lens Imaging

## 7.1 Introduction

Phased array technology is a common way to generate high gain and steerable beams. The capability of dynamic control of the radiation pattern makes the phased array crucial in communication systems and military radars. The disadvantage of phased arrays, however, is their large hardware footprint, as each array element needs to be connected to a dedicated transceiver module leading to very high implementation cost. Reflector antennas are popular alternatives for high-directivity and beam steering purposes. This type of antenna has been successfully introduced to many security imaging systems [1–3]. Although reflector antenna systems are more cost effective than the phased array systems, they usually require a bulky mechanical scanning system which suffers from scanning speed.

Lens antennas are similar to reflector antennas in transforming spherical wave-fronts emitted from a feed at their focus into plane wave-fronts. A variety of lens antenna applications can be found in literature [4–6], ranging from wireless communication to

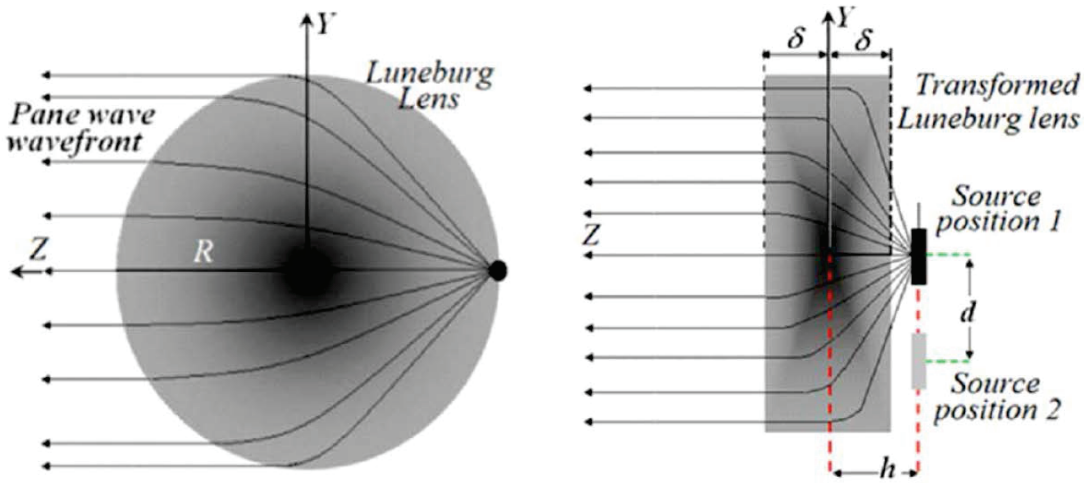


(a) (b)

Figure 7.1: Ray tracing for (a) original and (b) transformed Luneburg lens [12].

radar imaging. Among many existing lenses, the main two categories are homogeneous dielectric lenses [7] and gradient-index lenses [8–10]. Luneburg lens belongs to the latter one and is famous for its intrinsic broadband response and ability to form multiple beams [10]. Its spherical symmetric property makes it suitable for electronic beam scanning by placing sources at different locations and frequency points. In this chapter, we introduce a beam steering imaging system using a compact 3-D flat Luneburg lens antenna. Image reconstruction is realized by using CS techniques [11]. The adoption of Luneburg lens avoids the use of phased array components and thus provides a relatively low-cost and straightforward imaging solution.

## 7.2 Luneburg Lens Design

An ideal Luneburg lens is a dielectric sphere whose index of refraction varies with the radius of the sphere [10]:

$$n(r) = \sqrt{2 - r^2}, \tag{7.1}$$

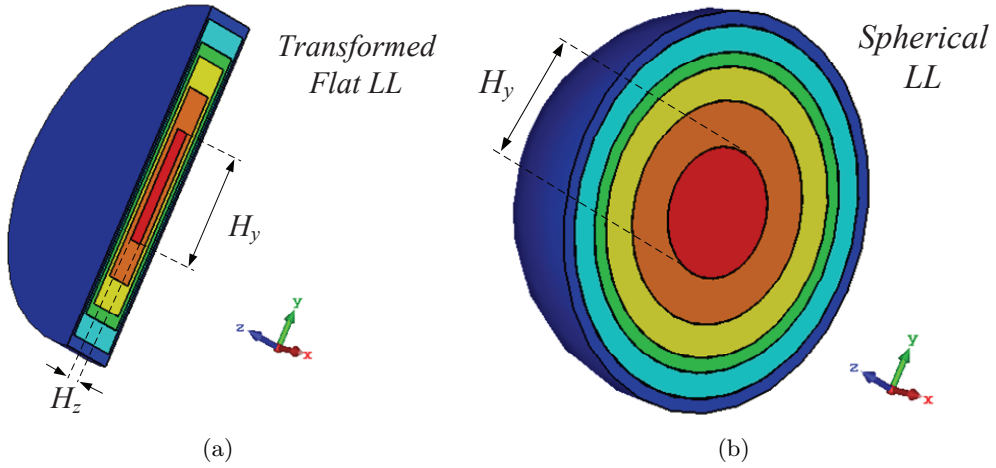


Figure 7.2: Cross-section of the discretized flat Luneburg lens and spherical Luneburg lens after considering 6 shells of dielectric material with the optimised dimensions as in Table I.

where $r$ is the normalized radial position. With such a permittivity distribution, the Luneberg lens is able to focus an incoming wave into a focal point on the boundary of the sphere which is opposite of the entry point. In the same way, the spherical wave of a radiator at the focal point can be transformed into plane waves, as illustrated in Figure 7.1(a) [12].

In practice, it is extremely difficult to manufacture such a lens with continuous permittivity variation. The most common way is to approximate the gradient index law by using a finite number of concentric homogeneous dielectric shells [13], which is then to choose the thickness and permittivity of each shell such that the lens can achieve the maximum directivity. A lot of algorithms are available for such optimization problems [9, 14]. One drawback of the spherical Luneburg lens is that its spherical surface is incompatible with planar feeds or detector arrays. In recent years, the development of transformation optics (TO) theory [15] provides a means to modify the traditional Luneburg lens by flattening the spherical surface while maintaining similar properties to the original spherical lens [12, 16–18].

In the TO design of flat Luneburg lens, the first step is the coordinates transformation

which tries to 'squeeze' the original sphere into a flat cylinder. Suppose the refactive index of the original Luneburg lens is a function of the spatial coordinates $y$ and $z$. The coordinates of the transformed flat Luneburg lens as shown in Figure 7.1(b) can be expressed as

$$z' = \frac{\delta}{\sqrt{R^2 - y^2}} z, \; y' = y, \tag{7.2}$$

where $\delta$ represents the compression of the original Luneburg lens and $R$ is the radius. After the geometry of the flat lens has been determined, its refractive index can then be calculated accordingly. The new values of the permittivity and permeability tensors are given by

$$\begin{aligned} \bar{\bar{\varepsilon}}' &= \left(2 - \frac{(R^2 - y'^2)z'^2 + (\delta y')^2}{(\delta R)^2}\right) \cdot |\sqrt{R^2 - y'^2}| \cdot \begin{pmatrix} A & B \\ B & \frac{1}{\delta} \end{pmatrix} \\ \bar{\bar{\mu}}' &= |\sqrt{R^2 - y'^2}| \cdot \begin{pmatrix} A & B \\ B & \frac{1}{\delta} \end{pmatrix} \end{aligned} \tag{7.3}$$

where the coefficients $A$ and $B$ are expressed as

$$A = \frac{\delta(R^2 - y'^2) + \delta z'^2 y'^2}{(R^2 - y'^2)^3}, \; B = \frac{z'y'}{|\sqrt{R^2 - y'^2}|(R^2 - y'^2)}. \tag{7.4}$$

More details of the selection of $\delta$ can be found in [12].

Figure 7.2 gives an example of flat Luneburg lens design using TO [12]. The original spherical Luneburg lens consists of 6 shells with the optimized dimensions and permittivities shown in right column of Table 7-A. The parameters of the transformed flat Luneburg lens are shown in the left column of Table 7-A. With the reduced size and a flat surface, the new lens is easier for practical feeding implementation. For example, planar mechanic scanning can be adopted for single feeding system while completely electronic scanning can be achieved using a feeding array. According to [12], when fed by an X-band pyramid horn antenna, the flat Luneburg lens is able to preserve similar directivity performance to the original spherical Luneburg lens. The maximum scanning angle of this flat Luneburg lens is around 30° when the horn is placed 30 mm away from

Table 7-A: Flat Luneburg Lens Transformed from a Spherical Lunebrug Lens

| Cylinder | $H_z$ (mm) | $H_y$ (mm) | $\varepsilon_r$ |
|---|---|---|---|
| 1 | 3.32 | 31.2 | 12 |
| 2 | 6.62 | 53.2 | 10 |
| 3 | 8.8 | 69.7 | 8 |
| 4 | 11 | 76.5 | 6 |
| 5 | 12.4 | 89.1 | 4 |
| 6 | 13.8 | 95.4 | 2 |

| Sphere | $H_y$ (mm) | $\varepsilon_r$ |
|---|---|---|
| 1 | 31.4 | 2 |
| 2 | 53.5 | 1.8 |
| 3 | 69.8 | 1.6 |
| 4 | 76.9 | 1.4 |
| 5 | 89.3 | 1.2 |
| 6 | 95.9 | 1.08 |

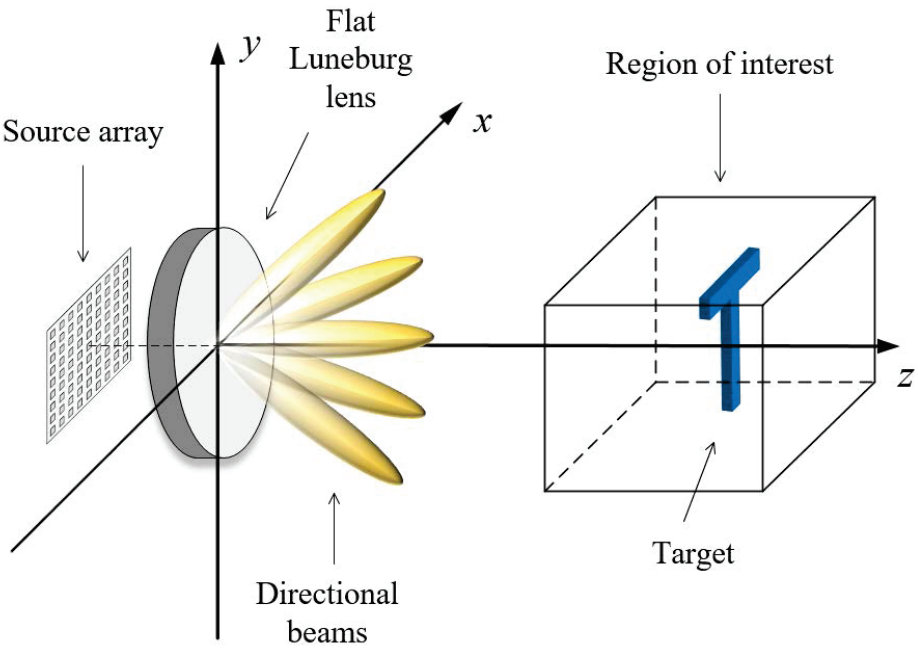


Figure 7.3: Compressive sensing based Luneburg lens imaging system.

the center of the lens. This steering angle is mainly limited by the physical size of the flat Luneburg lens. Higher steering angles can be obtained by increasing the longitudinal size of the lens ($x$- and $y$-dimension) and the appropriate discretization.

## 7.3 Compressive Luneburg Lens Imaging Formulation

The proposed Luneburg lens imaging system is shown in Figure 7.3. An array of feeding elements is placed at the focal plane of the flat Luneburg lens for illumination. By sequentially exciting each element, the Luneburg lens produces beams pointing at differ-

ent directions. The imaging process is similar to a phased array imaging system. Antenna beams are first steered to scan the region of interest for data acquisition. The stored data is then used for image reconstruction. In this way, we realize a beam steering imaging system without using expensive phased array components. Another advantage of the Luneburg imaging system is its multi-beam capability enables fast electronic scanning for real-time imaging applications.

In order to reconstruct the target scene from the measurements, the forward imaging model should be derived first. Under the BA, the scattered electric field at the antenna can be expressed as

$$\mathbf{E}_s(\mathbf{r}, k) = k^2 \int_V \mathbf{G}(\mathbf{r}, \mathbf{r}', k)\mathbf{E}_{inc}(\mathbf{r}', k)\chi(\mathbf{r}')\, d\mathbf{r}', \tag{7.5}$$

where $\mathbf{r}$ is the source position, $k$ is the wavenumber in free space and $\chi(\mathbf{r}')$ is the well known contrast function. $\mathbf{G}(\mathbf{r}, \mathbf{r}', k)$ is the Green's function and $\mathbf{E}_{inc}(\mathbf{r}', k)$ is the incident field at the target position $\mathbf{r}'$. From the reciprocity principle, the Green's function here is the same as the incident field. Therefore, (7.5) can be simplified into [19]

$$\mathbf{E}_s(\mathbf{r}, k) = \int_V \mathbf{E}_{inc}^2(\mathbf{r}', k)\ \left[k_s^2(\mathbf{r}') - k_b^2\right]\ d\mathbf{r}', \tag{7.6}$$

where $k_s$ and $k_b$ are the wavenumbers of the target and the background medium, respectively. In radar imaging, the contrast function is usually replaced with a more straightforward reflectivity function for simplicity. To recover the target scene from the scattered field data, traditional methods try to reformulate the integral of equation (7.6) into FT form such that the inverse FT can be applied for image reconstruction. However, this integral reformulation usually requires approximations and thus the solution is not accurate.

CS is a powerful signal processing technique from the information theory society [11]. CS theory enables signal reconstruction from highly under-sampled data provided the signal is sparse and proper sensing matrix is adopted. This technique has been

successfully applied in previous chapters and was shown to give better imaging results than traditional methods. In a similar way, equation (7.6) can be accurately solved by rewriting it in the CS framework as

$$\mathbf{s} = \mathbf{H}\mathbf{g} + \mathbf{n}, \tag{7.7}$$

where $\mathbf{s}$ is a vector of the scatter field data received at different source locations, $\mathbf{g}$ is a vector of reflectivity coefficients of the target scene, $\mathbf{H}$ is the system response matrix, and $\mathbf{n}$ is the noise vector. Frequency and spatial under-sampling can be applied by multiplying an under-sampling operator $\mathbf{A}$ as

$$\mathbf{y} = \mathbf{A}\mathbf{H}\mathbf{g} + \mathbf{n}', \tag{7.8}$$

where $y$ is the under-sampled data and $n'$ has the same dimension as $y$. This underdetermined system is usually solved by rewriting it as the well known BPDN [20]

$$\min_{\mathbf{g}} \|\mathbf{g}\|_1 \quad s.t. \quad \|\mathbf{A}\mathbf{H}\mathbf{g} - \mathbf{y}\|_2^2 \leq \epsilon, \tag{7.9}$$

where $\epsilon$ is a nonnegative real parameter that defines the noise level. The $\ell_1$ norm is suitable for most sparse target scenes. Other sparsifying transformations like TV can also be used depending on the types of the target scene.

The critical step of this compressive imaging approach is to calculate the response matrix $\mathbf{H}$ from equation (7.6). While it is easy to calculate the electric field from formulas in traditional array imaging, the Luneburg lens imaging system does not have a straightforward solution. One possible way is to use geometrical optics (GO) or physical optics (PO) principals, which are commonly used in lens antenna optimizations and synthesis [14]. However, these methods are approximated in nature and made a compromise between calculation time and accuracy. Another way is to use simulated or measured radiation patterns for electric field calculation. This way gives better accuracy at the cost of time consuming full-wave simulation or real pattern measurements. Once the

radiation pattern of the lens antenna is known, the incident field in equation (7.6) can be calculated according to [19]

$$\mathbf{E}_{inc}^{2}(\mathbf{r}', k) \approx 2\eta P(\phi, \theta, k) \exp(-j2kr) \tag{7.10}$$

where $(r, \theta, \phi)$ is the spherical coordinates of the target position $\mathbf{r}'$ and $P(\phi, \theta, k)$ is the phaseless radiation pattern of the antenna at given angles.

There are many commercial available EM solvers can be used for the radiation pattern simulation, e.g., FEKO, ANSYS HFSS, CST Microwave Studio, etc. Among these solvers, CST offers higher degree of freedom in dealing with the field data. For example, the simulated far-fields in CST can be saved as directivity, gain, realized gain, E-field, E-pattern and so on. To obtain several hundred radiation patterns one by one is a very time-consuming task. One would like to set-up the simulation such that the horn antenna can automatically scan all positions and also save the corresponding radiation patterns. Parameter Sweep is such a built-in function in CST which can be used for controlling the translation of the horn antenna in the focal plane. However, according to our tests, this method suffers from two major issues. Firstly, it is inconvenient to keep track of the progress of the simulation. Once the simulation is interrupted, it is cumbersome to start from where it left off. This inconvenience makes the direct parameter sweep approach quite vulnerable to unexpected situations like software crash and power failure. Secondly, the CST software becomes very slow as the parameter sweep approaches the end. The normally 10 minutes per parameter simulation can take up to hours to finish. When this happens, the PC also becomes extremely slow and sometimes nonresponsive. While the software crash issue is quite often uncontrollable, we decided not to use this direct parameter sweep approach.

Another way is to use the more advanced Macro Programming function in CST. CST already offered many built-in Project Templates that are written in the VBA programming language. One can modify these existing examples to extend the program's

capabilities. Although it is possible to only use VBA programming to solve the aforementioned simulation issues, the VBA language is not a good candidate for data processing. Fortunately, the Component Object Model (COM) support makes it possible to control CST using many other applications. For instance, Matlab can be used for more efficient data processing in our case. We present the code used for radiation pattern generation in the Appendix B. The main work of the parameter sweep is done in the Matlab code shown in Appendix B.1. At each step, Matlab invokes the CST application and updates the parameters for the translation of the horn antenna. The CST solver is then called by using system commands to execute a simple VBA code as shown in Appendix B.2. After the simulation, radiation pattern data is extracted, saved and moved to a specified location. The progress of the parameter sweep is well monitored using the for-loop. When software crash happens, we can easily start again by just changing the start number of the for-loop. After all radiation patterns have been obtained, a final Matlab code shown in Appendix B.3 is used to read the radiation pattern files and save them into one single Matlab data file for further use.

## 7.4 Numerical Analysis

This section presents some numerical examples to verify the proposed imaging system. The flat Luneburg lens shown in Section 7.2 is adopted for simulation. We choose the radiation pattern approach for response matrix construction. A sketch of the imaging system is shown in Figure 7.4. The Luneburg lens with a moving horn antenna at the focal plane are simulated in CST Microwave Studio to get the radiation patterns. Then the system response matrix and synthetic data are calculated using these radiation patterns in Matlab. The dimensions of the pyramid horn antenna are shown in Figure 7.5(a) together with its radiation pattern in Figure 7.5(b). The S-parameter of this pyramid horn antenna is shown in Figure 7.6. Although not optimized, the S-parameter of the horn antenna is still well under -15 dB from 7 GHz to 13 GHz. To give a glimpse of

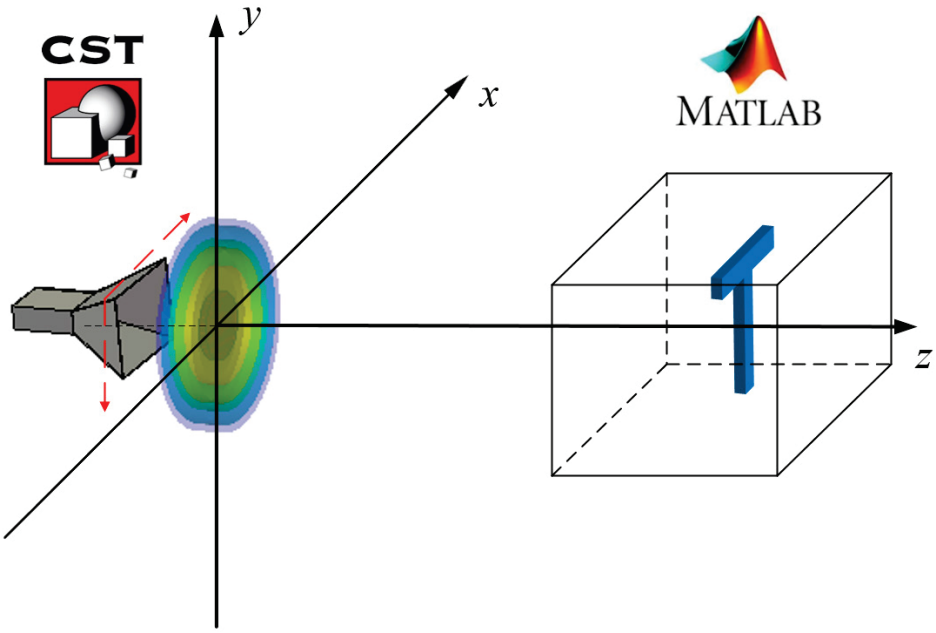


Figure 7.4: Luneburg lens imaging system using a mechanically scanned horn antenna.

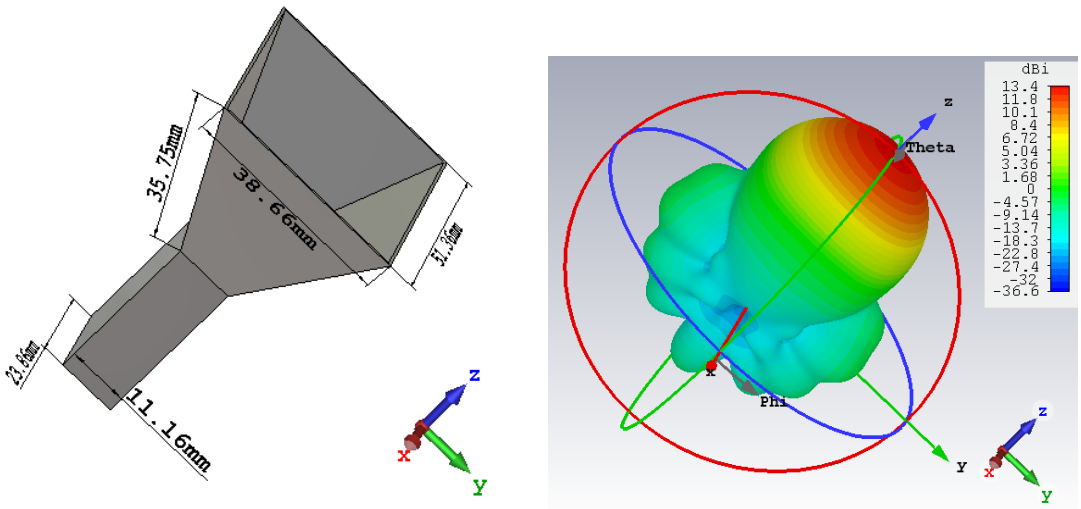


(a) (b)

Figure 7.5: (a) Dimensions of the pyramid horn antenna and (b) its radiation pattern.

the beam steering performance of the Luneburg lens antenna, a set of radiation patterns are given in Figure 7.7 when the lens is fed at different locations in the focal plane. The maximum has been achieved when the horn is placed at the center of the focal plane,

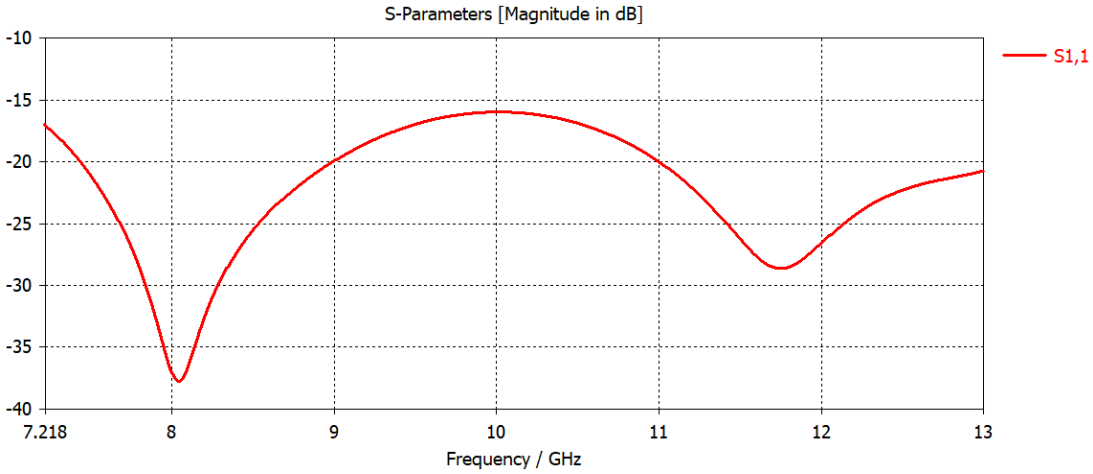


Figure 7.6: S-parameter of the pyramid horn antenna.

which is about 5 dB higher than the original horn antenna, showing the effectiveness of the Luneburg lens in gain enhancement. When the feeding location is moving along the $x$ axis, the main beam of the lens antenna gradually moves towards the reverse direction, just in the same way as the spherical lens.

We first assume a total of 30 $\times$ 30 source locations are used for data acquisition. The 900 feeding locations are uniformly distributed in a 30 mm $\times$ 30 mm area in the focal plane. The 20 cm $\times$ 20 cm ROI which is 30 cm away from the lens is discretized into 81 $\times$ 81 pixels. Single frequency signal at 10 GHz is considered for cross-range imaging only. In the algorithm implementation, we adopt the split augmented lagrangian shrinkage algorithm (SALSA) [21] for image reconstruction. Four rectangular stripes as shown in Figure 7.8(a) are considered as targets for test. A total of 450 random samples from the 900 samples (50% sampling rate) are used for image reconstruction. Figure 7.8(b) presents the imaging result of the proposed imaging system using CS algorithm. Although the reconstruction is not perfect, the four stripe targets can still be easily distinguished. This example shows the feasibility of the imaging system using 30 $\times$ 30 mechanically scanned positions. However, mechanic scanning of 900 points is going to take too much time and thus is not desirable for real-time applications. The ultimate goal is to have a completely electronic scanning system that can finish data acquisition

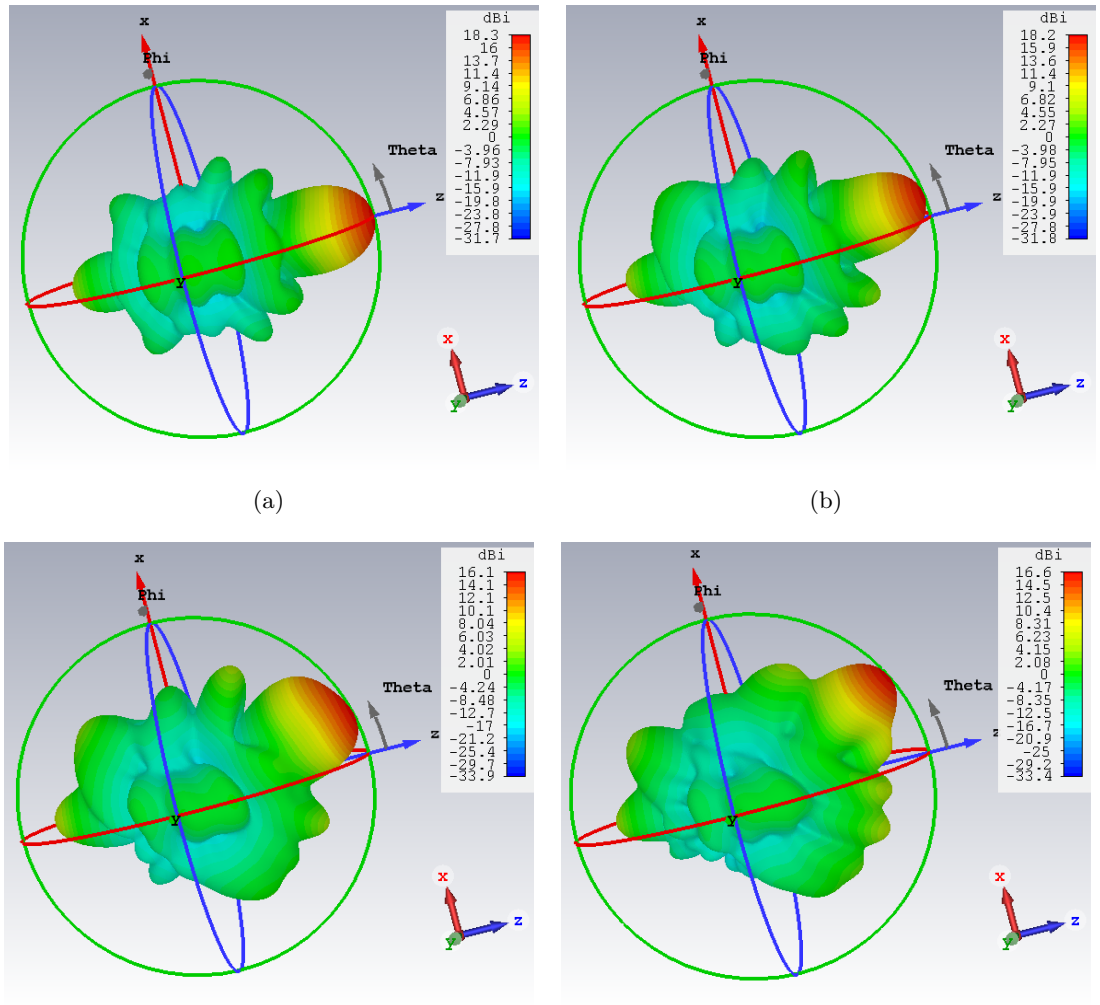


Figure 7.7: Three-dimensional far-field directivity patterns at 10 GHz for different positions of the horn, (a) at 0, (b) 10, (c) 20 and (d) 30 mm along the $x$ axis.

in a very short time. In our example, a feeding array of 30 × 30 elements is required to achieve 900 samples. In reality, it is almost impossible to fabricate such an array within a 9.5 cm × 9.5 cm aperture while the wavelength is 3 cm, let alone the actual feeding region is smaller than the lens aperture. Therefore, a larger lens is needed to fit in a feeding array that has normal element spacing.

While simulating an electric large lens with hundreds of radiation patterns will cost too much time, another way to alleviate the limited space issue is to increase the element

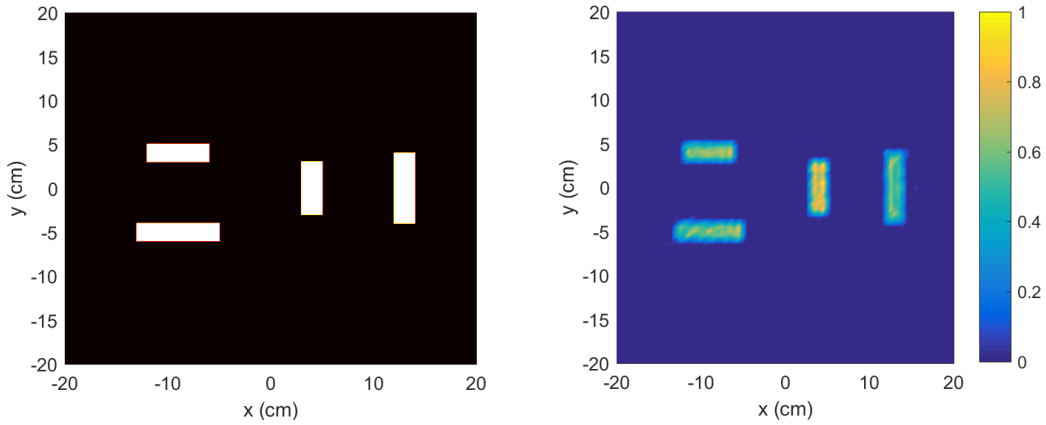


(a) (b)

Figure 7.8: Image reconstruction of four stripe targets using 50% random samples. (a) The ground truth and (b) reconstruction by the proposed imaging method.

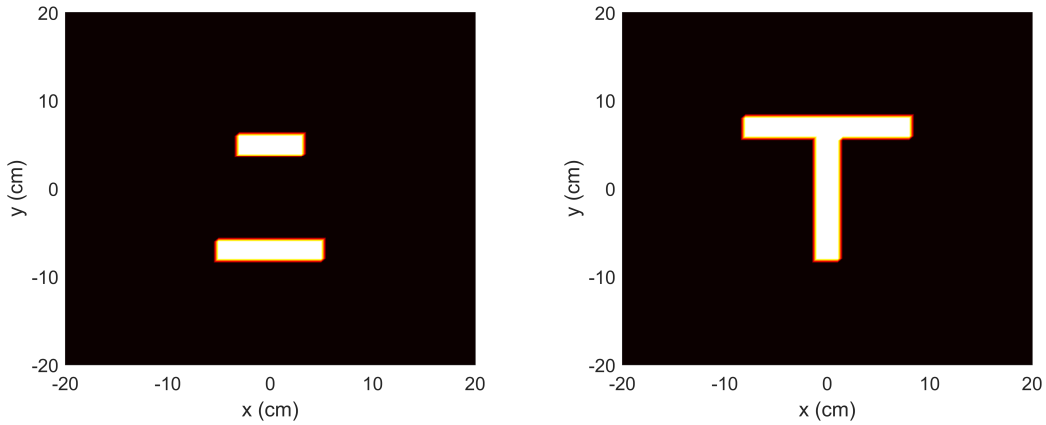


(a) (b)

Figure 7.9: Ground truth of the (a) rectangular stripe target and (b) T-shaped target.

spacing of the feeding array. Recall that the previous chapter has shown the compressive array imaging is capable of dealing with sub-Nyquist element spacing, we expect to see the same feature in compressive Luneburg lens imaging. Therefore, another two configurations with $20 \times 20$ and $12 \times 12$ feeding locations are considered, together with 400 and 144 newly generated radiation patterns, respectively. These two configurations are then compared with the original one in the following two scenarios.

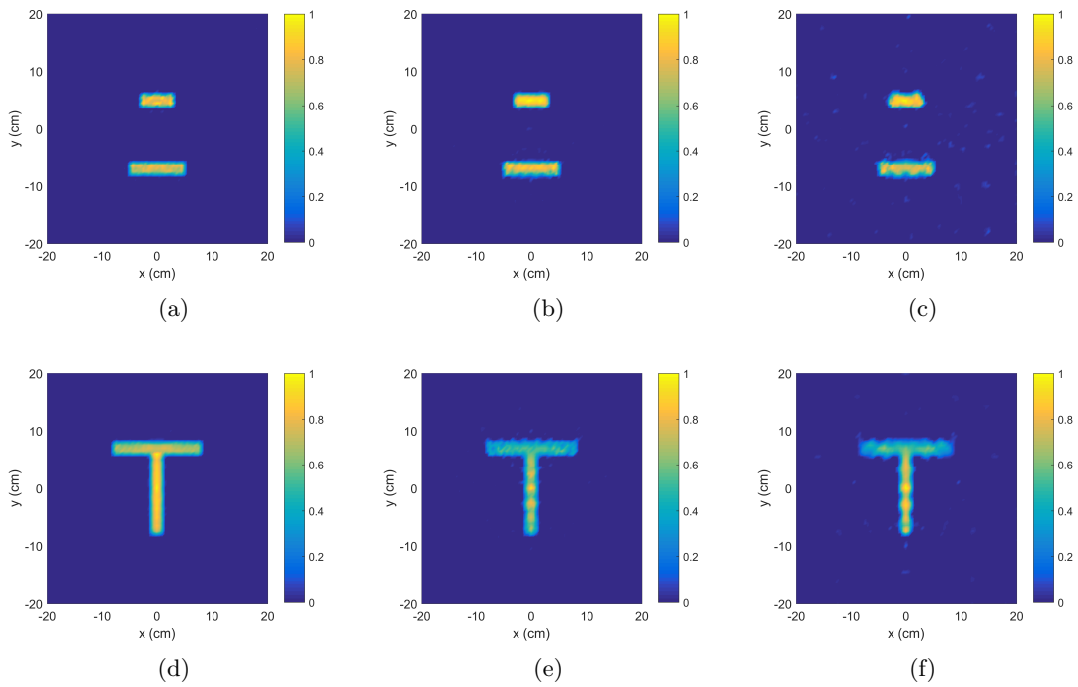


Figure 7.10: Stripe target reconstruction with (a) 30 × 30, (b) 20 × 20 and (c) 12 × 12 feeding locations. T-shaped target reconstruction with (a) 30 × 30, (b) 20 × 20 and (c) 12 × 12 feeding locations.

In the first scenario, two complex target scenes are used, with one scene as rectangular stripes and the other as a T-shaped target. The ground truths of the two target scenes are shown in Figure 7.9(a) and Figure 7.9(b), respectively. The first, second and third columns of Figure 7.10 represent the reconstructions of the 30 × 30, 20 × 20 and 12 × 12 feeding configurations, respectively. We can notice that the 30 × 30 configuration gives the most faithfully reconstruction of the target scenes. As the element spacing increases, the image quality decreases. Specifically, the contours of the reconstructed targets are no longer smooth and thus makes the overall image blurry. Moreover, speckles also start to show up in the background. Nevertheless, the 12 × 12 configuration is still able to offer a discernible reconstruction of the targets scenes. The reconstruction comparison suggests that increasing the element spacing is a possible way to alleviate the array fabrication issue at the cost of deteriorating some image quality.

To better understand this compromised approach, resolution test is considered in our

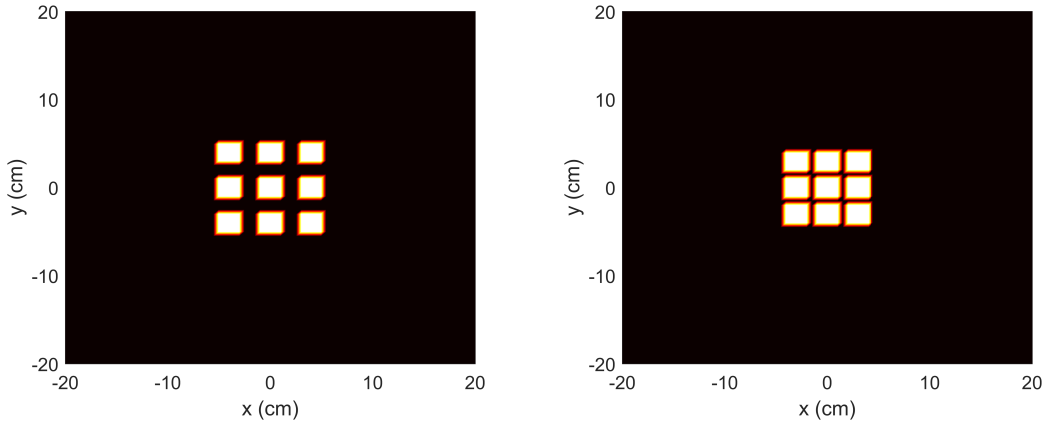


(a) (b)

Figure 7.11: Ground truth of the 9 square target with (a) 2 cm spacing and (b) 1 cm spacing.

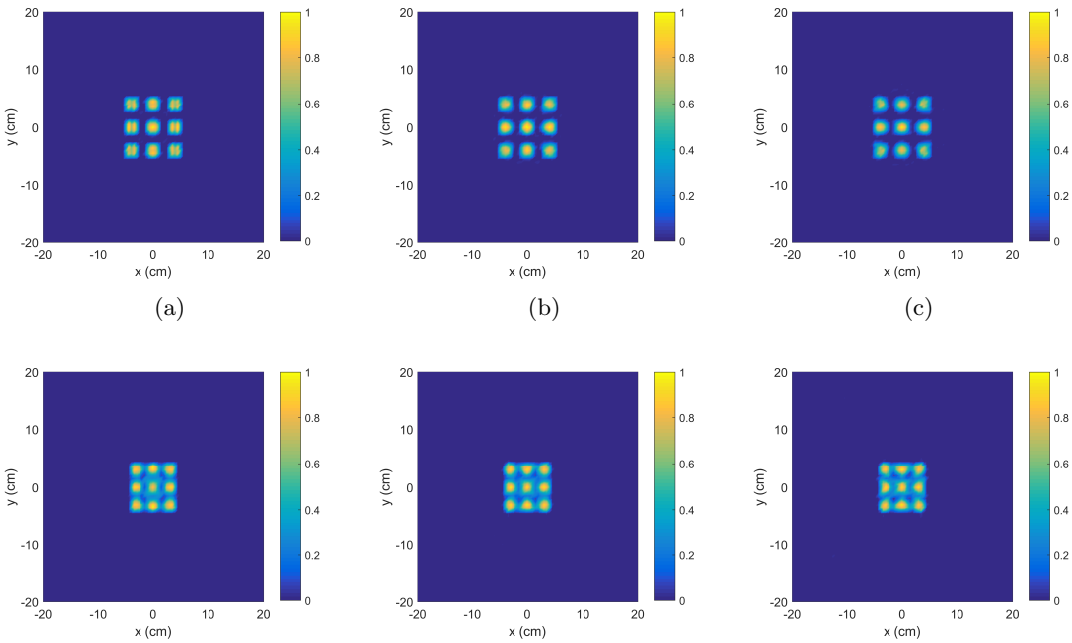


(a) (b) (c)

(d) (e) (f)

Figure 7.12: Reconstruction of 2 cm spaced square targets using (a) 30 × 30, (b) 20 × 20 and (c) 12 × 12 feeding locations. Reconstruction of 1 cm spaced square targets using (a) 30 × 30, (b) 20 × 20 and (c) 12 × 12 feeding locations.

second scenario. As has been shown in Chapter 6, the resolution of compressive imaging is related to the target sparsity. The resolution of two point scatterers is not accurate

enough to represent the resolution of the system. Therefore, solid square targets with varying spacings are employed in this case. Two sets of 9 solid squares with one 1 cm spaced and the other 2 cm spaced, as shown in Figure 7.11, are simulated. According to the general resolution calculating formula, the 9.5 cm $\times$ 9.5 cm aperture gives a resolution of 4.7 cm at 30 cm distance using 10 GHz signals. One can imagine, with traditional FT algorithms, the 9 squares in both target scenes can hardly be distinguished. However, we expect to see better results with our CS methods. The reconstruction results of the three configurations are shown in different columns in Figure 7.12. Image quality deterioration can also be observed in the reconstructed squares just as the previous example. Additionally, when the spacing of the squares is 2 cm, the gaps between the squares are all clear to see in all three figures. When the spacing reduces to 1 cm, the gaps all become blurry and the 9 squares are barely discernible. This two cases suggest that all three configurations have similar resolving abilities, which means increasing the element spacing does not affect the resolution too much. Moreover, reconstruction of both two target scenes suggests the compressive Luneburg lens imaging method is also able to break the resolution limit of traditional FT methods.

## 7.5 Summary

In this chapter, we present a beam steering imaging system with a Luneburg lens antenna where CS technique is adopted for image reconstruction. The response matrix of the imaging system is calculated using full-wave EM simulated data. A fully automated parameter sweep method using CST is also demonstrated with Matlab and VBA codes. The mechanic scanning scheme is validated using 900 samples at 10 GHz. Image reconstruction using CS techniques offers higher resolution than conventional methods. By reducing the element spacing and increasing the lens aperture, it is possible to use a feeding array for fast electronic beam steering which helps reduces the data acquisition time.

## References

[1] K. B. Cooper, R. J. Dengler, N. Llombart, T. Bryllert, G. Chattopadhyay, E. Schlecht, J. Gill, C. Lee, A. Skalare, I. Mehdi *et al.*, "Penetrating 3-d imaging at 4-and 25-m range using a submillimeter-wave radar," *IEEE Transactions on Microwave Theory and Techniques*, vol. 56, no. 12, pp. 2771–2778, 2008.

[2] K. Cooper, R. Dengler, G. Chattopadhyay, E. Schlecht, J. Gill, A. Skalare, I. Mehdi, and P. Siegel, "A high-resolution imaging radar at 580 ghz," *IEEE Microwave and wireless components letters*, vol. 18, no. 1, pp. 64–66, 2008.

[3] K. B. Cooper, R. J. Dengler, N. Llombart, B. Thomas, G. Chattopadhyay, and P. H. Siegel, "Thz imaging radar for standoff personnel screening," *IEEE Transactions on Terahertz Science and Technology*, vol. 1, no. 1, pp. 169–182, 2011.

[4] J. Ala-Laurinaho, J. Aurinsalo, A. Karttunen, M. Kaunisto, A. Lamminen, J. Nurmiharju, A. V. Räisänen, J. Säily, and P. Wainio, "2-d beam-steerable integrated lens antenna system for 5g *e*-band access and backhaul," *IEEE Transactions on Microwave Theory and Techniques*, vol. 64, no. 7, pp. 2244–2255, 2016.

[5] J. Grzyb, K. Statnikov, N. Sarmah, B. Heinemann, and U. R. Pfeiffer, "A 210-270 ghz circularly polarized fmcw radar with a single-lens-coupled sige hbt chip," *IEEE Transactions on Terahertz Science and Technology*, vol. 6, no. 6, pp. 771–783, 2016.

[6] A. Artemenko, A. Mozharovskiy, A. Maltsev, R. Maslennikov, A. Sevastyanov, and V. Ssorin, "Experimental characterization of e-band two-dimensional electronically beam-steerable integrated lens antennas," *IEEE Antennas and Wireless Propagation Letters*, vol. 12, pp. 1188–1191, 2013.

[7] G. Bekefi and G. Farnell, "A homogeneous dielectric sphere as a microwave lens," *Canadian Journal of Physics*, vol. 34, no. 8, pp. 790–803, 1956.

[8] R. Ilinsky, "Gradient-index meniscus lens free of spherical aberration," *Journal of Optics A: Pure and Applied Optics*, vol. 2, no. 5, p. 449, 2000.

[9] B. Fuchs, L. Le Coq, O. Lafond, S. Rondineau, and M. Himdi, "Design optimization of multishell luneburg lenses," *IEEE Transactions on Antennas and Propagation*, vol. 55, no. 2, pp. 283–289, 2007.

[10] R. K. Luneburg, *Mathematical theory of optics.* Providence, Rhode Island, USA: Brown University, 1944.

[11] D. Donoho, "Compressed sensing," *IEEE Transactions on Information Theory*, vol. 52, no. 4, pp. 1289–1306, April 2006.

[12] C. Mateo-Segura, A. Dyke, H. Dyke, S. Haq, and Y. Hao, "Flat luneburg lens via transformation optics for directive antenna applications," *IEEE Transactions on Antennas and Propagation*, vol. 62, no. 4, pp. 1945–1953, April 2014.

[13] E. Buckley, "Stepped-index luneburg lenses," *Electron. Design*, vol. 8, pp. 86–89, 1960.

[14] R. Sauleau and B. Barès, "A complete procedure for the design and optimization of arbitrarily shaped integrated lens antennas," *IEEE Transactions on Antennas and Propagation*, vol. 54, no. 4, pp. 1122–1133, 2006.

[15] J. B. Pendry, D. Schurig, and D. R. Smith, "Controlling electromagnetic fields," *Science*, vol. 312, no. 5781, pp. 1780–1782, 2006.

[16] H. F. Ma and T. J. Cui, "Three-dimensional broadband and broad-angle transformation-optics lens," *Nature communications*, vol. 1, p. 124, 2010.

[17] A. Demetriadou and Y. Hao, "Slim luneburg lens for antenna applications," *Opt. Express*, vol. 19, no. 21, pp. 19 925–19 934, Oct 2011.

[18] R. Yang, W. Tang, and Y. Hao, "A broadband zone plate lens from transformation optics," *Opt. Express*, vol. 19, no. 13, pp. 12 348–12 355, Jun 2011.

[19] R. K. Amineh, J. McCombe, and N. K. Nikolova, "Microwave holographic imaging using the antenna phaseless radiation pattern," *IEEE Antennas and Wireless Propagation Letters*, vol. 11, pp. 1529–1532, 2012.

[20] S. S. Chen, D. L. Donoho, and M. A. Saunders, "Atomic decomposition by basis pursuit," *SIAM review*, vol. 43, no. 1, pp. 129–159, 2001.

[21] M. V. Afonso, J. M. Bioucas-Dias, and M. A. Figueiredo, "Fast image recovery using variable splitting and constrained optimization," *IEEE Transactions on*

*Image Processing*, vol. 19, no. 9, pp. 2345–2356, 2010.

# Chapter 8

# Conclusions and Future Work

## 8.1 Summary

In this thesis, we mainly investigated the CS implementation to array based imaging systems. The research work can be divided into four major parts as follows.

Two distinct CS approaches were first studied for the 2-D short-range switched array MMW imaging. Both numerical and experimental data are used for the comparative study. With highly under-sampled data, both CS approaches still outperform the conventional FT method in many scenarios. When compared with each other, the D-CS approach that directly utilizes the classic CS formulation demonstrates better imaging performance than the FT-CS approach that relies on conventional FT method. More specifically, when sufficient samples and moderate SNR are satisfied, the D-CS approach can achieve higher resolution with a sparser array. This big advantage helps to reduce the number of minimum required elements of a traditional imaging array.

Without considering the high computational complexity, the D-CS approach is then applied to the phased array imaging system. A 3-D forward imaging model is derived and verified with numerical results. The proposed method is able to provide high resolution

reconstruction with under-sampled data in both frequency and angular domains. This work is further extended for near-field applications by integrating a near-field focusing technique into the CS framework. A new point scanning method has also been provided for better coverage. When compared with its far-field counterpart, the near-field method shows better robustness against noise and interfering targets from the background.

The D-CS approach is finally applied to the MIMO array configuration. The CS forward imaging model is derived and tested with a cross-shaped MIMO array. A comparative study on the performance of D-CS methods with aforementioned three array configurations is carried out with numerical simulations. All three methods have the same level of resolution due to the same effective aperture size. The MIMO array is able to achieve comparable performance as the switched array with far fewer antenna elements. While all three array configurations are capable of imaging with sub-Nyquist element spacing, the phased array is more sensitive to this element spacing factor. This can be explained by fact that too few elements will fail the beamforming process. As for the robustness against noise, the phased array outperforms the other two arrays. Finally, the computational complexity of the three methods is analyzed. The MIMO array has approximately doubled time in computing the response matrix than the switched array due to the separate Tx/Rx pairs. The phased array, on the other hand, cost too much time here due to the beamforming process.

As an alternative to the expensive phased array imaging, a novel low-cost beam-steering imaging system using Luneburg lens is presented as the last part of the thesis. The proposed system consists of a flat Luneburg lens fed by an antenna array. By exciting the feeding elements at different locations, the lens forms directive beams to scan the region of interest. CS techniques are adopted in the image reconstruction and thus enables high resolution images and also under-sampling during data acquisition. Mechanically scanned data using full-wave simulated radiation patterns are first used to verify the idea of Luneburg lens imaging. Considering that the actual feeding area might be relatively small to fit in a normally spaced array, we tested the sub-Nyquist element

spacing which turns out to be an effective way to alleviate the limited space issue.

## 8.2 Key Contributions

The key contributions presented in the four major parts are listed as follows:

1. *Compressive switched array imaging.* The performance of the FT-CS and D-CS methods are studied in detail in terms of element spacing, resolution, computational complexity, robustness to noise and under-sampling rate. Both qualitative and quantitative results are used in the comparative study. The superior resolving power of the D-CS method makes it desirable for high resolution imaging applications. More importantly, element spacing can be slightly larger than the Nyquist criterion required, which means high resolution imaging can be achieved with fewer antenna elements than conventional methods.

2. *Compressive phased array imaging.* A general imaging forward model is derived for array based imaging systems by taking into consideration the antenna factors. This model can be easily applied to other array configurations with slight modifications. Based on this forward model, a 3-D compressive imaging method based on conventional phased array configuration is proposed. As mutual coherence is related to the CS reconstruction performance, coherence analysis of different sensing configurations is also provided as a guidance for system design for better imaging performance. Considering some imaging applications like personnel surveillance imaging are usually in the short range, a near-field focusing technique is integrated into the CS framework for the purpose of near-field imaging.

3. *Comparative study of compressive sensing methods in different array configurations.* Compressive MIMO array imaging is first derived in this chapter. A comparative study on the performance of CS methods with the three array configurations is then presented. Resolution, effects of element spacing, robustness against noise,

and computational complexity are discussed with several numerical examples.

4. *Compressive Luneburg lens imaging.* This chapter demonstrates a novel low-cost beam-steering imaging system using a flat Luneburg lens. CS technique is integrated into the imaging reconstruction algorithm. To calculate the system response matrix, a radiation pattern based approach using full-wave EM solver is presented. A fully automated simulation method for the generation of radiation patterns is provided with Matlab and VBA codes.

## 8.3 Future work

Based on the present results, further work can be carried out in the following areas:

- According to our results in Chapter 4, the FT-CS method is very sensitive to the regularization parameter when compared to the D-CS method. It should be carefully calibrated with respect to different under-sampling pattern and different targets. This essential calibration process has greatly limited the application of the FT-CS method as the target scene is usually unknown in practice. An adaptive scheme that can adaptively change the regularization parameter in reconstruction according to the target scene is desperately needed for the D-CS method.

- As mentioned previously, the sparsity basis for the complex-valued data in MMW array imaging is more complicated than the real-valued case. Different from terahertz imaging and SAR imaging, the phase information of the acquired data in our case can be seen as between random and smooth varying. It is possible that these differences are caused by the target-to-antenna distance. An optimal sparsity constraint for such case would be of great interest.

- Chapter 6 provides an alternative way of data acquisition by focusing the array beams at different spots with various depths. Simulation results prove the effectiveness of this method and provide a new insight into phased array pattern control for

imaging applications. For one particular application, there exist numerous pattern combinations that can successfully give a reconstruction. From the perspective of CS theory, the series of patterns have to be relatively independent so that the corresponding system response matrix has low mutual coherence. However, this might lead to a series of random low-gain patterns, which are not preferred for noisy environment as they have lower SNR compared to conventional high gain pencil beam patterns. It is of great importance if we can find a way to design optimized pattern combinations according to the imaging applications. This is an interesting optimization problem and could be a new hot topic for not only the phased array imaging system, but also other reconfigurable antenna imaging systems like meta-surface antenna and reflect-array antenna.

- CS imaging methods not only offers much better reconstruction results than conventional Fourier methods but also greatly reduce the data acquisition time. Nevertheless, CS methods suffer from high computational complexity in reconstruction and data storage. This could limit their applications to imaging systems that have low or limited computing power. This issue becomes extremely serious when it comes to 3-D imaging and real-time imaging. New recovery algorithms should be developed such that both the ability to reduce data acquisition time and fast image reconstruction can be achieved.

- Traditional MIMO array design focuses on the position arrangement of the transmit and receive elements. The goal is to achieve sharp beam with low side lobes, which is usually verified by showing the PSF or the reconstruction of a point-like target. In compressive MIMO array imaging, the imaging performance is related to the probability of successful CS reconstruction, which is determined by the well-condition of the system response matrix. Therefore, for optimized performance in compressive MIMO array imaging, the goal of array design becomes to arrange the geometry of the transmit and receive arrays such that the response matrix is well-conditioned for CS reconstructions. The evaluation metric of how the response

matrix is well-conditioned can be the well-known RIP, mutual coherence or any other potential methods. This well-condition evaluation process can be surely integrated into an optimization problem and the array design problem can then be solved by a lot of optimization techniques. Although the compressive MIMO array design is completely different from the traditional MIMO array design, we believe there must be some connections between them and further research should be done.

- Chapter 7 has demonstrated a Luneburgn lens imaging system using a mechanically scanned horn fed. As a continuation of this work, one would like to design an array to feed the Luneburg lens for electronic beam steering. For optimal imaging performance, the array should maintain high gain, low mutual coupling, good matching with the lens, and should also be compact in size. Considering the complexity in calibrating the imaging system, it is desirable to design the feeding array and the lens as a whole system like an Integrated Lens Antenna (ILA). The main drawback of the compressive Luneburg lens imaging is the time-consuming calculation of the response matrix. Moreover, full-wave EM solvers and real experiments sometimes are not available for the generation of the radiation patterns. Therefore, approximated methods like PO and GO techniques that give fast calculation should be an object or further research.

# Appendix A

# Author's publications

### Journal papers

1. **Q. Cheng**, A. Alomainy, and Y. Hao, "Near-Field Millimeter-Wave Phased Array Imaging with Compressive Sensing," *IEEE Access*, vol. 5, pp. 18975-18986, 2017.

2. **Q. Cheng**, A. Alomainy, and Y. Hao, "Compressive Millimeter-Wave Phased Array Imaging," *IEEE Access*, vol. 4, no. , pp. 9580-9588, 2016.

3. La Spada, L., T. M. McManus, A. Dyke, S. Haq, L. Zhang, **Q. Cheng**, and Y. Hao, "Surface Wave Cloak from Graded Refractive Index Nanocomposites," *Scientific Reports* 6 (2016).

4. **Q. Cheng**, A. Alomainy, and Y. Hao, "On the Performance of Compressed Sensing-based Methods for Millimeter-wave Holographic Imaging," *Applied Optics*, 2016 Feb 1; 55(4):728-38.

## Conference papers

1. **Q. Cheng**, A. Alomainy, and Y. Hao, "Comparative Study of Compressive Sensing Imaging in Different Array Configurations", 2018 Twelfth European Conference on Antennas and Propagation, London, UK. (Accepted)

2. **Q. Cheng**, A. Alomainy, and Y. Hao, "Luneburg Lens Imaging with Compressive Sensing", 2017 Sixth Asia-Pacific Conference on Antennas and Propagation, 2017, Xi'an, China.

3. **Q. Cheng**, A. Alomainy, and Y. Hao, "Resolution Analysis of Compressed Sensing Based Methods for Single Frequency Radar Imaging", 2016 IEEE International Symposium on Antennas and Propagation/USNC-URSI National Radio Science, 2016, Fajardo, Puerto Rico.

4. **Q. Cheng**, A. Alomainy, and Y. Hao, "Effect of Antenna Directivity on the Accuracy of Fingerprint-based Localisation," 5th EAI International Conference on Wireless Mobile Communication and Healthcare, 14-16 October 2015, London, UK.

5. **Q. Cheng**, M. Munoz, A. Alomainy, and Y. Hao, "Compressive sensing applied to fingerprint-based localisation," in RF and Wireless Technologies for Biomedical and Healthcare Applications (IMWS-Bio), 2014 IEEE MTT-S International Microwave Workshop Series on , vol., no., pp.1-3, 8-10 Dec. 2014

# Appendix B

# Code for Antenna Radiation Pattern Generation in CST

## B.1 Matlab Code to Control CST

Listing B.1: Some class definition

```
clear;clc;
newdir='C:\CST\datasave\';
cst_prj_name = 'C:\CST\Luneburg Lens Imaging.cst';
patternfile='C:\CST\Luneburg Lens Imaging\Export\Farfield\
   farfield (f=10) [2].txt';
N_x=30;N_y=30;
N=N_x*N_y; % Number of sampling points
xmax=30;ymax=30;
x=linspace(-xmax,xmax,N_x);
y=linspace(-ymax,ymax,N_y);
temp=repmat(x,N_y,1);
xy(:,1)=temp(:);
```

```
temp=repmat(y',N_x,1);
xy(:,2)=temp; % Coordinates matrix

for i=1:N
    tic
    %% CST start
    cst = actxserver('CSTStudio.application');

    %% Open the project file and update parameters
    mws=invoke(cst, 'OpenFile', cst_prj_name);
    invoke(mws,'StoreParameter','G_fx',xy(i,1));
    invoke(mws,'StoreParameter','G_fy',xy(i,2));
    invoke(mws,'Rebuild');
    invoke(mws,'Save');

    %% Finish CST session
    invoke(mws, 'Quit');
    release(mws);
    invoke(cst, 'Quit');
    release(cst);

    %% Call VBA code to run CST solver
    ! "C:\Program Files (x86)\CST STUDIO SUITE 2016\CST
       DESIGN ENVIRONMENT.exe" -m C:\CST\runsolver.bas

    %% Move radiation pattern file to new folder and rename
    movefile(patternfile,char(strcat(newdir,num2str(i,'%04d'
       ),'.txt')));

```

```
    %% Time estimation
    time=toc;
    disp(['############  Loop ',num2str(i), ' of ',num2str(N
       ),'...']);
    disp(['Remaing time = ',num2str((N-i)*time/60), '
       minutes / ',num2str((N-i)*time/60/60),' hours']);
    datestr(now)
    fprintf('\n\n')

end
```

## B.2 VBA Code to Configure CST

Listing B.2: Some class definition

```
Option Explicit

Sub Main
  OpenFile("C:\CST\Luneburg Lens Imaging.cst")
  Solver.Start
  Save
End Sub
```

## B.3 Matlab Code to Extract Data

Listing B.3: Some class definition

```
clear;clc;
cd 'C:\CST\datasave\' % Change Matlab working folders
```

```
newdir='C:\CST\datasave\';
newdir2='C:\MATLAB\Luneburg\';

%% Calculate the total number of txt files
txtname=dir('*.txt');
N=length(txtname);

%% Read radiation pattern data and save to one single file
pattern_matrix=single(zeros(65160,N));   % single precision
angle_matrix=zeros(65160,2);
for i= 1:N
  filename=char(strcat(newdir,num2str(i,'%04d'),'.txt'));
  [theta, Phi, Efield]=textread(filename,' %f %f %f %*s %*s
     %*s %*s %*s','headerlines',2);
  angle_matrix(:,1)=theta;
  angle_matrix(:,2)=Phi;
  pattern_matrix(:,i)=Efield;
end
save(char(strcat(newdir2,'CST_VBA_Radiation_Pattern_10G_',
   num2str(N,'%04d'),'.mat')),'angle_matrix','pattern_matrix
   ');
```